

Aus dem
Institut für Neuropathologie
Ludwig-Maximilians-Universität München



**Astrocytic Diazepam Binding Inhibitor Instructs Microglial
Synaptic Engulfment in Lewy Body Dementia**

Dissertation
zum Erwerb des Doctor of Philosophy (Ph.D.)
an der Medizinischen Fakultät der
Ludwig-Maximilians-Universität München

vorgelegt von
Mochen Cui

aus
Ürümqi, China

Jahr
2023

Mit Genehmigung der Medizinischen Fakultät der
Ludwig-Maximilians-Universität München

Erstes Gutachten: Prof. Dr. Jochen Herms

Zweites Gutachten: Prof. Dr. Johannes Levin

Drittes Gutachten: Prof. Dr. Dieter Edbauer

Viertes Gutachten: Prof. Dr. Lars Kellert

Dekan: Prof. Dr. med. Thomas Gudermann

Tag der mündlichen Prüfung: 21.11.2023

Veritas tantum conservetur.

Table of Contents

Summary	IX
1. Introduction.....	1
1.1 Lewy body dementia (LBD)	1
1.1.1 <i>The discovery and conceptualization of Lewy body dementia</i>	1
1.1.2 <i>Epidemiology of LBD</i>	3
1.1.3 <i>Symptoms and diagnosis of LBD</i>	3
1.1.4 <i>Pathogenesis and pathological process of LBD</i>	4
1.2 Dendritic spines	6
1.2.1 <i>Structure of dendritic spines</i>	7
1.2.2 <i>Dendritic spine morphology and its functional significance</i>	8
1.2.3 <i>TSPO and glial activation</i>	10
1.2.4 <i>Dendritic spine alterations in LBD</i>	11
1.3 Microglia and 18 kDa translocator protein (TSPO).....	11
1.3.1 <i>Physiology of microglia</i>	12
1.3.2 <i>Microglia-dendritic spine interaction</i>	12
1.3.3 <i>Altered microglia-dendritic spine interaction in CNS disorders</i>	14
1.3.4 <i>TSPO is a biomarker for microglial activity</i>	16
1.3.5 <i>Regulation of microglial states via TSPO</i>	17
1.3.6 <i>Endogenous ligands of TSPO</i>	19
1.4 Astrocytes and diazepam binding inhibitor (DBI)	20
1.4.1 <i>Physiology of astrocytes</i>	21
1.4.2 <i>Astrocytes regulate synapses via secretory pathways</i>	22

1.4.3 Astrocytes-microglia interaction in health and diseases.....	23
1.4.4 Astrocytes are the primary DBI source in the CNS	24
1.4.5 DBI is an ancestral protein with diverse and emerging functions.....	25
1.4.6 Alterations of DBI in CNS disorders.....	26
1.5 In vivo two-photon imaging.....	27
2. Methods	31
2.1 Animals	31
2.2 Genotyping.....	32
2.3 Drug administration.....	33
2.4 Postmortem human brain tissue	33
2.5 Perfusion	34
2.6 Immunostaining	35
2.7 Proximity ligation assay (PLA)	38
2.8 Brain extracellular fluid (ECF) collection.....	40
2.9 Immunodepletion.....	40
2.10 Primary astrocytes and microglia isolation.....	41
2.11 Primary microglia culture	41
2.12 pHrodo-conjugated synaptosome preparation	42
2.13 Microglia phagocytosis assay	43
2.14 Confocal imaging	44
2.15 Super-resolution confocal imaging.....	44
2.16 Cerebral protein extraction	45
2.17 Co-immunoprecipitation	45
2.18 Immunoblotting.....	46

2.19 Enzyme-linked immunosorbent assay (ELISA).....	47
2.20 Stereotactic injection	47
2.21 Cranial window implantation	48
2.22 <i>In vivo</i> imaging of dendritic spines	49
2.23 Image analysis for astrocytes and microglia.....	50
2.24 Image analysis for dendritic spines.....	52
2.25 Image analysis for neurons and blood vessels	54
2.26 Key resources.....	54
2.27 Key software tools.....	56
2.28 Statistics	56
3. Results	58
3.1 Elevated astrocytic DBI and microglial TSPO in LBD	58
3.1.1 <i>Astrocytic DBI expression and release increase in LBD</i>	58
3.1.2 <i>Microglial TSPO enhances in LBD</i>	60
3.1.3 <i>DBI-TSPO bindings elevate in LBD</i>	62
3.2 Enhanced microglial synaptic engulfment via DBI-TSPO signaling.....	64
3.2.1 <i>Morphological alterations of microglia in LBD</i>	64
3.2.2 <i>Elevated TSPO-dependent microglial synaptic engulfment</i>	66
3.2.3 <i>Elevated microglial synaptic engulfment via DBI-TSPO signaling</i>	68
3.2.4 <i>DBI-induced alteration of TSPO-mediated phagocytosis of primary microglia</i>	69
3.3 DBI-TSPO suppression alleviates dendritic spine pathology in LBD.....	74
3.3.1 <i>Dendritic spine impairment in LBD</i>	74
3.3.2 <i>TSPO deficiency alleviates dendritic spine impairment in LBD</i>	75

3.3.3 <i>Microglia depletion attenuates dendritic spine impairment in LBD</i>	77
3.3.4 <i>DBI knockdown mitigates dendritic spine impairment in LBD</i>	79
3.4 Altered DBI-TSPO signalling in the brains of patients with LBD.....	85
3.4.1 <i>Astrocytic DBI elevates in human LBD patients</i>	85
3.4.2 <i>Microglial TSPO enhances in human LBD patients</i>	86
4. Discussion	88
4.1 DBI exerts regulatory functions beyond TSPO.....	88
4.2 Non-microglial TSPO alters in CNS disorders.....	89
4.3 DBI-TSPO signaling as a general pathway for synaptic regulation.....	91
4.4 The penta-partite synapse is an integral unit for synaptic studies.....	93
5. Conclusion.....	97
List of Figures and Tables	99
Bibliography	102
Abbreviations.....	125
Acknowledgments.....	130
List of Publications.....	132
Eidesstattliche Versicherung/Affidavit	135
Confirmation of Congruency	136

Summary

In Lewy body dementia (LBD), loss of synapses is associated with reactive astrocytes and activated microglia. However, the interaction between these two major glial cell types and the subsequent implications on synaptic removal remain unclear. This study demonstrates that anomalous secretion of astrocyte-derived diazepam binding inhibitor (DBI), an endogenous ligand of the 18 kDa translocator protein (TSPO), facilitates excessive microglial phagocytosis of synaptic materials in a mouse model of LBD and in postmortem brains of patients with LBD-associated dementia. Additionally, evidence is presented suggesting that the decline of synaptic plasticity in LBD-associated dementia is dependent on the astrocytic DBI-microglial TSPO signaling pathway, as it can be mitigated by DBI knock-down or TSPO knock-out. These findings emphasize the significance of astrocyte-microglia interaction in regulating synaptic plasticity and propose the non-neuronal DBI-TSPO signaling pathway between these glial cells as potential therapeutic targets to improve synaptic pathology in LBD-associated dementia.

1. Introduction

1.1 Lewy body dementia (LBD)

Lewy body dementia is an umbrella term that includes two diseases: Parkinson's disease dementia (PDD) and dementia with Lewy bodies (DLB). Both of them are characterized by prominent syndromes of dementia and parkinsonism¹. Collectively, PDD and DLB represent the second most prevalent form of degenerative dementia².

1.1.1 *The discovery and conceptualization of Lewy body dementia*

In 1817, the English surgeon James Parkinson published a seminal dissertation titled "An Essay on the Shaking Palsy"³, wherein he detailed six cases and provided a comprehensive portrayal of their symptoms, such as "involuntary tremulous motion" and "inclination to bend the trunk forwards." The disease he identified in his dissertation as "shaking palsy" (*paralysis agitans*) has since been acknowledged as Parkinson's disease (PD)^{4,5}. Although there are earlier yet brief descriptions of similar conditions, such as "running involuntarily" and "being incapable of maintaining directions so as to circumvent impediments" observed in older adults^{6,7}, Parkinson was distinguished by his ability to discern the shaking palsy from other conventional cases of palsy and classify it as a separate disease.

Despite the widespread use of the term "Parkinson's disease", the neuropathology of the disease remained largely enigmatic until the early 20th century. In 1912, the German neurologist Fritz Heinrich Lewy discovered eosinophilic intracytoplasmic inclusions in the posterior nucleus of the vagus nerve, Meynert's nucleus, and the thalamic paraventricular nucleus in the cerebral specimens of PD patients^{8,9}. Following this discovery, the Russian neuropathologist Konstantin Nikolaevitch Tretiakoff coined the term "Lewy bodies (corps de Lewy)" in his dissertation to delineate these inclusions^{10,11}. In addition to assigning a name to the pathological entities, Tretiakoff

was one of the pioneers who identified and documented the significant degenerative processes occurring in the substantia nigra of patients with PD¹⁰, shedding light on the intricate pathophysiology of the disease.

Since then, the presence of Lewy bodies in the brains of PD patients has been increasingly supported by evidence. In the 1950s and 1960s, Greenfield and Bosanquet¹², followed by Bethlem and Den Hartog Jager¹³, published successive reports that provided comprehensive insights into the distribution patterns of Lewy bodies throughout the brains of PD-afflicted patients, predominantly within subcortical regions such as locus coeruleus and substantia nigra. These studies contributed significantly to establishing the contemporary understanding of the neuropathological basis of PD. However, at that time, the presence of Lewy bodies within the cerebral cortex of PD-affected brains was not widely acknowledged or accepted¹⁴.

It was not until 1976 that the Japanese psychiatrist Kenji Kosaka and colleagues documented a series of cases involving parkinsonism concomitant with progressive dementia¹⁵. Following postmortem analyses, numerous Lewy bodies were discerned within the neurons situated in deeper cortical layers in addition to the subcortical regions. As an increasing number of similar cases emerged, the nomenclature "Lewy body disease" was established¹⁶. During later years, this disorder was characterized more meticulously by the accumulation of α -synuclein aggregates into Lewy bodies and Lewy neurites present in neurons and neuronal processes, collectively known as Lewy-related pathology¹⁷.

According to the current agreement, the spectrum of Lewy body diseases encompasses PD, Parkinson's disease dementia (PDD), and dementia with Lewy bodies (DLB)¹⁸. Given the primary manifestation of dementia in both PDD and DLB, they are frequently referred to collectively as Lewy body dementia (LBD)².

1.1.2 Epidemiology of LBD

LBD predominantly affects elderly individuals, although infrequent instances have been documented prior to the age of 65^{2,19}. Converging evidence from clinical examinations and postmortem investigations substantiates that, among individuals aged 65 years and beyond, LBD constitutes the second most prevalent form of degenerative dementia².

Recent evaluations have revealed that nearly a quarter of patients diagnosed with PD concurrently grapples with dementia¹⁹. Moreover, the probability of dementia emergence escalates to 50% within 10 years following the initial PD diagnosis²⁰. In the long run, dementia ultimately develops in a staggering 80% of the entire PD patient population²¹.

The approximated prevalence of LBD within the general population aged 65 and over differs depending on distinct methodologies, encompassing clinic-based or community-based approaches, as well as diverse populations, collected relying on medical records or diagnostic evaluations. Broadly speaking, the estimated prevalence of LBD in the general population fluctuates between 0.2% and 0.5%^{19,22}.

1.1.3 Symptoms and diagnosis of LBD

Over the past few decades, the study of LBD has undergone a gradual refinement process, which has led to an improved understanding of the symptoms and diagnostic criteria of these diseases.

In 1996, a milestone was reached with the establishment of the first International Consensus Criteria (ICC) for the diagnosis of DLB. The initial version of the ICC prioritized the central feature of cognitive decline, which impedes an individual's social and occupational abilities. The central feature was accompanied by additional core features such as cognitive fluctuation, visual hallucinations, and parkinsonism²³. It is noteworthy that the initial version of the ICC primarily relied on clinical features

acquired through anamnesis and neurological assessments and did not offer guidance on differentiating between DLB and PDD²³.

The landscape of diagnosing DLB and PDD was transformed in 2005 with the promulgation of the updated ICC. This augmented edition drew upon a plethora of clinical and foundational research, and integrated multiple biomarkers as indicative features of DLB¹⁸. These biomarkers included rapid eye movement (REM) sleep behavior disorder, pronounced neuroleptic sensitivity, and reduction of dopamine transporter uptake in the basal ganglia, detected by single-photon emission computed tomography or positron emission tomography (PET) imaging¹⁸.

By assimilating these biomarkers into the diagnostic schema, the precision of DLB/PDD identification was improved, and the possibility of early diagnosis, even preceding clinical manifestations, was proposed. Furthermore, the 2005 ICC emphasized the chronological progression of LBD symptoms and instituted the "one-year rule," which clearly demarcated DLB from PDD¹⁸. According to this guideline, the onset of dementia within one year after the initiation of movement disorders is categorized as DLB, while its emergence following this interval is designated as PDD¹⁸. Since this distinction is based solely on clinical observations, it is more appropriate to consider the two primary LBD syndromes – dementia and parkinsonism – as a continuum sharing a similar pathological underpinning rather than as distinct entities¹. In summary, these advancements constituted a significant enhancement over the 1996 ICC and represented a crucial stride forward in the diagnosis and comprehension of LBD.

1.1.4 Pathogenesis and pathological process of LBD

The primary pathological hallmark of LBD is the manifestation of α -synuclein neuronal inclusions, which subsequently leads to neuronal loss¹⁷. These inclusions typically materialize as Lewy bodies and Lewy neurites, jointly denoted as Lewy-related

pathology¹⁷. In a healthy human brain, α -synuclein is abundantly expressed throughout the neocortex, midbrain, and cerebellum, constituting approximately 1% of the total cytosolic proteins²⁴. Within these regions, α -synuclein primarily resides in neurons, specifically in presynaptic terminals²⁵. By establishing a close association with synaptic vesicles in the reserve pool^{26,27}, α -synuclein plays an essential role in modulating neurotransmitter release, synaptic operations, and synaptic structural plasticity^{28,29}.

Under physiological conditions, α -synuclein appears as an intrinsically disordered protein, either as a monomeric entity or as a multimeric α -helical assembly³⁰. However, during the onset of LBD, α -synuclein undergoes a conformational alteration, transitioning from the monomeric state to β -sheet structures, resulting in the formation of protofilaments and amyloid fibrils³¹. These fibrillary aggregates are the primary components of Lewy bodies and Lewy neurites³². Although the causal factors instigating the aggregation of α -synuclein remain unclear, a substantial body of evidence strongly indicates a multifaceted etiology underlying this process.

The complex etiology is postulated to encompass a diverse array of risk factors, including genetic alterations such as missense point mutations, like the Contursi kindred A53T mutation³³, the German A30P mutation³⁴, and the Spanish E46K mutation³⁵. Additionally, an assortment of environmental factors has been identified as potential contributors to α -synuclein aggregation, comprising exposure to neurotoxic agents such as metals³⁶, carbon monoxide³⁷, specific solvents³⁸, and a range of pesticides and herbicides³⁹.

Although the etiology of LBD continues to be enigmatic, the advancement of Lewy-related pathology has become increasingly discernible. As the pathology progresses, the lesions of Lewy-related pathology exhibit a more pervasive distribution throughout the brain⁴⁰. In 2003, Braak and colleagues proposed a staging method for PD based on the histopathological examination of Lewy-related pathology, regardless of cognitive decline status⁴⁰. According to the examination results, the pathological

development begins in the dorsal motor nucleus or the proximate intermediate reticular zone, subsequently disseminating to the substantia nigra and basal ganglia. Thereafter, it permeates the limbic system and ultimately extends to the neocortex⁴⁰. The exact process through which Lewy-related pathology propagates remains elusive. Nevertheless, a plethora of investigations conducted over the previous decades has corroborated the transmissible nature of misfolded α -synuclein between cells, both *in vitro* and *in vivo*⁴¹⁻⁴³.

In accordance with the propagation of Lewy-related pathology⁴⁰ and the emergence of dementia¹⁸, a significant reduction in dendritic spines has been observed in LBD patients⁴⁴. Dendritic spines are the structural correlates of cognitive function^{45,46}. Nonetheless, the precise mechanisms underlying their decline in LBD pathology remain incompletely understood. In this study, I focus on unveiling the crucial mechanism that expedites the aberrant loss of dendritic spines in both the mouse model and human subjects affected by LBD.

1.2 Dendritic spines

Dendritic spines, initially delineated by the Spanish neuroscientist Santiago Ramón y Cajal in the late 19th century⁴⁷, constitute minuscule protrusions⁴⁸ that emerge from the intricate and ramified neuronal dendrites⁴⁹. In the central nervous system (CNS), dendritic spines serve as the postsynaptic components (Fig. 1), facilitating the majority of excitatory connections by receipting and transmitting the signaling inputs from presynaptic terminals⁵⁰.

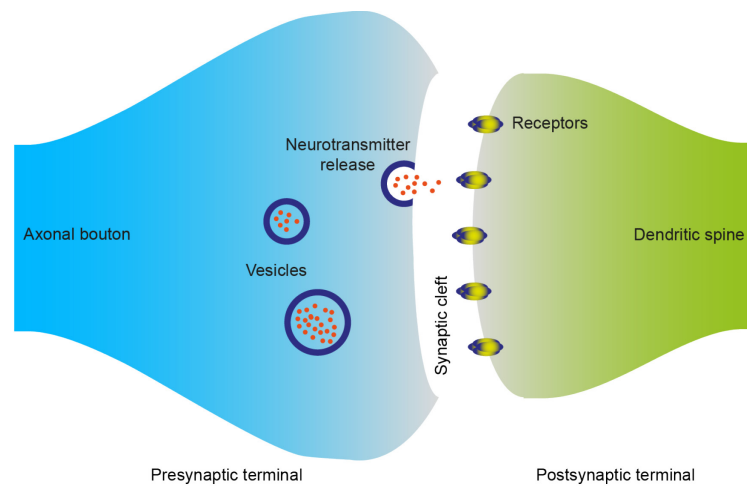


Figure 1 Scheme of an asymmetric synapse.

The axonal bouton serves as the presynaptic terminal, encompassing synaptic vesicles replete with neurotransmitters. Upon synaptic activation, the neurotransmitters are exocytosed into the synaptic cleft, followed by their binding to receptors on the postsynaptic terminal, typically the dendritic spine. This interaction facilitates the transmission of informational input to the targeted neurons.

1.2.1 Structure of dendritic spines

Dendritic spines typically range in length from 0.1 to 2 μm depending on the species and the corresponding brain region⁵¹. A mature dendritic spine usually consists of a globoid head and a narrow neck that connects it to the dendrite.

The spine head is separated from the presynaptic terminal by the synaptic cleft. Most spine heads contain a postsynaptic density (PSD), an intricate architecture consisting of an array of neurotransmitter receptors, ion channels, scaffolding proteins, and signaling complexes⁵². This intricate architecture functions as an organized and integral framework to facilitate signal transduction within the postsynaptic domain⁵³. Apart from the PSD, larger spine heads usually contain the smooth endoplasmic reticulum (SER), a well-established Ca^{2+} reservoir that can be evoked by local receptors such as the ryanodine and inositol (1,4,5)-trisphosphate [Ins(1,4,5)P₃] receptors⁵⁴. The ensuing Ca^{2+} release, known as Ca^{2+} -induced Ca^{2+} release (CICR), plays a crucial role in sustaining synaptic plasticity⁵⁴. Additionally, polyribosomes and mitochondria are frequently found within the spine heads, particularly in those

exhibiting larger dimensions, indicating active local protein synthesis and energy consumption^{55,56}.

The slender spine neck serves not only as a mechanical connection between the head and the dendrite but also as a regulator of the compartmentalization of Ca^{2+} in the spine head. Upon synaptic activation, spine necks with narrower diameters increase the retention of Ca^{2+} in the head region, thereby modulating local signaling cascades that can either enhance or weaken synapses⁵⁷. Additionally, the spine neck mediates the bidirectional protein diffusion, which is activity- and geometry-dependent⁵⁸. Longer and thinner spine necks can temporarily accommodate more molecules, including 1,4,5-triphosphate and the postsynaptic density protein 95 (PSD 95), which subsequently modulate Ca^{2+} or synaptic efficacy, respectively⁵⁹.

1.2.2 Dendritic spine morphology and its functional significance

Dendritic spines are generally grouped into three primary categories based on their size and compartmental arrangement, namely mushroom spines, thin spines, and stubby spines (Fig. 2)⁶⁰. Mushroom spines are characterized by a sizable, round head and a thinner, elongated neck, whereas thin spines exhibit smaller heads and longer necks compared to mushroom spines. In contrast, stubby spines are minuscule protrusions on dendrites that lack distinct heads or necks.

Even after reaching maturity and attaining relative stability, the three types of dendritic spines exhibit common yet differentiated morphological adaptability^{61,62}. For instance, recent studies have demonstrated that thin spines have a briefer observable lifetime, typically appearing and disappearing within a few days, while mushroom spines tend to endure for months^{61,62}.

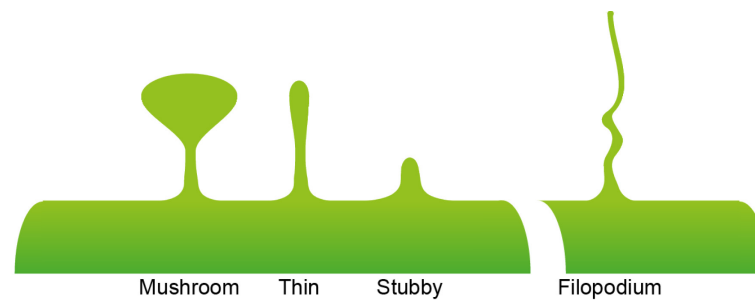


Figure 2 Scheme of dendritic spines of different morphology and filopodium.

The dendritic spines can be classified into three major types: mushroom, thin, and stubby. Filopodium is not considered a type of dendritic spine.

Besides varying observable lifetimes, dendritic spines of different morphologies possess distinct functionalities that contribute to cognitive performance. For example, mushroom spines contain large PSDs⁵² that house a significant number of α -amino-3-hydroxy-5-methyl-4-isoxazole propionic acid (AMPA) glutamate receptors, leading to potent synaptic functions^{63,64}. Additionally, the large head size of mushroom spines allows ample accommodation of SER⁶⁵ and polyribosomes⁵⁶, both of which are crucial for maintaining synaptic functionalities. Moreover, the large head of mushroom spines establishes connections with multiple perisynaptic astrocytic processes that provide supplementary synaptic stabilization and neurotransmitter regulation⁶⁶. These traits collectively indicate that mushroom spines are more stable and functionally closer to the concept of "memory"⁶⁷. In contrast, spines with smaller heads exhibit fewer PSDs and AMPA receptors, providing the potential for additional enhancement by increasing AMPA receptor numbers^{63,64}. Furthermore, such spines retain a higher degree of structural flexibility, enabling them to expand, stabilize, or retract in response to informational input. These qualities align these spines more closely with the concept of "learning"^{61,62,67}.

Apart from the morphological categories of dendritic spines mentioned above, there exist filopodia, which are dendritic protrusions that are not universally accepted as a type of dendritic spine⁶⁸. Filopodia are headless, elongated structures that extend from

the dendrite and can reach up to 10 μm in length⁶⁸. They typically form during the first postnatal week and are involved in the formation of nascent synapses, often resulting in shaft synapses or stubby spines⁶⁹. Filopodia can also be observed in the brains of older subjects. However, studies suggest that they are generally not associated with synapses⁶¹.

Therefore, in this dissertation, I focus on analyzing the three main types of dendritic spines, namely mushroom, thin, and stubby, both *in vivo* and *ex vivo*.

1.2.3 TSPO and glial activation

Despite their delineation over one hundred years ago, the morphological characteristics of dendritic spines have garnered substantial attention and comprehensive investigation only in recent times. This surge in interest can be predominantly attributed to breakthroughs in imaging techniques⁷⁰ and the discovery of fluorescent protein reporters⁷¹, which have implemented the visualization of dendritic spines and facilitated their subsequent studies, revealing that dendritic spines undergo a continuous turnover, demonstrating a degree of structural plasticity^{48,72}.

The structural plasticity of dendritic spines is influenced by various factors, encompassing neuronal activity⁷³, developmental factors⁷⁴, external stimuli (e.g., sensory experiences⁷⁵, environmental enrichment⁷⁶, and pharmacological interventions⁷⁷), and pathological conditions (e.g., neurodegenerative^{42,46,78,79} and psychiatric⁸⁰ disorders). Moreover, previous investigations have shown that the structural plasticity of dendritic spines impact synaptic strength⁸¹, subsequent memory consolidation⁸², and ultimately, cognitive performance⁵⁰. These findings suggest that dendritic spines represent the structural correlates of cognition, with their inherent plasticity underpinning cognitive shifts throughout healthy and pathological states^{45,46,83}.

1.2.4 Dendritic spine alterations in LBD

In accordance with the primary manifestation of cognitive deficits in LBD, persistent observations have unveiled substantial impairment of dendritic spines, which serve as the structural correlates of cognitive function, across diverse brain regions in both LBD-afflicted individuals and LBD animal models^{42,44,84-88}. Despite our limited comprehension of the specific factors that render dendritic spines susceptible to LBD, several theories have been proposed to elucidate potential mechanisms underlying this process.

Antecedent investigations delineating the neurotoxicity of α -synuclein aggregates⁸⁹ suggest that these aggregates may directly inflict harm upon dendritic spines and compromise their plasticity⁴². Contrarily, more recent discoveries indicate that dendritic spines sustain damage as a consequence of impaired neurotransmitter release subsequent to the accumulation of small α -synuclein aggregates in presynaptic terminals^{85,90}. Furthermore, glial cells, particularly microglia and astrocytes, have been shown to exhibit altered activities in LBD-affected brains^{91,92}. Given the pivotal role of microglia in dendritic spine elimination under both physiological and pathological circumstances⁹³, as well as the pronounced function of astrocytes in regulating synapses⁹⁴, it is reasonable to hypothesize that the alterations of these glial cells also exert a substantial influence on the alterations of dendritic spines in the context of LBD.

1.3 Microglia and 18 kDa translocator protein (TSPO)

Microglia are small and branched CNS glial cells first identified and described by Santiago Ramón y Cajal⁴⁷ and Pío Del Río-Hortega⁹⁵ in the early 20th century. Within the CNS, microglia serve as the primary immune cells⁹⁶ and play a crucial role in regulating dendritic spines across healthy and pathological states^{97,98}.

1.3.1 Physiology of microglia

Microglia, which comprise approximately 5-10% of the total CNS cellular population⁹⁹, are the principle resident macrophages within the CNS⁹⁶. During embryogenesis, microglia, along with macrophages situated in various tissues, are derived from embryonic yolk sac (YS) myeloid progenitors¹⁰⁰. These YS progenitors migrate into the CNS throughout embryonic development, eventually colonizing within the CNS until the blood-brain barrier (BBB) is fully established¹⁰⁰.

After colonizing within the CNS, the early microglia initiate the maturation process. As revealed by comprehensive transcriptomic and epigenomic studies, microglial maturation occurs within several weeks postpartum¹⁰¹. This complex maturation process entails ongoing adaptation, ultimately enabling microglia to assume specialized physiological functions in support of the CNS⁹³.

Although microglia stem from YS progenitors, the maintenance of the microglial population does not depend on circulating myeloid cells. During physiological cell renewal or in pathological circumstances that demand additional microglia, these cells typically engage in self-renewal from the local pool¹⁰².

The endurance of individual microglia depends on the continuous activation of their colony-stimulating factor 1 receptor (CSF-1R). Previous studies have demonstrated that systemic CSF-1R inhibition leads to the expeditious depletion of the microglial population^{77,103}.

1.3.2 Microglia-dendritic spine interaction

As elucidated in previous sections, dendritic spines continually emerge^{48,72} and maintain structural plasticity^{48,72} in a predominantly activity- and experience-dependent manner^{75,76,104}, thereby upholding refined neural circuits and optimized cognitive performance⁶². During the postnatal maturation stages, roughly half of the dendritic spines undergo elimination following their formation¹⁰⁵. In subsequent developmental

phases, spanning adolescence and adulthood, a parallel process endures, albeit at generally attenuated yet dynamically fluctuating rates¹⁰⁶⁻¹⁰⁸.

The process of eliminating superfluous and inappropriate synaptic connections is orchestrated by both neuronal¹⁰⁹ and non-neuronal cells^{106,110,111}. Although a definitive division of labor between these cells remains elusive, microglia have emerged as pivotal players in this process, owing to their prominent phagocytic activity toward synaptic materials in healthy and pathological contexts¹⁰⁶⁻¹⁰⁸. Corroborating this notion, a plethora of previous investigations have revealed the presence of both pre- and postsynaptic constituents within microglia by employing electron microscopy techniques^{97,112}.

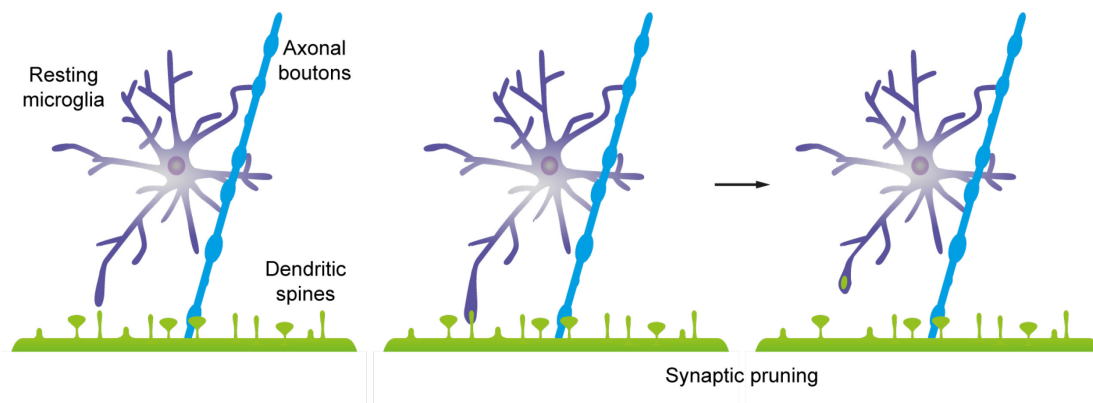


Figure 3 Synaptic pruning by microglia.

Microglia is one of the critical players that drives synaptic pruning. Resting microglia perpetually monitor the adjacent synapses and remove the superfluous or inappropriate dendritic spines.

Within the CNS, microglia perpetually shape the architecture of adjacent neural circuits by engulfing hypoactive synaptic components through a process designated as synaptic pruning (Fig. 3)⁹⁷. Nevertheless, the precise molecular mechanisms responsible for microglial discernment and subsequent phagocytosis of specific synapses or dendritic spines hitherto remain to be elucidated. A plethora of pathways has been implicated in the synaptic pruning process, encompassing the triggering receptor expressed on myeloid cells 2 (TREM2), the extracellular matrix (ECM), glutamate, C-X3-C motif chemokine receptor 1 (CX3CR1), the complement

cascade¹¹³⁻¹¹⁷, and a myriad of other potential elements¹¹⁸. Of these pathways, the complement-mediated synapse elimination paradigm has garnered broad acceptance. Within this framework, complement component 1q (C1q) – the inaugural molecule of the classical complement cascade – serves as a marker for both pre- and postsynaptic components. This labeling instigates the deposition of the downstream protein complement component 3 (C3) and the subsequent activation of complement receptor 3 (CR3) on the microglial surface. Ultimately, these occurrences converge in the microglial engulfment of the marked synaptic materials¹¹³⁻¹¹⁷.

It is essential to emphasize that these pathways do not inherently preclude one another. Within an intricate system such as the CNS, it stands to reason that the previously mentioned pathways function in concert with the complement-mediated mechanism to refine synaptic connections, consequently fostering optimized cognitive performance. It is entirely possible that these distinct processes regulate synaptic refinement in disparate contexts, incorporating a multitude of brain regions and developmental phases.

1.3.3 Altered microglia-dendritic spine interaction in CNS disorders

In response to a wide range of CNS disorders, microglia exhibit morphological alterations^{119,120} and various functional transformations¹²¹, including their interaction with dendritic spines, cytokine expression profiles¹²², and distinct genetic signatures¹²³⁻¹²⁵.

In a physiologically intact CNS, microglia display a ramified phenotype, characterized as the "resting" state, typified by elongated, branched structures and a relatively diminutive cellular soma. These extensive branches are extraordinarily sensitive and are incessantly surveying the proximate environment¹²⁶. Upon encountering CNS perturbations, microglia in varying states display a spectrum of morphological features, ranging from increasingly complex branching architectures with augmented

processes⁷⁷ to an amoeboid conformation typified by a pronounced enhancement in migratory capabilities¹²⁰.

Studies conducted on Alzheimer's disease (AD) mouse models have shown that the process of complement-mediated synaptic pruning is significantly intensified compared to wild-type (WT) counterparts, ultimately leading to an escalated engulfment of synaptic materials by microglia¹²⁷. Furthermore, in patients with LBD, the expression of the cluster of differentiation 68 (CD68), which is emblematic of microglial lysosomes¹²⁸, has been observed to be substantially augmented within the microglial population, indicating enhanced microglial phagocytic activity¹²⁹. In addition, investigations employing microglia and synaptic structures (synaptosomes) derived from individuals diagnosed with schizophrenia have also revealed an elevated rate of microglial engulfment of synaptic constituents when compared to healthy controls¹³⁰. Collectively, these findings indicate that microglia are a crucial driving force in the synaptic loss observed in CNS disorders that have a detrimental impact on cognitive functions (Fig. 4).



Figure 4 Schematic diagram of excessive spine loss upon altered synaptic pruning.

In the physiological state, microglial synaptic pruning attains a state of equilibrium, characterized by a dynamic balance between the elimination and formation of dendritic spines. However, in the context of CNS disorders, microglial dynamics are perturbed, resulting in hyperactive dendritic spine pruning and consequential significant synaptic loss.

In parallel with altered microglia-dendritic spine interaction, activated microglia also exhibit fluctuations in their cytokine expression patterns, encompassing, but not confined to, tumor necrosis factor- α (TNF- α), interleukin-1 β (IL-1 β), interleukin-6 (IL-6),

nitric oxide synthase (NOS), major histocompatibility complex class II (MHC II), and 18 kDa translocator protein (TSPO)¹²³⁻¹²⁵. In addition to cytokines, recent investigations leveraging single-cell RNA sequencing techniques have revealed the presence of microglial subpopulations distinguished by their genetic signatures, which are correlated with specific CNS disorders and thus referred to as "disease-associated microglia (DAM)"¹²³⁻¹²⁵.

These findings contribute not only to elucidating the underlying mechanisms altering microglial states and their subsequent implications on the CNS, but also provide opportunities for assessing the states of microglia and extrapolating microglia-associated pathophysiological conditions across a wide range of CNS disorders^{77,121}.

1.3.4 TSPO is a biomarker for microglial activity

As elucidated above, significant progress has been made in understanding and assessing microglial activity. However, most of this knowledge has been obtained through animal models and cell models derived from diverse sources. Therefore, to comprehend and evaluate microglial activity within the CNS *in vivo*, a biomarker compatible with non-invasive methodologies, such as PET, is imperative.

Numerous PET tracers have been utilized to determine microglial activity, such as cannabinoid receptor type 2 (CB2)¹³¹, cyclooxygenase-2 (COX-2)¹³², P2X₇ receptor¹³³, and TSPO¹³⁴. Among these tracers, TSPO is considered optimal due to its high sensitivity for alterations of microglial states in processes such as aging and CNS diseases^{135,136}.

TSPO was initially identified as the peripheral-type benzodiazepine receptor (PBR) due to its marked affinity for benzodiazepine diazepam¹³⁷. However, subsequent investigations revealed that it is neither solely affiliated with peripheral tissues nor exclusively bound to benzodiazepines. As a result, in recognition of its principal

function and molecular attributes, the nomenclature 18 kDa translocator protein was adopted¹³⁸.

TSPO is a phylogenetically conserved protein comprising five transmembrane domains, predominantly situated in the outer mitochondrial membrane¹³⁸. Its principal function is to serve as a rate-limiting determinant during the translocation of cholesterol from the outer to the inner mitochondrial membrane¹³⁸, a critical process in the biosynthesis of steroid hormones and neurosteroids^{137,138}. Nevertheless, observations from the mouse model with genetic depletion of TSPO revealed no adverse consequences on steroid biosynthesis¹³⁹, thereby casting doubt on the long-held assumption of TSPO's role in steroid production. In addition to this, prior studies have elucidated the potential involvement of TSPO in alternative biological functions, including mitochondrial homeostasis¹⁴⁰, and cellular apoptosis¹⁴¹.

Within the CNS, TSPO exhibits ubiquitous expression across a multitude of cell types, encompassing microglia, neurons, endothelial cells, and astrocytes^{77,142}. However, upon most CNS challenges, such as pharmacological stimuli⁷⁷ and CNS pathologies¹⁴³, the inducible augmentation of TSPO is predominantly observed in activated microglia¹⁴⁴, making it an appropriate tracer for the assessment of microglial activity.

1.3.5 Regulation of microglial states via TSPO

The role of TSPO in microglial activity goes beyond a simple depiction of this process. Numerous investigations have substantiated the intricate involvement of TSPO in regulating the activity of microglia.

Upon genetic depletion of TSPO, microglia display transformed metabolic processes and immune responses within the framework of neuroinflammation^{145,146}. Consequently, this results in diminished phagocytic activity towards oligomeric amyloid-beta (A β) in cultured microglia, and hindered microglial-mediated A β phagocytosis in the AD mouse models¹⁴⁵.

In addition to the effect of its genetic ablation, TSPO also serves as a receptor for a diverse array of synthetic ligands, modulating microglial functionality depending on the stimulation evoked by specific agents (Tab. 1).

Table 1 Representatives of synthetic TSPO ligands and their effects on microglia.

Class	TSPO ligand	Specificity to TSPO	Recorded effects on microglia
(Iso)quinoline carboxamide	PK11195, VC198M	Highly specific to TSPO ^{147,148}	MPT pore inhibition in isolated mitochondria ¹⁴⁹ Reduction of reactive astrocytes and microglia in the rat models of brain injury ^{150,151}
Phenylpurine acetamide	XBD173 (Emapunil)	Highly specific to TSPO ¹⁵²	Prevent microglial reactivity and gliosis in the retina of dark-adapted mice after acute light stimulation ¹⁵³ Prevent microglial migration, reactivity, and phagocytic capabilities in BV-2 microglial cell line and human microglial cell line ¹⁵⁴
Benzodiazepine	Diazepam	TSPO and γ - aminobutyric acid type A receptors (GABA _A Rs) ^{77,155}	Elevation of microglial TSPO and microglial engulfment of synaptic materials in WT mice, leading to impaired cognitive performance in WT mice ⁷⁷
	Ro5-4864	Highly specific to TSPO ¹⁵⁶	MPT pore inhibition in isolated mitochondria ¹⁴⁹ Reduction of reactive astrocytes and microglia in the rat models of brain injury ¹⁵⁰
Benzoxazine	Etifoxine	TSPO and GABA _A Rs ¹⁵⁷	Mitigation of microglia and macrophage activities in the rat model of brain trauma ¹⁵⁸

Notably, in a study my colleagues and I conducted, I observed a markedly increased activation of microglial TSPO following the administration of diazepam in WT mice. This TSPO activation engendered microglial morphological alterations and their heightened phagocytic activity towards synaptic materials. Ultimately, this outcome resulted in cognitive impairment in the diazepam-treated mice. Intriguingly, the effect

was nullified by the genetic depletion of TSPO, emphasizing the indispensability of TSPO in microglial-mediated synaptic engulfment⁷⁷.

1.3.6 Endogenous ligands of TSPO

The TSPO has been shown to have affinity not only for synthetic ligands but also for various endogenous ligands. Previous studies have demonstrated the presence of endogenous TSPO ligands both within and beyond the CNS (Tab. 2).

Cholesterol is a principal ligand for TSPO, demonstrating nanomolar (nM) affinity¹²³. Upon binding, this lipid molecule engages with the cholesterol recognition amino acid consensus sequence located within the C-terminal domain of TSPO¹⁵⁹. This interaction plays a critical role in TSPO-mediated cholesterol translocation and subsequent steroidogenesis^{137,138,160}.

Apart from the C-terminal domain of TSPO, specific endogenous TSPO ligands engage with analogous regions akin to synthetic ligand counterparts. Previous investigations have unveiled that an array of porphyrins or cyclic tetrapyrroles, including protoporphyrin IX (PPIX), mesoporphyrin IX, heme, and hemin¹⁶¹, retain a mutual region within their binding sites, analogous to the PK11195 binding site¹⁶², displaying high affinity¹⁶¹. Nevertheless, the biological ramifications of porphyrin-TSPO bindings have yet to be fully comprehended. It is possible that TSPO participates in the translocation of porphyrins into mitochondria, where these molecules contribute to the biogenesis of porphyrin-containing compounds, such as mitochondrial cytochromes¹⁶³.

In addition to cholesterol and porphyrins, TSPO also exhibits significant affinity for a class of acyl-coenzyme A binding domain-containing proteins (ACBD). Among this class, the most recent TSPO-binding member identified is acyl-coenzyme A binding domain-containing protein 3 (ACBD3), also known as PBR-associated protein 7

(PAP7)¹⁶⁴. It has been shown that ACBD3 is involved in translocating mitochondrial cholesterol and steroidogenesis¹⁶⁴.

Prior to the discovery of ACBD3, a member of the same family named acyl-coenzyme A binding domain-containing protein 1 (ACBD1)¹⁶⁵, otherwise referred to as the diazepam binding inhibitor (DBI), was identified as the first CNS TSPO-binding ACBD¹⁶⁶. DBI was initially detected within the rat brain¹⁶⁶, and has since undergone comprehensive investigations, becoming one of the most extensively studied and significant endogenous TSPO ligands within the CNS.

Table 2 Representatives of endogenous TSPO ligands and their functions.

TSPO ligand	Range of Binding affinity	Binding site	Recorded biological functions
Cholesterol	nM ¹²³	C-terminal domain of TSPO ¹⁵⁹	Steroid biosynthesis ^{137,138,160}
Porphyryns (cyclic tetrapyrroles)	nM ¹⁶¹	Partially shared with PK11195 ¹⁶²	Porphyrin-containing compounds biosynthesis ¹⁶³
ACBD1 (DBI)	μM ^{166,167}	N/A	Steroid biosynthesis ¹⁶⁸ , regulation of neurogenesis ¹⁶⁹ , regulation of oscillatory activity ¹⁶⁹ , formation of the acyl-CoA intracellular reservoir ¹⁷⁰⁻¹⁷² , metabolic functions ¹⁷³⁻¹⁷⁵
ACBD3 (PAP7)	N/A	N/A	Steroid biosynthesis ¹⁶⁴

1.4 Astrocytes and diazepam binding inhibitor (DBI)

Astrocytes were first observed and documented as neuroglia by Santiago Ramón y Cajal in the early 20th century⁴⁷. They are arborized cells that are highly abundant in the CNS¹⁷⁶. In addition to microglia, astrocytes also incessantly regulate dendritic spines via multiple pathways¹⁷⁷⁻¹⁸².

1.4.1 Physiology of astrocytes

Astrocytes are considered the most abundant glial cell type in the brains of humans and other mammals¹⁷⁶. While the proportion of astrocytes varies depending on the specific brain region¹⁷⁶, it is widely acknowledged that they constitute roughly 10% to 20% of all cells within a typical human brain^{99,183}.

During early embryonic development, astrocytes and oligodendrocytes are derived from neural stem cells in the neuroepithelium and propagate throughout the entire CNS¹⁸⁴. In contrast, microglia originate from YS myeloid progenitors and have a mesodermal or, more specifically, hematopoietic origin^{100,184}.

The morphology of astrocytes is highly heterogeneous, and their categorization is insufficiently defined¹⁸⁵. Take the cortical astrocytes as an example – a typical astrocyte possesses a highly arborized structure with diameters of 30 – 60 μm in rodents and 100 – 200 μm in humans¹⁸⁶, with its processes branching out radially in all directions from the cell body¹⁸⁶. However, in certain cases, such as residing next to vascular structures or approximating pathological entities like AD-induced dystrophic neurites, a significant portion of astrocytic processes moves in the corresponding direction to maintain the BBB or react to the pathological process, respectively^{186,187}. Additionally, the morphology of astrocytes is highly dynamic, with swift structural remodeling occurring in response to stimuli such as osmotic stimulation¹⁸⁸ and stress¹⁸⁹.

Astrocytes have multifaceted roles that encompass almost every aspect of CNS development, homeostasis, and reactions to pathologies¹⁹⁰. They constantly maintain CNS structural integrity¹⁹¹ and metabolic functions¹⁹², regulate the BBB¹⁹³, and control blood flow across the brain¹⁹⁴. Moreover, astrocytes are involved in producing and distributing various neurotransmitters^{195,196} and ions¹⁹⁷ in perisynaptic areas, thereby regulating synapses¹⁹⁸. Additionally, astrocytes play crucial roles in the myelinating process¹⁹⁹, supporting neuronal pathways in the white matter. Furthermore, astrocytes regulate CNS immune processes by becoming reactive and expressing multiple

cytokines in response to various CNS challenges^{200,201}. However, it is essential to note that astrocytes conduct all these functions heterogeneously within the CNS, leading to a multitude of diverse astrocytic functionalities¹⁸⁵.

The fundamental division of grey matter "protoplasmic" astrocytes and white matter "fibrous" astrocytes was described over a century ago, and has been supported by continuous observations^{202,203}. As research on astrocytes advances, more detailed information and complex categories utilizing advanced morphological analysis²⁰⁴, transcriptomic profiling^{205,206}, and Ca²⁺ activity recording²⁰⁷ have been proposed to further elucidate astrocytic heterogeneity¹⁸⁵. Moreover, specialized cells with astrocytic properties have been identified, such as retinal Müller cells and cerebellar Bergmann glial cells²⁰⁸.

In this study, I focus on protoplasmic astrocytes, the primary type of astrocytes located in grey matter and closely associated with synapses²⁰⁹. It has been consistently observed that protoplasmic astrocytes actively engage in synapses in the majority of brain regions of mammalian animals²¹⁰.

1.4.2 Astrocytes regulate synapses via secretory pathways

Within grey matter, astrocytes are intimately associated with a significant number of adjacent synapses^{182,209,211}. A typical astrocyte in the rodent brain occupies an approximate volume of 66,000 μm^3 , containing around 90,000 synapses²¹². By extrapolating to humans, it is estimated that each astrocyte covers about 2 million synapses²⁰⁴, stating the significant influence that astrocytes may exert over synaptic functions.

The astrocytic regulation of dendritic spines is accomplished predominantly through the secretion of signaling molecules²¹³. As demonstrated in previous studies, there are three principal routes of astrocytic secretion: vesicle-based exocytosis, diffusion through the plasma membrane, and transmembrane transport²¹³. These routes enable

the transmission of signaling molecules between astrocytes and synapses through extracellular space and direct contact^{213,214}, facilitated by perisynaptic astrocyte processes²¹⁴.

As shown in prior investigations, astrocytes play a crucial role in the synaptic formation. The introduction of astrocytes to glial-free neuronal cultures has resulted in a substantial increase in fully developed and functional synapses by several-fold^{215,216}. Since then, the astrocyte-induced synaptic formation has been substantiated by an accumulating body of evidence on different types of synapses, such as glutamatergic²¹⁶, cholinergic^{217,218}, glycinergic²¹⁹, and GABAergic²²⁰, through diverse signaling pathways involving various components such as thrombospondin¹⁷⁷, glypican¹⁷⁹, and transforming growth factor- β 1 (TGF- β 1)¹⁸⁰⁻¹⁸².

In addition to their role in the synaptic formation, astrocytes are known to regulate synaptic transmission and their structural plasticity through various signaling pathways, involving the secretion of astrocyte-derived factors such as adenosine triphosphate (ATP)^{221,222}, glutamate²²³⁻²²⁶, secreted protein acidic and cysteine-rich (SPARC)^{94,227}, hevin^{227,228}, and TNF- α ²²⁹.

1.4.3 Astrocytes-microglia interaction in health and diseases

In the CNS, the regulatory function of astrocytes on synapses also goes through other glial cell types, particularly microglia^{230,231}. The astrocyte-microglia interaction has been reported to affect synaptic regulation across physiological and pathological conditions^{230,231}.

Recent research has demonstrated that during the normal aging process, astrocytes secrete interleukin-33 (IL-33), which has been shown to promote microglial synapse engulfment during development, thereby facilitating the normal maturation and remodeling of neural circuits²³⁰. Furthermore, in a mouse model of AD, astrocytes were observed to produce an increased level of C3, which enhances the C3-CR3 signaling

pathway²³² and leads to an increased microglial engulfment of synapses¹²⁷. In addition to C3, astrocytes also regulate microglia behavior under AD pathology through the interleukin-3 (IL-3)-interleukin-3 receptor α (IL-3R α) signaling pathway²³¹. This pathway modulates microglial motility and clearance of A β and tau aggregates, which are known to trigger synaptic dysfunctions^{233,234}.

In addition to the cytokines mentioned above, prior investigations have highlighted that DBI, a principal endogenous ligand for TSPO in the CNS, is among the abundantly secreted molecules from astrocytes in both healthy and pathological states²³⁵.

1.4.4 Astrocytes are the primary DBI source in the CNS

In the CNS, the expression of DBI is mainly observed in cells of glial nature, such as astrocytes^{236,237}, tanycytes²³⁶, and ependymal cells²³⁸. Previous studies have demonstrated that cultured astrocytes express a significant amount of DBI^{236,237,239-241}, indicating their role as the primary DBI producer in the CNS.

Apart from DBI production, astrocytes also play a crucial role in DBI secretion²³⁵. DBI is generally released through the unconventional secretory pathway^{175,240,242-245}. Unlike most neuropeptides that undergo processing by prohormone convertases, such as proprotein convertase subtilisin/kexin type 1 (PCSK1) and proprotein convertase subtilisin/kexin type 2 (PCSK2), within the endoplasmic reticulum and are then transported to the Golgi apparatus for packaging into dense core vesicles before release^{246,247}, DBI remains localized in the cytoplasmic compartment after its translation²⁴⁸. From astrocytes, DBI is primarily secreted through vesicle-based exocytosis²⁴⁹, which is dependent on Golgi-associated proteins, such as Golgi reassembly stacking protein (GRASP), and the formation of autophagosomes²⁴⁸. However, the specific mechanisms regulating DBI secretion may be intricate and dependent on the context²⁵⁰.

Furthermore, extensive investigations have revealed that several signaling pathways, including the adenylyl cyclase/protein kinase A transduction²⁵¹, somatostatin receptor⁴²⁵², and *N*-formyl peptide receptor²⁵³, modulate DBI release through astrocytes^{245,251-253}, thereby establishing astrocytes as the primary target for regulating DBI secretion within the CNS.

Collectively, these investigations highlight astrocytes as the primary source of DBI in the CNS, with their capability in DBI secretion exhibiting high sensitivity to different regulatory pathways across various CNS states.

1.4.5 DBI is an ancestral protein with diverse and emerging functions

DBI is a small (~10 kDa) and phylogenetically conserved ancestral protein²⁵⁴. The name of the diazepam binding inhibitor originates from its inherent ability to displace benzodiazepines, such as diazepam, from both their target receptors - GABA_AR and TSPO – demonstrating a potent affinity (micromolar, μM) towards these binding sites^{166,167}.

Extensive research has revealed that, as a secretory protein, DBI executes a myriad of biological functions within the CNS through interactions with GABA_ARs. For instance, DBI acts as a positive allosteric modulator through its association with GABA_ARs, targeting specifically the $\alpha 3$ subunit in the thalamic reticular nucleus²⁵⁵. This engagement mitigates oscillatory activity in thalamocortical networks, subsequently inhibiting absence seizures in the mouse model²⁵⁵. In contrast, functioning as a negative allosteric modulator, DBI engages with the $\gamma 2$ subunits of GABA_ARs, orchestrating neural progenitor proliferation through GABA signaling and thereby regulating neurogenesis¹⁶⁹.

Apart from its GABA-related actions, secreted DBI exerts regulatory influence by binding to TSPO. Previous investigations have shown that persistent exposure to DBI stimulates steroidogenesis, augmenting steroid biosynthesis by 1.5 to 3-fold within a

few minutes in steroidogenic cell lines¹⁶⁸. Notably, these effects can be obstructed by TSPO ligands, such as flunitrazepam¹⁶⁸, suggesting that the process of DBI-induced steroidogenesis occurs in a TSPO-dependent manner.

As previously mentioned, DBI is alternatively designated as acyl-coenzyme A binding domain-containing protein 1 (ACBD1)¹⁶⁵ or acyl-coenzyme A binding protein (ACBP), indicative of its substantial affinity (nM) for long-chain acyl-coenzyme A (LCACoA) esters²⁵⁶. In this capacity, DBI functions as an acyl-coenzyme A transporter intracellularly, contributing to the formation of the acyl-coenzyme A intracellular reservoir¹⁷⁰⁻¹⁷². This particular aspect of DBI was initially discovered in bovine hepatic tissue²⁵⁷, a mere half-decade subsequent to the unearthing of DBI in the rat brain¹⁶⁶. In the ensuing years, a plethora of substantiating evidence has emerged, underscoring the notion that the implications of DBI reach far beyond the confines of the CNS. As evidenced by preceding investigations, DBI manifests in a diverse assortment of peripheral tissues such as skin keratinocytes^{173,174}, hepatocytes, and peripheral blood mononuclear cells¹⁷⁵. Within these respective tissues, DBI is involved in a multifaceted array of metabolic processes, encompassing the maintenance of normal systemic energy expenditure¹⁷³ and epidermal barrier function¹⁷⁴, as well as the modulation of lipolysis, feeding behavior, and body weight¹⁷⁵.

1.4.6 Alterations of DBI in CNS disorders

Despite the multifaceted functionality of DBI in the CNS and its role as an endogenous ligand for TSPO – the commonly used tracer for microglia activity assessment in various CNS pathologies – there is no established or universally accepted association between DBI and microglia. Research on DBI alterations in different CNS pathologies is less centralized, with limited elucidation on the underlying mechanisms that elucidate the implication of DBI on microglial activity and regulation of dendritic spines.

Though the quantity of research is restricted, discrepancies in DBI concentrations have been consistently observed between healthy individuals and those suffering from CNS pathologies such as neurodegenerative, neuroinflammatory, neurodevelopmental, and psychiatric disorders²⁵⁸⁻²⁶². Specifically, aberrantly elevated DBI levels have been identified in patients diagnosed with AD^{258,259}, multiple sclerosis²⁵⁸, delirium²⁵⁹, and acute stress^{260,261}. Conversely, by employing a combination of cluster analysis of the Autism Diagnostic Interview-Revised scores obtained from 85 autistic spectrum disorder (ASD) patients and proteomic profiling of lymphoblastoid cells extracted from these individuals through 2D gel electrophoresis and mass spectrometry, it has been ascertained that in cases of severe language deficits, DBI concentrations in ASD patients are markedly reduced²⁶². However, how DBI alterations correlate to the progression of these CNS pathologies remains to be further explored.

1.5 *In vivo* two-photon imaging

As described in the above sections, impaired structural plasticity of dendritic spines has been consistently observed in LBD pathology. However, the precise mechanisms facilitating this process have yet to be fully elucidated. Concomitantly, within the CNS, astrocytes engage in intricate interactions with microglia, modulating the structural plasticity of dendritic spines in both healthy and pathological states. However, how this glial interplay influences dendritic spines in LBD remains largely unknown.

The primary objective of this dissertation is to scrutinize the potential impacts of astrocyte-microglia crosstalk, specifically through the ligand-receptor dyad of DBI and TSPO, on dendritic spines in LBD pathology. To achieve this aim, I intend to systematically examine alterations in astrocytic DBI and microglial TSPO in both the mouse model and postmortem human brain tissues exhibiting LBD pathology. Additionally, I will evaluate the interactions between these two constituents and the resulting implications on microglial functionality, with particular emphasis on their

engulfment towards synaptic materials. Correspondingly, I will trace the alterations of dendritic spines along LBD pathophysiology. On top of this, I will manipulate this process by selectively suppressing either DBI or TSPO and systematically monitor and analyze the resulting impacts on dendritic spine plasticity under the respective experimental paradigms.

As emphasized before, dendritic spines are highly dynamic structures that undergo continual fluctuations in their formation and elimination. Therefore, to obtain a comprehensive understanding of dendritic spine plasticity, it is necessary to conduct longitudinal investigations spanning extended periods of time, rather than relying solely on singular temporal evaluations. In this study, I utilized *in vivo* two-photon microscopy, coupled with a transgenic mouse model expressing the enhanced green fluorescent protein (eGFP) in specific subsets of neurons⁷¹. This integrated methodology enabled the monitoring of dendritic spines in living animals over an extended timeframe, thereby allowing for a more rigorous and detailed analysis of their inherent plasticity.

The two-photon excitation-based microscopy, initially demonstrated by Wolfgang Kaiser in 1961²⁶³, represents a milestone in the field of fluorescence microscopy. The underlying principle of this process aligns with conventional fluorescent microscopy, wherein fluorophores are stimulated from their ground state (S_0) to an excited state (S_1) by the absorption of photons with a specific energy level. Subsequently, the excited fluorophores release the absorbed energy in the form of emitted light, which is then captured by microscopic detectors and interpreted as visible images²⁶⁴. However, unlike conventional methods that excite one fluorophore using a single photon with relatively high energy, the two-photon excitation process employs two photons with the lower energy that converge on the same fluorophore within a few femtoseconds. The combined energy of these two photons effectively elevates the fluorophore to the desired excited state, leading to subsequent light emission (Fig. 5)⁷⁰.

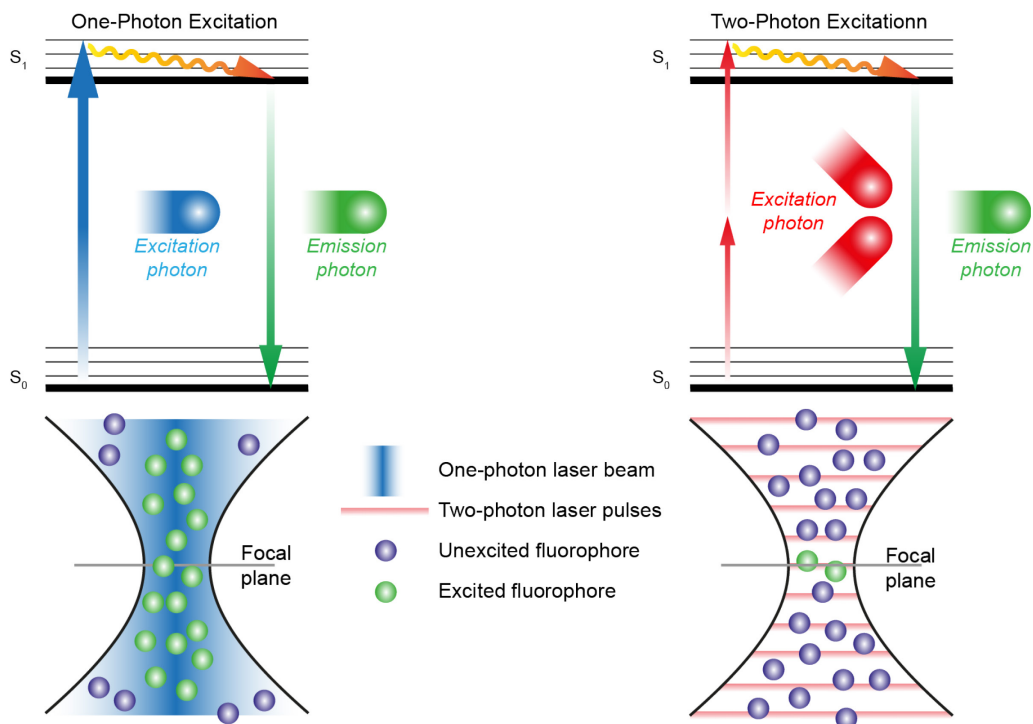


Figure 5 Outline of one-photon and two-photon excitation.

One-photon excitation is typically utilized in confocal microscopy. This involves applying a laser beam of photons with sufficient energy to the samples, which excites all fluorophores from their ground state (S_0) to their excited state (S_1) along the optical path. Subsequently, the excited fluorophores emit light and return to the S_0 state. On the other hand, two-photon excitation is commonly used in *in vivo* microscopy. This technique involves the selective excitation of fluorophores within a specific optical section using lower energy laser pulses.

The utilization of two-photon excitation for microscopic imaging offers several distinct advantages. Notably, photons with lower energy levels possess longer wavelengths (Tab. 3), allowing for enhanced tissue penetration compared to short wavelengths²⁶⁵. On average, a two-photon microscope can image tissues up to a depth of approximately 1 mm, surpassing confocal microscopy by 2 to 3 times. Moreover, longer wavelengths are less scattered while traversing tissue layers, making them well-suited for high-resolution imaging²⁶⁶. Additionally, as illustrated in Fig. 5, two-photon excitation occurs selectively within a certain optical section. This eliminates the need for a pinhole, a crucial component in confocal microscopy, to block the detection of excited fluorophores from other optical sections, thus simplifying the overall microscope configuration⁷⁰. Furthermore, the reduced total energy absorbed by tissue

in two-photon microscopy significantly mitigates phototoxicity during imaging, a critical consideration for longitudinal imaging of living animals.

Table 3 Commonly used fluorophores and two-photon excitation wavelengths.

Fluorophore	Excitation (nm) ^{77,267}	Emission (nm)
Enhanced Cyan Fluorescent Protein (eCFP)	850 – 860	477
eGFP	880 – 970	511 – 521
Enhanced Yellow Fluorescent Protein (eYFP)	920 – 970	530

In line with the advantages mentioned above, no detrimental effects were detected in any control animals during the longitudinal *in vivo* imaging of dendritic spines in the mouse brains.

2. Methods

2.1 Animals

All procedures and protocols involving animal experiments were conducted in compliance with the regulations of the Ludwig Maximilian University of Munich and were authorized by the Upper Bavarian government. The animal subjects used in this investigation, both the WT mice and those that underwent genetic modification, were of the C57BL/6 lineage²⁶⁸. For each experiment, only mice between 2 to 4 months of age and with comparable sex distribution were employed unless otherwise specified.

To model certain traits of LBD, the *Tg(PDGFB-SNCA)^{4Ema} (PDGF-h- α -syn)* mice were procured from QPS Austria Neuropharmacology (Grambach, Austria). These mice overexpress the WT human α -synuclein gene through the human platelet-derived growth factor (PDGF) b-chain (PDGF- β) promoter, restrained in neurons²⁶⁹. For the genetic ablation of TSPO from the CNS, global TSPO knockout (*C57BL/6-Tspo^{tm1GuMu(GuwiyangWurra)}, Tspo^{-/-}*) mice were generated as previously described²⁷⁰. The GFP-M (*Thy1-eGFP*) transgenic mice were obtained from Jackson Laboratory and maintained as heterozygous to enable the visualization of dendritic spines *in vivo* and *ex vivo*. In these mice, cortical layer 5 – 6 pyramidal neurons of restrained subpopulations are sparsely labeled with enhanced green fluorescent protein governed by the thymocyte differentiation antigen 1 (Thy1) promoter⁷¹. Other double- or triple-transgenic mice, such as *Thy1-eGFP:PDGF-h- α -syn* mice, *PDGF-h- α -syn:Tspo^{-/-}* mice, and *Thy1-eGFP:PDGF-h- α -syn:Tspo^{-/-}* mice, were bred through interbreeding with mice of each transgene and maintained as in the original strain. All mouse lines used in this study are listed in Tab. 4.

All animal subjects were housed at the Centre for Neuropathology animal facility at the Ludwig Maximilian University of Munich, bred under pathogen-free conditions (with the

room temperature at 21 ± 1 °C and a 12 h light/12 h dark cycle), and provided with *ad libitum* access to food and water.

Table 4 Mouse strains used in this study.

Symbol	Reference	MGI ID
<i>B6.Cg-Tspo^{tm1.1Guwu}</i>	Banati <i>et al.</i> , 2014	5603428
<i>B6.Cg-Tspo^{tm1.1Guwu} : Tg(Thy1-eGFP)MJrs/J</i>	This dissertation	N/A
<i>C57BL/6J</i>	Wallace, 1950	3028467
<i>Tg(PDGFB-SNCA)4Ema</i>	Masliah E, <i>et al.</i> , 2000	1353749
<i>Tg(PDGFB-SNCA)4Ema : B6.Cg-Tspo^{tm1.1Guwu}</i>	This dissertation	N/A
<i>Tg(Thy1-eGFP)MJrs/J</i>	Ralvenius <i>et al.</i> , 2015	3766828
<i>Tg(Thy1-eGFP)MJrs/J : B6.Cg-Tspo^{tm1.1Guwu}</i>	This dissertation	N/A
<i>Tg(Thy1-eGFP)MJrs/J : Tg(PDGFB-SNCA)4Ema</i>	This dissertation	N/A
<i>Tg(Thy1-eGFP)MJrs/J : Tg(PDGFB-SNCA)4Ema : B6.Cg-Tspo^{tm1.1Guwu}</i>	This dissertation	N/A

2.2 Genotyping

The genotypes of all genetically modified mice were determined utilizing methods in accordance with the provider's guidelines with in-house modifications. To summarize, tissues were harvested in mice between 12 to 14 days old from the tip of the tail, approximately 3 mm in length, or from the ear, approximately 2 mm in diameter. Tissues were subsequently stored at -20 °C until further analysis. The genomic DNA was extracted using the Quantabio Extracta DNA Prep for PCR (Quantabio, USA). Thereafter, specific transgenic constructs were amplified via polymerase chain reaction (PCR) using the OneTaq Hot Start Quick-Load (NEB, USA) coupled with corresponding primers, as detailed in Tab. 5. Each amplified sample was then subjected to electrophoresis on 1.5% to 2% agarose gels with ethidium bromide staining. Finally, genotype validation was achieved by interpreting specific bands. All primers used in this study are listed in Tab. 5.

Table 5 Primers for genotyping.

Strain	Primer	Sequence (5'-3')	Length (bp)
<i>Thy1-eGFP</i>	IMR 0872	AAG TTC ATC TGC ACC ACC G	19
	IMR 1416	TCC TTG AAG AAG ATG GTG CG	20
<i>PDGF-h-α-syn</i>	209F	CTG GAA GAT ATG CCT GTG GA	20
	50R	CAT CAA TGT ATC TTA TCA TGT CTG GAT TCT	29
<i>Tspo^{-/-}</i>	P1	GGT AGA CTA GTG TGG GAA GAT TTG A	25
	P2	ATG GTG ATT GCA ACT GAT GTT C	22
	P3	TAG ATA CTG ACC CTA TCT GGG ATG T	25

2.3 Drug administration

To pharmacologically deplete microglia from the CNS, a potent inhibitor of the CSF-1R, PLX5622, was administered as a supplement of AIN-76A standard chow (Research Diets, USA) at a concentration of 1200 ppm (Plexxikon, USA).

For *in vivo* two-photon imaging, mice were fed the PLX5622-mixed diet or a control diet *ad libitum* for a period of two weeks before the first imaging session and throughout the entire imaging period (in total 8 weeks). To confirm the extent of microglia depletion in the cortical region, immunostaining coupled with 3D reconstruction and analysis was performed (Fig. 22).

2.4 Postmortem human brain tissue

All scientific investigations involving human samples were carried out in strict accordance with established ethical standards, and received approval from the Ethics Committee at Ludwig Maximilian University under registration number 17-722. Tissue sample collection was executed under registration number GA2017-5.

The Neurobiobank Munich at the Ludwig Maximilian University of Munich supplied all of the brain samples from patients diagnosed with Lewy body dementia (PDD/DLB) as well as from healthy donors. Formalin-fixed paraffin-embedded (FFPE) sections from

the frontal cortex, with a thickness of 5 μm , were provided for immunostaining purposes. For the LBD group, tissue was collected from patients with pathologically confirmed cases of Lewy body disease at stages Braak 1-6, which includes incidental findings. For the control group, tissue was procured from donors who were pathologically excluded from Lewy-related pathology. A detailed description of both groups is included in Tab. 6. To execute the study in a blinded fashion and maintain data anonymity, the pseudonyms of LBD and non-LBD samples from the Neurobiobank were randomly replaced with new numerical pseudonyms.

Table 6 Characterization of postmortem human tissue samples used in this study.

Pseudo-nym	Group	Braak LBD	Brain region	Age	Gender	Clinical diagnosis
#2	Case	1	Medial frontal gyrus	95	Female	Restless-Legs Syndrom
#5	Case	2	Medial frontal gyrus	60	Male	Gastric cancer
#1	Case	3	Medial frontal gyrus	87	Female	Schizophrenia
#7	Case	6	Medial frontal gyrus	79	Female	Parkinson's disease
#4	Case	6	Medial frontal gyrus	78	Female	Dementia
#8	Case	6	Medial frontal gyrus	81	Female	Parkinson's disease dementia
#6	Control	0	Medial frontal gyrus	42	Male	No neurological or psychiatric diseases
#3	Control	0	Medial frontal gyrus	71	Female	No neurological or psychiatric diseases
#9	Control	0	Medial frontal gyrus	82	Female	Gall bladder carcinoma

2.5 Perfusion

Unless otherwise specified, all mice included in the study underwent transcatheter perfusion prior to the extraction of brain tissue. Prior to the perfusion, each mouse was sedated by intraperitoneal injection of a mixture containing ketamine and xylazine at concentrations of 100 mg/kg body weight and 20 mg/kg body weight, respectively. The

state of anesthesia was evaluated using the pedal reflex, specifically by toe pinching. Upon achieving adequate sedation, the mouse was subjected to a two-phased transcardial infusion involving ice-cold phosphate-buffered saline (PBS) followed by a 4% paraformaldehyde (PFA) solution (Roth, Germany). Following the completion of the perfusion, the brain was extracted. The extracted brain tissue was then immersed immediately in a 4% PFA solution for a duration of 24 h before being stored in PBS at a temperature of 4 °C in anticipation of further sectioning.

2.6 Immunostaining

In the case of mouse brain tissue, the obtained brains were sliced into 50 µm sections using a Leica VT1200 vibratome (Leica, Germany). The free-floating sections of regions of interest were then permeabilized overnight at room temperature in a PBS solution containing 2% Triton X-100 (Sigma Aldrich, USA). Following this, the sections were subjected to a blocking step, which consisted of incubating the sections in a blocking buffer for 4 to 5 h at room temperature. The blocking buffer consisted of 10% normal goat or donkey serum (Sigma Aldrich, USA), 2% bovine serum albumin (Sigma Aldrich, USA), and 0.3% Triton X-100 PBS or 3% I-Block (Invitrogen, USA). Once the sections were properly blocked, they were incubated at 4 °C for 24 to 48 h with respective sets of blocking-buffer-diluted primary antibodies (Tab. 7). The sections were then washed three times for 10 min in PBS and incubated in corresponding blocking-buffer-diluted secondary antibodies (Tab. 7) for 4 h at room temperature. Following thorough washing in PBS, the stained sections were mounted on microscope slides using the fluorescence mounting medium (Dako, Germany) and then covered by coverslips. Before imaging, all slides were kept at 4 °C and out of direct light to ensure proper preservation of the stained sections.

In the case of human brain tissues, all samples were provided in ~5 µm FFPE sections pre-adhered to microscope slides and stored at 4 °C prior to immunostaining. To begin

the immunostaining process, the sections were deparaffinized with 100% xylene (Sigma Aldrich, USA) and then immersed in variously diluted ethanol solutions (100%, 95%, 70%, 50%) (Roth, Germany) to be rehydrated. Subsequently, the rehydrated sections underwent a heat-induced epitope retrieval step by incubating them at 120 °C for 3 minutes in an epitope retrieval solution (Abcam, USA). After the retrieval procedure, the sections were immersed in tap water for cooling down to room temperature. Upon reaching room temperature, the epitope-retrieved sections were subjected to the staining process in a humidity chamber (Merck, Germany), following a similar procedure as that of the mouse brain sections. The staining of the human brain tissue sections was conducted using various combinations of primary and secondary antibodies, the details of which are listed in Tab. 7.

Table 7 Antibodies used in this study.

Antibodies	Source	Identifier
Rat Monoclonal Anti-CD68	Bio-Rad	Cat# MCA1957; RRID: AB_322219
Rabbit Monoclonal Anti-DBI	Frontier Institute	Cat# DBI-Rb-Af300; RRID: AB_2571690
Rabbit Polyclonal Anti-DBI	Atlas Antibodies	Cat# HPA051428, RRID:AB_2681482
Rabbit Monoclonal Anti-GAPDH	Cell Signaling Technology	Cat# 5174; RRID: AB_10622025
Mouse Monoclonal Anti-GFAP	Abcam	Cat# ab49874; RRID: AB_880203
Rabbit Polyclonal Anti-GFP	Thermo Scientific	Cat# A-21311; RRID: AB_221477
Rabbit Polyclonal Anti-GLUT-1	Millipore	Cat# 07-1401; RRID: AB_11212210
Guinea Pig Polyclonal Anti-Iba1	Synaptic Systems	Cat# 234 308; RRID: AB_2924932

Antibodies	Source	Identifier
Rabbit Polyclonal Anti-mCherry	Abcam	Cat# ab167453; RRID:AB_2571870
Mouse Monoclonal Anti-NeuN	Millipore	Cat# MAB377; RRID: AB_2298772
Rabbit Monoclonal Anti-PBR	Abcam	Cat# ab109497; RRID: AB_10862345
Goat Polyclonal Anti-PBR	Abcam	Cat# ab118913; RRID: AB_10898989
Recombinant Anti-PBR [EPR5384]	Abcam	Cat# ab213654; RRID: N/A
Rabbit Polyclonal Anti-PCNA	Cell Signaling Technology	Cat# 13110; RRID: AB_2636979
Goat Polyclonal Anti-PSD95	Abcam	Cat# ab12093; RRID:AB_298846
Mouse Monoclonal Anti-PSD95	Synaptic Systems	Cat# 124 011; RRID: AB_10804286
Rabbit Monoclonal Anti-PSD95	Cell Signaling Technology	Cat# 3450; RRID: AB_2292883
Rabbit Polyclonal Anti-Stathmin	Cell Signaling Technology	Cat# 3352; RRID: AB_330234
Rabbit Monoclonal Anti-Synaptophysin	Cell Signaling Technology	Cat# 5461; RRID: AB_10698743
Guinea Pig Polyclonal Anti-S100B	Synaptic Systems	Cat# 287 004; RRID: AB_2620025
Rabbit Polyclonal Anti-Transferrin	Abcam	Cat# ab82411; RRID: AB_1659060
Normal Rabbit IgG	Cell signaling technology	Cat# 2729; RRID: AB_1031062
Alexa Fluor 488 AffiniPure Donkey Anti-Guinea Pig IgG (H+L)	Jackson ImmunoResearch Labs	Cat# 706545148; RRID: AB_2340472

Antibodies	Source	Identifier
Alexa Fluor 647-AffiniPure Donkey Anti-Guinea Pig IgG (H+L)	Jackson ImmunoResearch Labs	Cat# 706-605-148, RRID:AB_2340476
Donkey Anti-Mouse IgG (H+L) Highly Cross Adsorbed Secondary Antibody, Alexa Fluor 594	Thermo Scientific	Cat# A-21203; RRID: AB_141633
Donkey Anti-Rat IgG H&L (Alexa Fluor 647) Preadsorbed	Abcam	Cat# ab150155, RRID:AB_2813835
Donkey Anti-Rabbit IgG (H+L) Highly Cross-Adsorbed Secondary Antibody, Alexa Fluor 647	Thermo Scientific	Cat# A-31573, RRID:AB_2536183
Donkey Anti-Mouse IgG (H+L) Highly Cross-Adsorbed Secondary Antibody, Alexa Fluor Plus 488	Thermo Scientific	Cat# A32766, RRID:AB_2762823
Donkey Anti-Goat IgG (H+L) Highly Cross-Adsorbed Secondary Antibody, Alexa Fluor Plus 555	Thermo Scientific	Cat# A32816, RRID:AB_2762839
Donkey Anti-Rabbit IgG (H+L) Highly Cross-Adsorbed Secondary Antibody, Alexa Fluor Plus 594	Thermo Scientific	Cat# A32754, RRID:AB_2762827
Goat Anti-Rabbit IgG, HRP-Conjugated	Cell Signaling Technology	Cat# 7074, RRID: AB_2099233

2.7 Proximity ligation assay (PLA)

To investigate the interaction between DBI and TSPO, the proximity ligation assay (PLA) was employed²⁷¹. Prior to the experiment, protein-specific PLA probes were generated by incubating rabbit-derived antibodies against DBI and TSPO with anti-rabbit lyophilized oligonucleotides (PLA probe PLUS and MINUS) (Sigma Aldrich, USA) at ambient temperature for 30 min, with gentle agitation. The process of conjugation was subsequently terminated by the addition of the stop solution provided with the probes, and the oligonucleotide-conjugated antibodies were kept at 4 °C until the subsequent steps.

The PLA was conducted using the Duolink *In Situ* Detection Reagents kit (Sigma Aldrich, USA) according to the manufacturer's instructions. Briefly, sections of mouse brains were affixed to SuperFrost Adhesion slides (Eprelia, USA), and permeabilized by being kept overnight at room temperature in PBS containing 2% Triton X-100. Following the permeabilization, the sections were blocked at room temperature for 2 to 3 h with a blocking buffer comprising 10% normal donkey serum and 2% bovine serum albumin in 0.3% Triton X-100 PBS. After the blocking procedure, the sections were incubated at 4 °C for 24 to 48 h with the blocking buffer-diluted unconjugated primary antibodies against ionized calcium binding adaptor molecule 1 (Iba1), PSD95, and CD68 (Tab. 7), as well as oligonucleotide-conjugated antibodies. The sections were then washed thoroughly multiple times in PLA wash buffer A (Sigma Aldrich, USA) to eliminate any unbound antibodies after the incubation. Next, the sections were kept at room temperature for 1 h with the blocking buffer-diluted secondary antibodies (Tab. 7) that detect unconjugated primary antibodies. After the 1-h incubation, the sections were repeatedly washed with PLA wash buffer A. To induce ligation between the oligonucleotides that were conjugated to the DBI and TSPO antibodies and produce detectable PLA signals, ligation buffer (Sigma Aldrich, USA) and amplification buffer (Sigma Aldrich, USA) were applied to the sections and incubated at 37 °C for 30 min and 100 min, successively (Fig. 6). Following the amplification step, the brain sections were washed with PLA wash buffer B (Sigma Aldrich, USA), mounted with Duolink *In Situ* Mounting Medium with DAPI (Sigma Aldrich, USA), and covered with coverslips. The PLA-probed sections were then kept at 4 °C in complete darkness and imaged within one week.

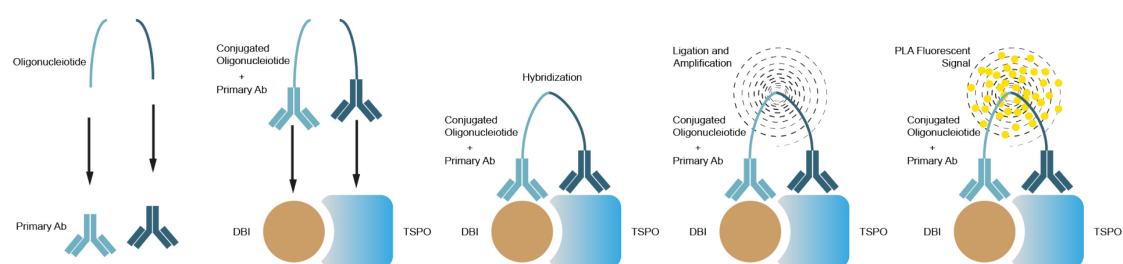


Figure 6 Schematic diagram of the PLA reaction.

The diagram illustrates that the oligonucleotide-conjugated antibodies in close proximity bind and generate detectable fluorescent signals.

2.8 Brain extracellular fluid (ECF) collection

To preserve the integrity of brain tissue and cells while collecting protein from the mouse brain extracellular fluid (ECF), mice were deeply sedated using the aforementioned ketamine/xylazine mixture. Next, sedated mice were perfused with ice-cold PBS for a period of 2 min. The brains were then promptly extracted and immersed in ice-cold PBS containing a 1× protease/phosphatase inhibitor (Thermo Fisher Scientific, USA) for a period of 4 h. Following the immersion, the PBS was gathered and subjected to centrifugation at a rate of 14,000× g for 30 min in order to eliminate any remaining cellular debris. The total protein concentration in the collected PBS was subsequently quantified using the bicinchoninic acid (BCA) assay (Thermo Scientific, USA). After adjusting the protein concentration to 1.5 mg/mL ECF, the resulting brain ECF was frozen at -80 °C. This sample was then reserved for subsequent analyses and use.

2.9 Immunodepletion

To deplete DBI from the *PDGF-h-α-syn* brain ECF, an antibody targeting DBI (Tab. 7) was solubilized in brain ECF at a concentration of 10 µg/mL, followed by thorough pipetting. The antibody-brain ECF mixture was subsequently incubated overnight at 4 °C with consistent stirring utilizing a HulaMixer (Thermo Scientific, USA). Following the incubation period, Dynabeads Protein G (Invitrogen, USA) was introduced into each sample at a concentration of 150 µL/mL sample volume and allowed to incubate for a duration of 30 min at room temperature. Thereafter, all the samples were placed on a DynaMag-2 Magnet (Invitrogen, USA) to extract the Dynabeads-antibody-DBI complex from the supernatant. The DBI-neutralized supernatant was collected and cryopreserved at -80 °C until subsequent experiments.

2.10 Primary astrocytes and microglia isolation

In order to isolate astrocytes and microglia from the cerebral cortex of mice, the rodents were terminated via cervical dislocation, and their brains were immediately harvested. After excising the cerebellum and all subcortical tissue, including the hippocampus and midbrain, cortical tissue from the cerebrum was extracted. The Adult Brain Dissociation Kit (Miltenyi Biotec, Germany) was employed to isolate astrocytes and microglia from the harvested tissue as per the manufacturer's guidelines. Briefly, the cortical tissue was rapidly submerged in a mixture of enzyme P and enzyme A provided by the Adult Brain Dissociation Kit to effect enzymatic dissociation. The submerged brains were subsequently cut into small pieces measuring roughly 1-2 mm³ using a pair of Iris scissors (Fine Science Tools, USA). The mixture of the cortex and enzyme was then subjected to further mechanical dissociation at 37 °C using the gentleMACS Octo Dissociator (Miltenyi Biotec, Germany). After mechanical dissociation, debris, and erythrocytes were removed from the cortex homogenate through sequential incubation-centrifugation cycles employing the debris removal solution and erythrocyte removal solution, respectively. The single-cell suspension was then incubated with microbeads (Miltenyi Biotec, Germany) that selectively bind to specific cell types – ACSA-2 microbeads coupled with FcR blocking reagent for astrocytes or CD11b microbeads for microglia, depending on the experimental aim. Subsequently, the corresponding target cells were isolated using MACS LS columns (Miltenyi Biotec, Germany) on QuadroMACS Separator (Miltenyi Biotec, Germany). Finally, the microglia and astrocytes that are positive for CD11b and ACSA-2 were employed for future experiments.

2.11 Primary microglia culture

The primary microglia were isolated and promptly suspended in a specialized culture medium designed for microglia, consisting of DMEM/F12 medium (Gibco, USA)

supplemented with 10% fetal bovine serum (FBS) (Gibco, USA), 10 ng/mL granulocyte-macrophage colony-stimulating factor (GM-CSF) (Gibco, USA), 10 ng/mL glial cell line-derived neurotrophic factor (GDNF) (Gibco, USA), and 15 mM 4-(2-Hydroxyethyl) piperazine-1-ethane sulfonic acid (HEPES) buffer (Thermo Scientific, USA). Additionally, to mitigate the risk of bacterial contamination, a penicillin-streptomycin mixture (Gibco, USA) was incorporated into the medium at a concentration of 100 U/mL for each component. The obtained primary microglia were seeded onto ibiTreat 8 Well μ -Slide (ibidi, Germany) at a concentration of approximately 1×10^5 cells per well. On the first day *in vitro* (DIV 1), the medium was replaced once. All microglia were cultured in a dedicated incubator (Thermo Scientific, USA) designed for primary cell culture and maintained at a temperature of 37 °C, a humidity level of 95%, and a 5% CO₂ supply.

2.12 pHrodo-conjugated synaptosome preparation

In this study, microglial phagocytic activity was measured using cortical synaptosomes²⁷² extracted from 3-4-month-old WT mice. The cortical tissue was extracted following cervical dislocation and homogenized in Syn-PER Reagent (Thermo Scientific, USA) using a set of 2 mL Dounce tissue grinders (Sigma Aldrich, USA) while maintained on ice. To obtain synaptosomes and separate them from cellular debris, the cortical homogenate underwent multiple rounds of centrifugation. The resultant synaptosome pellets were collected and resuspended in a mixture of Syn-PER Reagent and 1× Halt Protease and Phosphatase Inhibitor Cocktail (Thermo Scientific, USA) at a total protein concentration of 3 μ g/ μ L, and immediately stored at a temperature of -80 °C before the pHrodo conjugation.

For the pHrodo conjugation process, the cryogenically preserved synaptosomes were thawed and resuspended in 0.1 M NaHCO₃ (pH 8.5) at a total protein concentration of 10 μ g/ μ L. The resuspended synaptosomes were then incubated with dimethyl

sulfoxide (DMSO) (Sigma Aldrich, USA)-dissolved pHrodo Red, succinimidyl ester (Invitrogen, USA) at room temperature for a period of 2 h. Following conjugation, unbound pHrodo was eliminated through repeated centrifugation steps. The pHrodo-conjugated synaptosomes were subsequently collected, resuspended in PBS containing 5% DMSO, and stored at a temperature of -80 °C for use in subsequent experiments.

2.13 Microglia phagocytosis assay

Prior to the phagocytosis assay, primary microglia were subjected to a 4-day culture. On DIV 3, primary microglia from various experimental groups were pre-exposed for 24 hs to the culture medium containing WT brain ECF, *PDGF-h- α -syn* brain ECF, or DBI-neutralized *PDGF-h- α -syn* brain ECF at a total protein concentration of 1.5 mg/mL. In addition, a negative control group for the phagocytosis assay was established, where microglia were pre-exposed for 1 h to the culture medium containing 10 μ M cytochalasin D. Following pre-exposure, pHrodo-conjugated synaptosomes were applied to microglia for 1 h to evaluate their phagocytic activity. Post-incubation, microglia were delicately washed multiple times to eliminate any residual extracellular synaptosomes. Subsequent to the phagocytosis assay, microglia were fixed using eBioscience IC Fixation Buffer (Invitrogen, USA) and then blocked with eBioscience Permeabilization Buffer (Invitrogen, USA) at room temperature. After permeabilization, microglia were treated with a blocking buffer comprised of eBioscience Flow Cytometry Staining Buffer (Invitrogen, USA), which contained 10% normal donkey serum and 15% eBioscience Permeabilization Buffer, and then incubated with blocking-buffer-diluted primary antibodies against Iba1 and TSPO for 1 h. Subsequently, after being washed thrice with eBioscience Permeabilization Buffer, microglia were incubated with corresponding secondary antibodies. Finally, after secondary antibody incubation, microglia were washed once more and mounted using fluorescence mounting medium. The stained microglia were stored in darkness at 4 °C.

2.14 Confocal imaging

To perform *ex vivo* imaging of dendritic spines in mouse brains, stained sections were scanned using a Zeiss LSM780 confocal microscope (Zeiss, Germany) equipped with a Plan-Apochromat 40×/1.4 oil immersion differential interference contrast (DIC) M27 objective (Zeiss, Germany). All acquired images possessed a voxel size of 0.069 μm \times 0.069 μm \times 0.35 – 1 μm ($x \times y \times z$). To address the inherent image distortion during LSM780 image acquisition, all acquired images were subjected to deconvolution using AutoQuant X3 (Media Cybernetics, USA), which restored image fidelity and enhanced the quality of the acquired images.

2.15 Super-resolution confocal imaging

For super-resolution confocal imaging, mouse brain sections labeled with three to four channels were scanned on a Zeiss LSM900 confocal microscope equipped with Airyscan 2 (Zeiss, Germany) and a Plan-Apochromat 63×/1.4 oil immersion DIC M27. The LSM900 preserves image fidelity at the super-resolution level by employing oversampling with a voxel size of 0.035 μm \times 0.035 μm \times 0.14 μm ($x \times y \times z$) using the Airyscan 2 module. Following image acquisition, all images were digitally processed using the built-in "Airyscan processing" algorithm. All acquired images using LSM900 were scanned with the Airyscan 2 module and processed with Airyscan processing.

For mouse brain sections labeled with five channels and for cultured microglia, super-resolution confocal imaging was conducted on a Leica Stellaris 5 confocal microscope with Lightning (Leica, Germany) utilizing an HC PL APO CS2 63×/1.4 oil immersion objective (Leica, Germany). The Stellaris 5 maintained image fidelity through oversampling with a voxel size of 0.043 μm \times 0.043 μm \times 0.15 – 0.18 μm ($x \times y \times z$), and the dedicated "Lightning" deconvolution algorithm. All acquired images using Stellaris 5 were scanned and processed by the Lightning module.

For FFPE human brain samples, all stained sections were imaged on the Leica Stellaris 5 confocal microscope with Lightning utilizing an HC PL APO CS2 63×/1.3 glycerol immersion objective. The imaging protocols for human brain sections shared the same voxel size, scanning, and processing procedures as the protocols for mouse brain sections on Stellaris 5.

2.16 Cerebral protein extraction

To harvest mouse cerebral protein, mice were euthanized via cervical dislocation. The cerebrum was promptly excised from the brain tissue and submerged in Triton X-100 lysis buffer (Thermo Scientific, USA), which was supplemented with a 1× Protease/Phosphatase Inhibitor Cocktail (Cell Signaling Technology, USA). Subsequently, the cerebrum was meticulously homogenized while kept on ice, utilizing a set of 2 mL Dounce tissue grinders. The homogenized cerebrum was left on ice for 30 min and was subjected to centrifugation at 14000× g for an additional 30 min. Following the centrifugation, the supernatant, which contained the extracted protein, was procured and kept at a temperature of -80 °C for subsequent experimental procedures.

2.17 Co-immunoprecipitation

To assess the potential interaction between DBI and TSPO, Dynabeads Protein G Immunoprecipitation Kit (Thermo Scientific, USA) was employed. The protein samples from mouse brain homogenate was thawed in accordance with the manufacturer's instructions, and the total protein concentration was measured using the BCA assay and subsequently adjusted to 45 mg/mL using the same lysis buffer. Samples were then subjected to overnight incubation at 4 °C with goat-derived capture antibody targeting TSPO at a concentration of 10 µg/mL sample volume. Subsequently, the samples were mixed with Dynabeads Protein G at a concentration of 150 µl/mL sample volume and allowed to incubate at room temperature for 30 min. The Dynabeads-

antibody-TSPO complex was then retrieved via magnetization on a DynaMag-2 Magnet and subsequently eluted with the supplied Elution Buffer (Thermo Scientific, USA). Upon 2 min of incubation in the Elution Buffer, the anti-TSPO capture antibody and TSPO were dissociated from the Dynabeads. The Dynabeads were removed through the use of the DynaMag-2 Magnet, and the remaining supernatant was processed with Blue Loading Buffer (Cell Singling Technology, USA) containing 10% 1.25 M dithiothreitol (DTT) (Cell Singling Technology, USA) and stored at -20 °C until further immunoblotting detection.

2.18 Immunoblotting

To perform immunoblotting, cryogenically preserved protein samples from the mouse brain ECF and cerebrum were thawed, adjusted to comparable total protein concentration using the BCA assay, and mixed with Blue Loading Buffer containing 10% 1.25 M DTT as a reducing agent. The extensively blended samples were then loaded onto 4-20 % Mini-PROTEAN TGX precast protein gels (Bio-Rad, USA) for electrophoresis under a constant voltage of 110 V. Subsequently, the proteins were transferred from the gels onto Immobilon-P polyvinylidene fluoride (PVDF) membranes (Millipore, USA) using a constant current of 0.3 A for 90 min. After the transfer, the PVDF membranes were blocked utilizing tris-buffered saline (TBS) containing 5% skim milk (Millipore, USA) and Tween20 (PanReac AppliChem, USA) for 1 h at room temperature. After blocking, the PVDF membranes were incubated with various primary antibodies (Tab. 7) overnight at 4 °C, then with corresponding horseradish peroxidase (HRP)-conjugated secondary antibodies (Tab. 7) for 1 h at room temperature. Once the incubation with antibodies was completed, the PVDF membranes were developed utilizing enhanced chemiluminescence (ECL) Prime Western Blotting Detection Reagent (Amersham, UK) and scanned using a ChemiDoc MP imaging system (Bio-Rad, USA). The optical density (OD) of the protein bands of interest was determined using ImageLab software (Bio-Rad, USA). The determination

of the relative concentration of the protein of interest was achieved through a process of normalization. Specifically, the OD values of said protein were divided by the OD values of suitable housekeeping proteins that were also detected on the same membrane.

2.19 Enzyme-linked immunosorbent assay (ELISA)

To prepare protein samples for enzyme-linked immunosorbent assay (ELISA), the isolated astrocytes were lysed using a combination of alternating ultrasonication and centrifugation cycles, repeated four times. The brain ECF was thawed and thoroughly pipetted. Subsequently, the total protein concentration of all samples was determined using the BCA assay before ELISA was conducted. The concentration of DBI in each sample was measured using the LSBio ELISA Kit (Lifespan Biosciences, USA) in accordance with the manufacturer's instructions. Samples were successively incubated with primary, HRP-conjugated secondary antibodies and 3,3',5,5'-tetramethylbenzidine (TMB) substrate for color development. Following the color development, the OD value at a wavelength of 450 ± 2 nm was measured and recorded for each well using the Infinite M200 Pro NanoQuant microplate reader (Tecan, Switzerland). To calculate the DBI concentration in the tested samples, the ELISA-detected absolute DBI concentration of each sample was normalized to its total protein concentration, which had been previously measured by the BCA assay.

2.20 Stereotactic injection

To perform stereotactic injections of adeno-associated virus (AAV) in the brains of mice, a sedation regimen consisting of midazolam, medetomidine, and fentanyl (MMF) at concentrations of 5 mg/kg body weight, 0.5 mg/kg body weight, and 0.05 mg/kg body weight, respectively, was administered intraperitoneally. Following the attainment of adequate sedation, the mouse was mounted onto a stereotactic frame with its cranium exposed. Subsequently, the stereotactic injection of AAV, containing mouse small

hairpin RNA responsible for silencing the expression of the DBI (m-DBI-shRNA) (Vector Biolabs, USA) (Tab. 8), or AAV containing control scrambled RNA (scrmb-shRNA) (Vector Biolabs, USA) (Tab. 8), was infused bilaterally into the neocortex of each hemisphere at five distinct sites, within depth between 100-300 μm . Mice intended for *in vivo* imaging experiments received implantation of a cranial window after the injection procedure (refer to the "Cranial window implantation" section). Once the surgical procedure was completed, the mouse was revived using an MMF antidote comprised of atipamezole, naloxone, and flumazenil (ANF) at 2.5 mg/kg, 1.2 mg/kg, and 0.5 mg/kg body weight, respectively. Concurrently, carprofen at 4 mg/kg body weight, and metamizole at 200 mg/kg body weight were administered subcutaneously to mitigate the potential inflammation and pain. After the surgical intervention, the mice were individually housed and allowed to recuperate for a duration of 4 weeks before subsequent experiments.

Table 8 AAVs used in this study.

Construct	Source	Titer
AAV5-mCherry-U6-m-DBI-shRNA	Vector Biolabs	3.9×10^{12} genome copies (GC)/mL
AAV5-mCherry-U6-scrmb-shRNA	Vector Biolabs	1.2×10^{13} GC/mL

2.21 Cranial window implantation

The procedure for cranial window implantation was performed in compliance with previous studies^{77,273}, albeit with certain modifications. Prior to the procedure, the mouse was subjected to sedation via intraperitoneal injection of MMF and subsequently fixed onto a stereotactic frame with the cranium exposed. In order to establish optical access to the cortical region of interest, a circular section of parietal bone measuring 4 mm in diameter was meticulously excised from the mouse skull using a dental drill. Once the cortex was visible, the dura mater was cautiously detached with the use of fine-tipped forceps. Following the removal of the dura mater,

the craniotomy was sealed with a 4 mm diameter circular coverslip, which was affixed to the skull using dental acrylic by its margin to ensure a hermetic seal. In addition, a customized z-shaped metal bar was attached to the frontal-nasal bone of the mouse skull, serving as a clamp to attach the mouse to the framework mounted on the stage of the *in vivo* two-photon microscope. Once the coverslip and the metal bar were securely attached to the skull, the mouse was revived with an ANF injection, accompanied by subcutaneous administration of carprofen and metamizole to alleviate inflammation and pain post-surgery. Subsequently, the mouse was housed individually for a period of four weeks to ensure complete recovery prior to *in vivo* two-photon imaging.

2.22 *In vivo* imaging of dendritic spines

In order to conduct *in vivo* imaging of dendritic spines, all mice participating in the experiments were subjected to isoflurane inhalation-induced sedation prior to imaging. To obtain images of apical dendritic tufts emanating from eGFP-labeled pyramidal neurons positioned in layer V of the somatosensory cortex, the anesthetized mouse was securely positioned onto a customized framework, which was then mounted onto the imaging stage of the microscope. Images of dendritic spines were obtained using a Plan-Apochromat 20x/1.0 DIC M27 water immersion objective (Zeiss, Germany) on a customized LSM 880 two-photon microscope (Zeiss, Germany). The eGFP signal was excited by utilizing a two-photon laser set to a wavelength of 880 nm. During acquisition, all dendritic spine images were acquired as "z-stacks". To track the fate of specific sets of dendritic spines over time, the distinctive superficial blood vascular pattern on the cortex surrounding each imaged site was photographed during the first imaging session and subsequently utilized as a reference for revisiting the same site in subsequent sessions (Fig. 7).

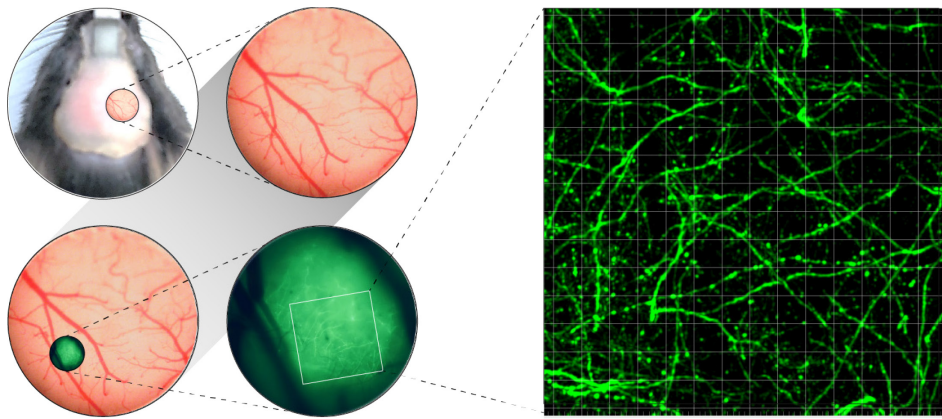


Figure 7 Long-term *in vivo* two-photon imaging of dendritic spines.

Long-term *in vivo* two-photon imaging is conducted by repeatedly imaging the same set of dendrites. To revisit the same imaging location during the imaging process, the distinctive patterns of blood vessels on the brain surface are used as references.

For each mouse, 2-3 sites within the region of interest were selected randomly, and 10-15 dendrites were imaged at each site. To maintain the stability of vital parameters of the mouse during and after imaging, all imaging sessions were limited to less than 1 h.

2.23 Image analysis for astrocytes and microglia

In order to analyze images related to glia, all acquired images were transformed into a suitable format for Imaris 9.7.1 (Andor Technology, UK) processing. Following this conversion process, all images underwent further analysis utilizing Imaris.

To explore the distribution of astrocytic DBI both inside and outside its originating cells (astrocyte origins), three-dimensional (3D) reconstructions of astrocytes were generated using the "Surface" module of Imaris. The DBI signal was reconstructed using the "Spot" module based on the mean diameter of the DBI⁺ signal measured under the "Slice" view. Following reconstruction, DBI⁺ puncta were classified as either "inside puncta" or "outside puncta" based on their spatial proximity to the astrocyte origin. The quantity of astrocyte-contained DBI was calculated as a ratio of the count

of "inside" DBI⁺ puncta to the volume of their respective astrocyte origins. The distribution of astrocyte-released DBI was determined by counting the number of "outside" DBI⁺ puncta within a specified distance from the surface of their respective astrocyte origins. To assess the number of astrocytes in particular regions, 3D reconstruction of astrocytic somata was carried out using the "Spot" module, based on the average diameter of astrocytic somata that was predetermined under the "Slice" view. Upon the completion of the reconstruction, the "Spot" module automatically generated the number of spots in each region (Fig. 8).

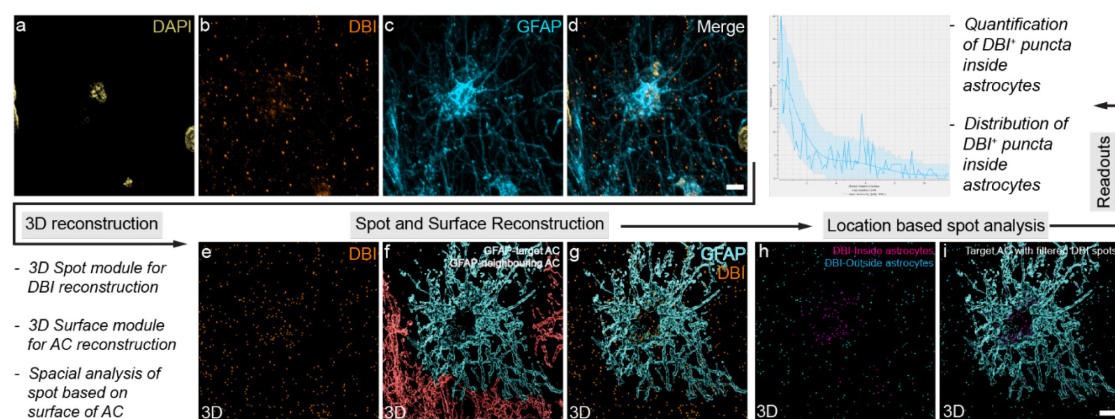


Figure 8 3D reconstruction and analysis for distribution of astrocytic DBI.

For microglial TSPO and PLA signal, microglia were reconstructed in 3D using the "Surface" module. The TSPO⁺ volume and the PLA⁺ volume were also reconstructed in 3D using the same method. The TSPO⁺/PLA⁺ volume was then classified based on their relative location to the microglia, and only microglia-containing TSPO/PLA were included in further analysis. The relative quantities of TSPO and PLA were calculated as the ratio of the TSPO⁺ volume or the PLA⁺ volume to the microglial volume. To analyze the morphology of microglia, 3D reconstruction of microglia was carried out using the "Filament" module. The number of process lengths, segments, process volume, branch points, and terminal points of each microglia was generated automatically by the module. To investigate the number of microglia in specific regions, microglial somata were reconstructed in 3D utilizing the "Spot" module based on the

average diameter of the microglia somata. The number of spots in each region was automatically generated by the module. To examine microglial engulfment of synaptic materials, microglia and microglial lysosomes (CD68) were reconstructed using the “Surface” module. The stained synaptic materials (PSD95) were reconstructed utilizing the “Spot” module based on the average diameter of PSD95⁺ puncta. The relative number of PSD95⁺ puncta that were engulfed by microglia was calculated by normalizing the number of PSD95⁺ puncta found within microglia-containing CD68 to the volume of these microglia (Fig. 9).

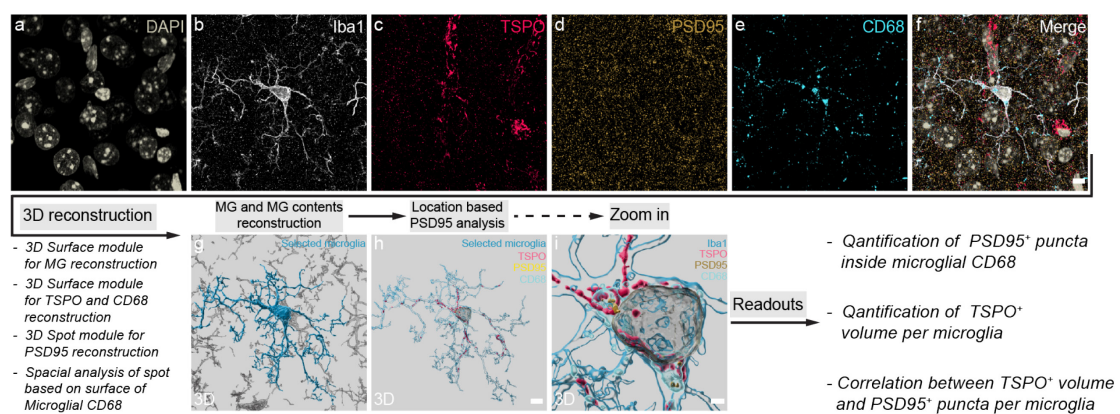


Figure 9 3D reconstruction and analysis for microglial TSPO and their engulfment of synaptic materials.

In the case of cultured microglia, the synaptic materials (pHrodo-conjugated synaptosomes) were reconstructed utilizing the "surface" module due to their distinct morphology inside microglia. The microglial phagocytosis of synaptosomes was calculated as the ratio of the volume of synaptosomes contained within the microglia to the volume of these microglia.

2.24 Image analysis for dendritic spines

For image analysis, the acquired *ex vivo* dendritic spine images underwent conversion to a format suitable for processing through Imaris 9.7.1. After the conversion, 3D objects mimicking the dendrite (and dendritic spines on it) of interest were reconstructed in each image utilizing the “Filament” module of Imaris. According to the predetermined

morphological categories⁷⁷, all reconstructed dendritic spines were automatically classified into three types: "mushroom," "thin," and "stubby." A "mushroom" spine was identified by the presence of maximum width (head) to minimum width (neck) ratio ≥ 1.1 , with a head width greater than $0.2 \mu\text{m}$ and neck width greater than $0 \mu\text{m}$. A "thin" spine was classified as having a maximum width (head) to minimum width (neck) ratio ≥ 1.1 , with a head width less than $0.2 \mu\text{m}$ or a spine length to mean neck width ratio ≥ 3 . Lastly, a "stubby" spine was designated with a length-to-mean neck width ratio < 3 and a maximum width (head) to minimum width (neck) ratio < 1.1 . The density of the dendritic spines of each dendrite was computed by dividing the spine count by the dendrite's length (per μm).

For images of dendritic spines obtained *in vivo*, the relative movement of the animal to the microscopic objective results in inherent z-dimension distortion during the *in vivo* imaging. Hence, to prevent potential inaccuracies attributable to the distortion, solely spines that laterally sprout from the dendrites (spines primarily on x-y dimension) in the acquired images and exhibit a high signal-to-noise ratio were included in subsequent analyses. Dendritic spines along the dendrite were manually identified and labeled as newly gained, lost, or stable ones, using the following criteria: dendritic spines that emerged or disappeared during consecutive imaging sessions were categorized as "gained" or "lost" spines, respectively; dendritic spines that remained in the same relative locations ($< 0.5 \mu\text{m}$ difference along the dendrite) along the dendrite for at least two consecutive imaging sessions were classified as "stable". The dendritic spine density of each time point was calculated using the same method as in the *ex vivo* images. For the micrographs presented in the figures, the maximum intensity projection of each image was displayed, which was initially processed with Imaris 9.7.1 (Andor Technology, UK) to remove distracting neighboring dendritic elements. Subsequently, AutoQuant X3 (Media Cybernetics, USA) was employed to deconvolve the maximum intensity projection images and to enhance the image quality. Finally,

contrast and brightness adjustments were performed to ensure that the images could be viewed with greater clarity.

2.25 Image analysis for neurons and blood vessels

Prior to conducting the analysis, all images underwent conversion to a format suitable for use with Imaris 9.7.1 (Andor Technology, UK).

In order to assess the volume of TSPO present in both neuronal and vascular structures, a 3D reconstruction of neurons and vascular (endothelial cells) was performed using the “Surface” module. The TSPO⁺ volume was similarly reconstructed in 3D using the same method. Subsequently, the TSPO volume was classified based on its relative location with respect to the originating cells, with only cell-containing TSPO being subjected to further analysis. The relative abundance of TSPO was determined through the calculation of the ratio between the TSPO⁺ volume and the volume of the cell in which TSPO was contained. To investigate the number of neurons present in specific regions, the neuronal somata were reconstructed in 3D utilizing the “Spot” module, based on the average diameter of the neuronal somata determined under the “Slice” view. The resulting number of spots in each region was then automatically generated by the module.

2.26 Key resources

Key reagents, consumables, and kits used in this study are listed in Tab.9.

Table 9 Key resources used in this study.

Category	Item	Source	Identifier
Chemicals, peptides, and recombinant proteins	GDNF from Mouse	Sigma	Cat# SRP3200
	GM-CSF Recombinant Mouse Protein	Thermo Scientific	Cat# PMC2016
	Mouse Acyl-CoA-Binding Protein (DBI) Protein	Abbexa	Cat# abx066329

Category	Item	Source	Identifier
	PLX5622	Plexxikon	https://www.plexxikon.com/
	Protease and Phosphatase Inhibitor Single-Use Cocktail, EDTA-Free (100X)	Thermo Scientific	Cat# 78443
	Triton X-100 Lysis Buffer	Alfa Aesar	Cat# J62289
Critical commercial assays	Adult Brain Dissociation Kit	Miltenyi Biotec	Cat# 130-107-677
	Anti-ACSA-2 MicroBead Kit	Miltenyi Biotec	Cat# 130-097-678
	CD11b (Microglia) MicroBeads	Miltenyi Biotec	Cat# 130-093-634
	Duolink <i>In Situ</i> Detection Reagents Orange	Sigma	Cat# DUO92007
	Duolink <i>In Situ</i> Detection Reagents Red	Sigma	Cat# DUO92008
	Duolink <i>In Situ</i> Probemaker MINUS	Sigma	Cat# DUO92010
	Duolink <i>In Situ</i> Probemaker PLUS	Sigma	Cat# DUO92009
	Duolink <i>In Situ</i> Wash Buffers, Fluorescence	Sigma	Cat# DUO82049
	Mouse DBI / ACBD1 ELISA Kit	LifeSpan BioSciences	Cat# LS-F9925
	pHrodo Red, Succinimidyl Ester (pHrodo Red, SE) Kit	Thermo Scientific	Cat# P36600
	Protein G Immunoprecipitation Kit	Invitrogen	Cat# 10007D
	Syn-PER Synaptic Protein Extraction Reagent	Thermo Scientific	Cat# 87793
Cell culture	DMEM/F12	Gibco	Cat# 31330-038
	Fetal Bovine Serum	Gibco	Cat# A316041
	Penicillin-Streptomycin (10000 U/ml)	Gibco	Cat# 15140122
	HEPES	Thermo Scientific	Cat# J16924.AE

Category	Item	Source	Identifier
	DPBS, calcium, magnesium, glucose, pyruvate	Gibco	Cat# 14287080
	PBS/BSA buffer	Miltenyi Biotec	Cat# 130091376
	AstroMACS Separation Buffer	Miltenyi Biotec	Cat# 130117336
	Cytochalasin D	Enzo Life Sciences	Cat# BML-T109-0001

2.27 Key software tools

The software used for data acquisition and analysis in this study is listed in Tab.10.

Table 10 Key software used in this study.

Software	Source	Identifier
AutoQuant	Media Cybernetics	http://www.mediacy.com/autoquantx3
Image Lab 6.0.1	Bio-Rad	http://www.bio-rad.com/en-us/product/image-lab-software
Imaris 9.7.1	Andor Technology	https://imaris.oxinst.com
Leica LAS X 4.4.0.24861	Leica	https://www.leica-microsystems.com/products/microscope-software/p/leica-las-x-ls/
MATLAB	MathWorks	https://www.mathworks.com/products/matlab
Prism 9	GraphPad	https://www.graphpad.com/scientific-software/prism/
ZEN Imaging Software	Zeiss	https://www.zeiss.com/microscopy/int/products/microscope-software/zen

2.28 Statistics

GraphPad Prism 9 software (GraphPad Software, USA) was utilized to conduct statistical analyses. For comparing consecutive *in vivo* two-photon data, a repeated two-way analysis of variance (ANOVA) was conducted, followed by Bonferroni's multiple comparisons test. Violations of the sphericity assumption were accounted for using the Geisser-Greenhouse correction for all repeated measures of ANOVA. Data

between two distinct groups were analyzed using a two-tailed Student's *t*-test, while multiple comparisons were made using one-way ANOVA followed by either Bonferroni's or Dunnett's posthoc test. The χ^2 test was utilized to compare the proportion of differently shaped spines. Mann-Whitney and Kolmogorov-Smirnov tests were conducted to compare spine head volume data based on mean ranks and cumulative distribution, respectively. To ensure clarity and fairness in comparison, the data was presented in various forms. For floating bars, the line within the box represents the mean value, with the upper and lower boundaries representing the maximum and minimum values, respectively. For violin plots, median values and interquartile ranges were plotted. All other data were presented as mean \pm standard error of the mean (S.E.M.), unless otherwise specified. Statistical significance was defined as a *p*-value less than 0.05.

3. Results

3.1 Elevated astrocytic DBI and microglial TSPO in LBD

3.1.1 Astrocytic DBI expression and release increase in LBD

In order to emulate LBD pathology in rodents, I employed the *PDGF-h- α -syn* mouse model, which expresses WT human α -synuclein in neurons of various brain regions, including the substantia nigra, hippocampus, and cerebral cortex²⁶⁹. The expression of human α -synuclein in the brains of these mice has been consistently detectable since three months of age and exhibits a progressive increase over time²⁷⁴. Along with the elevated α -synuclein expression, prior research has indicated a significant decrease in dendritic spine density within the cortical region of *PDGF-h- α -syn* mice commencing from 3 months of age and subsequently worsening⁴². Therefore, to examine the glial factors that affect dendritic spines during the early stages of LBD, 3-4-month-old *PDGF-h- α -syn* mice were included in the current investigation.

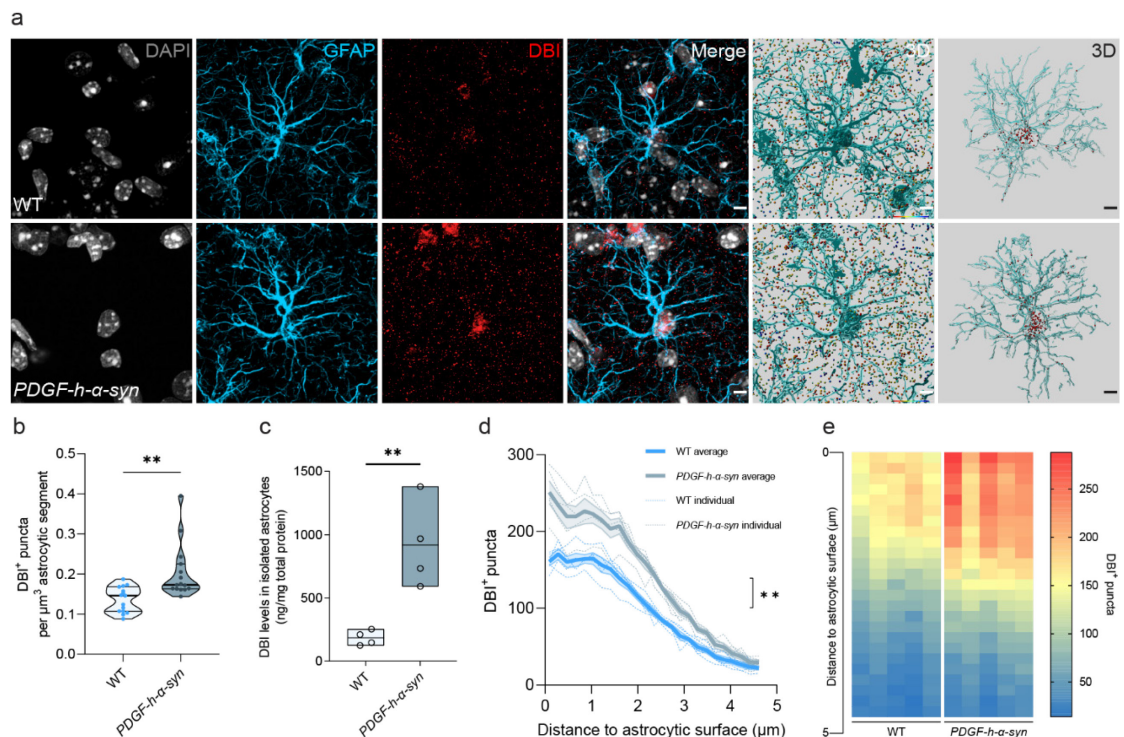


Figure 10 Elevated astrocytic DBI production and release in *PDGF-h- α -syn* mice.

a, Representative confocal micrographs and 3D reconstruction of cortical glial fibrillary acidic protein (GFAP)⁺ astrocytes and DBI in 3.5-month-old *PDGF-h- α -syn* and WT mice. **b**, Quantification of DBI⁺ puncta in the GFAP⁺ astrocytic segment. **c**, Quantitation of astrocytic DBI by ELISA. **d & e**, Distribution (**d**, in curve and **e**, in heat map, each lane represents one mouse) of DBI⁺ puncta radiating from astrocytes, showing the release pattern of astrocytic DBI. $n = 15$ astrocytes from 5 animals per group (**a**, **b**); $n = 4$ animals, in duplicates (**c**); $n = 5$ animals per group (**d**, **e**). For floating bars, the line within the box represents the mean. Two-sided Mann-Whitney test (**b**: $U = 32.50$, $p = 0.0005$); Two-sided unpaired Student's t test (**c**: $t_{(6)} = 4.193$, $p = 0.0057$); Kolmogorov-Smirnov test (**d**: $D = 0.4400$, $p = 0.0158$). $**p < 0.01$. Scale bars: **a** = 5 μm .

Initially, I conducted an extensive profiling of astrocytic DBI expression in cortical regions of 3-4-month-old *PDGF-h- α -syn* mice via immunostaining. To ensure a robust reconstruction and precise localization of the immunolabeled DBI signal, high-quality images were acquired using a Zeiss LSM900 with Ariyscan 2 super-resolution confocal microscope. Following the 3D reconstruction and spatial analysis of the DBI signal in the acquired images, a larger number of DBI⁺ puncta within cortical astrocytes of *PDGF-h- α -syn* mice were observed in comparison to age- and sex-matched WT controls, indicating a higher level of DBI expression within these astrocytes (Fig. 10a&b). Supporting this finding, using ELISA, I also detected an elevated ratio of DBI to total protein in isolated cortical astrocytes from *PDGF-h- α -syn* mice, as compared to their WT counterparts (Fig. 10c).

In parallel with analyzing the DBI contained within astrocytes, I conducted a detailed reconstruction and assessment of the distribution of DBI released from astrocytes. Through the process of categorizing DBI⁺ puncta based on their proximity to adjacent astrocytes, I discovered that the cortical astrocytes from *PDGF-h- α -syn* mice exhibited a greater concentration of DBI⁺ puncta in close proximity to them, as compared to the astrocytes from the WT mice. This proximity-dependent distribution, as depicted in Fig. 10d-e, indicates a more robust pattern of DBI release from the *PDGF-h- α -syn* cortical astrocytes.

In order to corroborate this finding, I obtained extracellular fluid (ECF) from the brains of both *PDGF-h- α -syn* mice and WT controls, and proceeded to assess the concentration of DBI therein. In accordance with my previous observations using immunostaining techniques, the ECF derived from the brains of *PDGF-h- α -syn* mice evinced significantly higher DBI concentrations than that of their WT counterparts, as determined by both immunoblotting and ELISA (Fig. 11a-c).

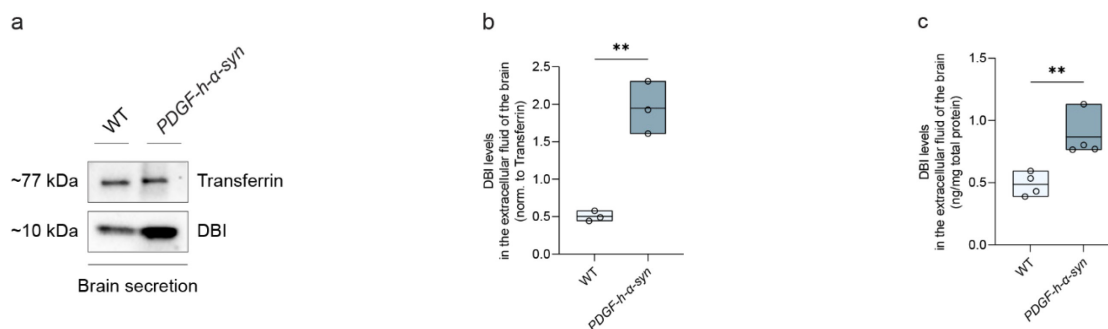


Figure 11 Elevated levels of DBI produced in astrocytes and released in the brains of *PDGF-h- α -syn* mice.

a & b, Representative immunoblots (**a**) and quantitation of DBI levels (**b**) in the brain extracellular fluid in 3.5-month-old *PDGF-h- α -syn* and WT mice. **c**, Quantitation of DBI in brain ECF of WT and *PDGF-h- α -syn* mice by ELISA. $n = 3$ animals per group, samples were immunoblotted in triplicate (**a**, **b**); $n = 4$ animals per group (**c**). For floating bars, the line within the box represents the mean. Two-sided unpaired Student's t test (**b**: $t_{(4)} = 7.002$, $p = 0.0022$; **c**: $t_{(6)} = 3.800$, $p = 0.0090$). ** $p < 0.01$.

3.1.2 Microglial TSPO enhances in LBD

Subsequent to the confirmation of elevated astrocytic DBI release, a comprehensive array was undertaken to evaluate the CNS DBI receptor, TSPO¹⁶⁸. Prior research has established the presence of TSPO in a range of CNS cells, including neurons, endothelial cells, astrocytes, and microglia^{77,142}. Furthermore, recent investigations have demonstrated that TSPO derived from different cell types exhibit distinct and sometimes conflicting responses to CNS challenges, such as neuroinflammation and neurodegeneration^{142,275}. To ascertain the reaction of TSPO derived from different CNS cell types to the LBD, TSPO and its primary cellular sources were immunolabeled in the brains of both *PDGF-h- α -syn* and WT mice.

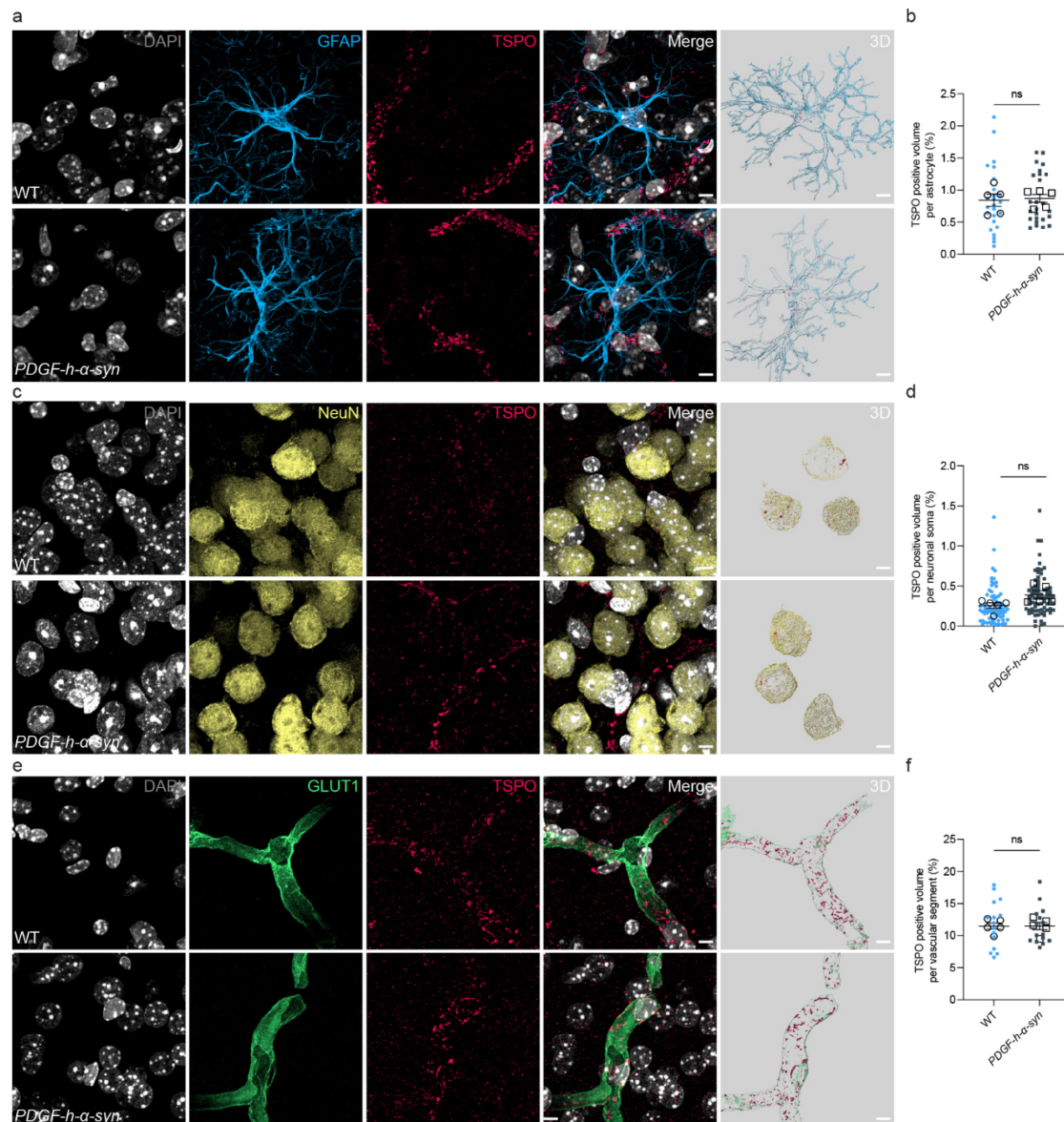


Figure 12 TSPO expression in different cell types of *PDGF-h-α-syn* and WT mice.

a, Representative confocal micrographs, 3D reconstruction of TSPO inside cortical GFAP⁺ astrocytes in 3.5-month-old *PDGF-h-α-syn* and age-matched WT controls. **b**, Quantification of TSPO⁺ volume per astrocyte. **c**, Representative confocal micrographs, 3D reconstruction of TSPO inside cortical NeuN⁺ neuronal soma in 3.5-month-old *PDGF-h-α-syn* and age-matched WT controls. **d**, Quantification of TSPO⁺ volume per neuronal soma. **e**, Representative confocal micrographs, 3D reconstruction of TSPO inside cortical GLUT1⁺ vascular endothelium in 3.5-month-old *PDGF-h-α-syn* and age-matched WT controls. **f**, Quantification of TSPO⁺ volume per vascular segment. $n = 5$ animals per group (**a-f**). Data are presented as mean \pm s.e.m. Two-sided unpaired Student's *t* test (**b**: $t_{(8)} = 0.2414$, $p = 0.8153$; **d**: $t_{(8)} = 2.169$, $p = 0.0619$; **f**: $t_{(8)} = 0.01788$, $p = 0.9862$). ** $p < 0.01$. n.s. - no significant difference. Scale bars = 5 μ m.

To quantify the relative abundance of TSPO in different major CNS cell types, namely neurons, endothelial cells, astrocytes, and microglia, I utilized super-resolution confocal imaging coupled with 3D reconstruction. The results, as presented in Fig. 12,

demonstrate that TSPO was detectable in all four cell types in both *PDGF-h- α -syn* and WT mice. However, only microglia in *PDGF-h- α -syn* mice exhibited a significantly higher TSPO signal than their WT counterparts (Fig. 13). This finding suggests that the TSPO-mediated cellular changes in the mouse model of LBD are specific to microglia.

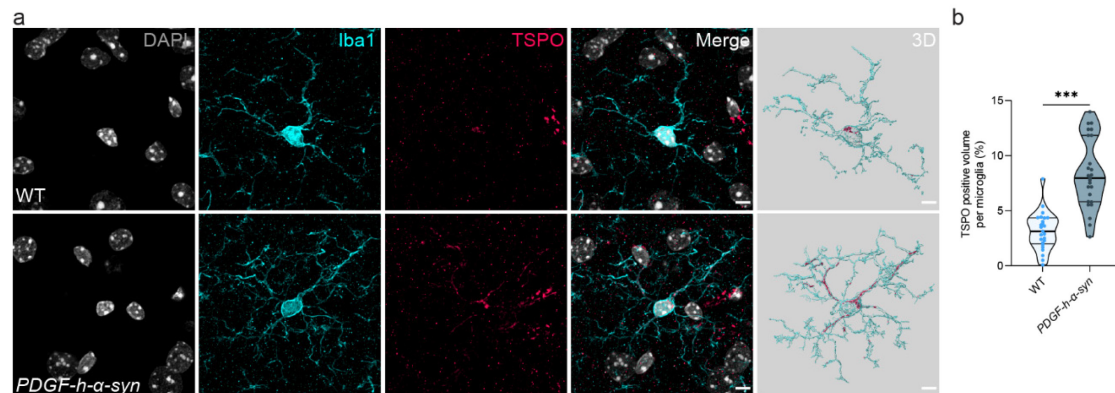


Figure 13 Elevated TSPO expression in microglia of *PDGF-h- α -syn* mice.

a, Representative confocal micrographs, 3D reconstruction of TSPO inside in Iba1⁺ microglia in 3.5-month-old *PDGF-h- α -syn* and age-matched WT controls. **b**, Quantification of TSPO⁺ volume per vascular segment. $n = 5$ animals per group (**a-b**). Data are presented as mean \pm s.e.m. For violin plots, median values and interquartile ranges are plotted. Two-sided unpaired Student's t test (**b**: $t_{(48)} = 7.250$, $p < 0.0001$). ** $p < 0.01$. n.s. - no significant difference. Scale bars = 5 μ m.

3.1.3 DBI-TSPO bindings elevate in LBD

Within the CNS, the DBI and TSPO serve as a set of endogenous ligands receptors. Given the significant elevation of both astrocytic DBI and microglial TSPO observed in the brains of *PDGF-h- α -syn* mice, it is reasonable to inquire whether the increase in these proteins is two isolated occurrences or an interconnected phenomenon. To explore this matter, I conducted an investigation into the bindings between DBI and TSPO and their potential alterations during LBD.

To begin, I conducted a co-immunoprecipitation assay to verify the interactions between DBI and TSPO. Using an anti-TSPO antibody, I captured TSPO from the brain homogenates of both *PDGF-h- α -syn* and WT mice, and successfully detected the

presence of DBI alongside captured TSPO in these samples. This finding demonstrates that DBI naturally attaches to TSPO (Fig. 14a-c).

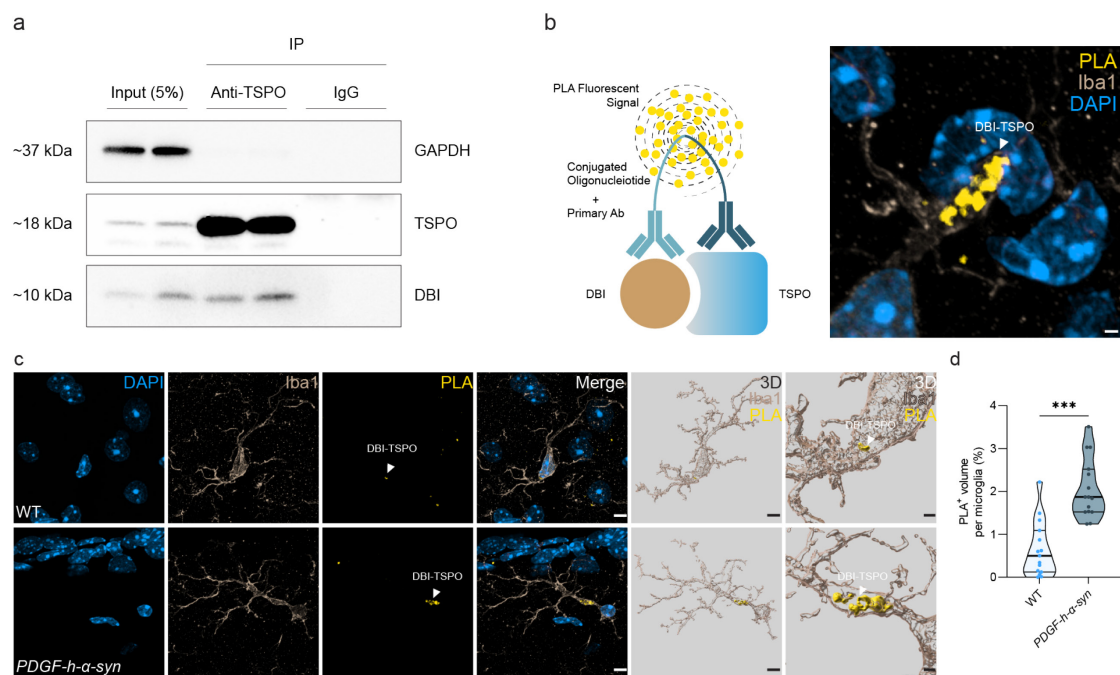


Figure 14 Elevation of DBI-TSPO bindings in *PDGF-h-α-syn* mice.

a, Co-immunoprecipitation assay showing the interaction between DBI and TSPO, protein extract (input) was immunoprecipitated using the anti-TSPO antibody, and IgG was used as the negative control. Protein-protein interactions were detected using anti-TSPO and anti-DBI antibodies. **b**, Schematic representation of the PLA with representative PLA fluorescence images. **c**, Representative images and 3D reconstructions of PLA⁺ volume in microglia from 3.5-month-old *PDGF-h-α-syn* and WT mice, PLA⁺ volume represents ligation of DBI and TSPO. **d**, Quantification of PLA⁺ volume in the Iba1⁺ microglia. $n = 4$ animals per group (**a**); $n = 15$ microglia from 5 animals per group (**c**, **d**). For violin plots, median values and interquartile ranges are plotted. Two-sided Mann-Whitney test ($k: U = 14, p < 0.0001$). *** $p < 0.001$. Scale bars: **b** = 1 μm ; **c** = 5 (lane 1-5 from left), 1 (lane 6) μm .

To evaluate the interplay between astrocytic DBI and microglial TSPO in specific cell types and locations, I incorporated regular immunostaining with the protein ligation assay (PLA). The PLA utilizes customized oligonucleotide-conjugated antibodies to label adjacent proteins. If the spatial proximity between the two proteins is less than 40 nm, the oligonucleotides can act as templates for further hybridization and circularization, ultimately resulting in the formation of circular DNA molecules. These circular DNA molecules can then be amplified via rolling circle amplification and detected by hybridizing with fluorescently labeled oligonucleotides that are

complementary to the circular DNA molecules²⁷¹, as illustrated in Fig. 14. In line with my observations regarding astrocytic DBI and microglial TSPO, the PLA signal that signifies interactions between DBI and TSPO was found to be significantly increased in cortical microglia of *PDGF-h- α -syn* mice, as compared to WT controls (Fig. 14c&d). This suggests that the binding between astrocytic DBI and microglial TSPO is elevated in *PDGF-h- α -syn* mice.

Collectively, these results indicate that in the LBD mouse model, there is an increased amount of DBI produced and released from astrocytes, which subsequently forms excessive bonds with microglial TSPO.

3.2 Enhanced microglial synaptic engulfment via DBI-TSPO signaling

3.2.1 Morphological alterations of microglia in LBD

As per a recent research my colleagues and I conducted, in WT mice, the activation of TSPO through the use of synthetic ligands resulted in microglial morphological changes and their heightened phagocytic activity towards synaptic materials⁷⁷. In *PDGF-h- α -syn* mice, although microglial TSPO was activated through the utilization of endogenous ligands, it is worthwhile to ponder whether, in LBD, comparable TSPO-mediated alterations also take place in microglia.

To furnish evidentiary support for the aforementioned supposition, I have assimilated the TSPO knockout (*Tspo*^{-/-}) mouse model, wherein the expression of TSPO has been genetically depleted²⁷⁰. Moreover, I have conducted crossbreeding between the *Tspo*^{-/-} mice and the *PDGF-h- α -syn* mice. Outcomes obtained from these *Tspo*^{-/-} strains serve to corroborate the microglial alterations observed in WT and *PDGF-h- α -syn* mice, demonstrating the dependency of the observed changes on the TSPO.

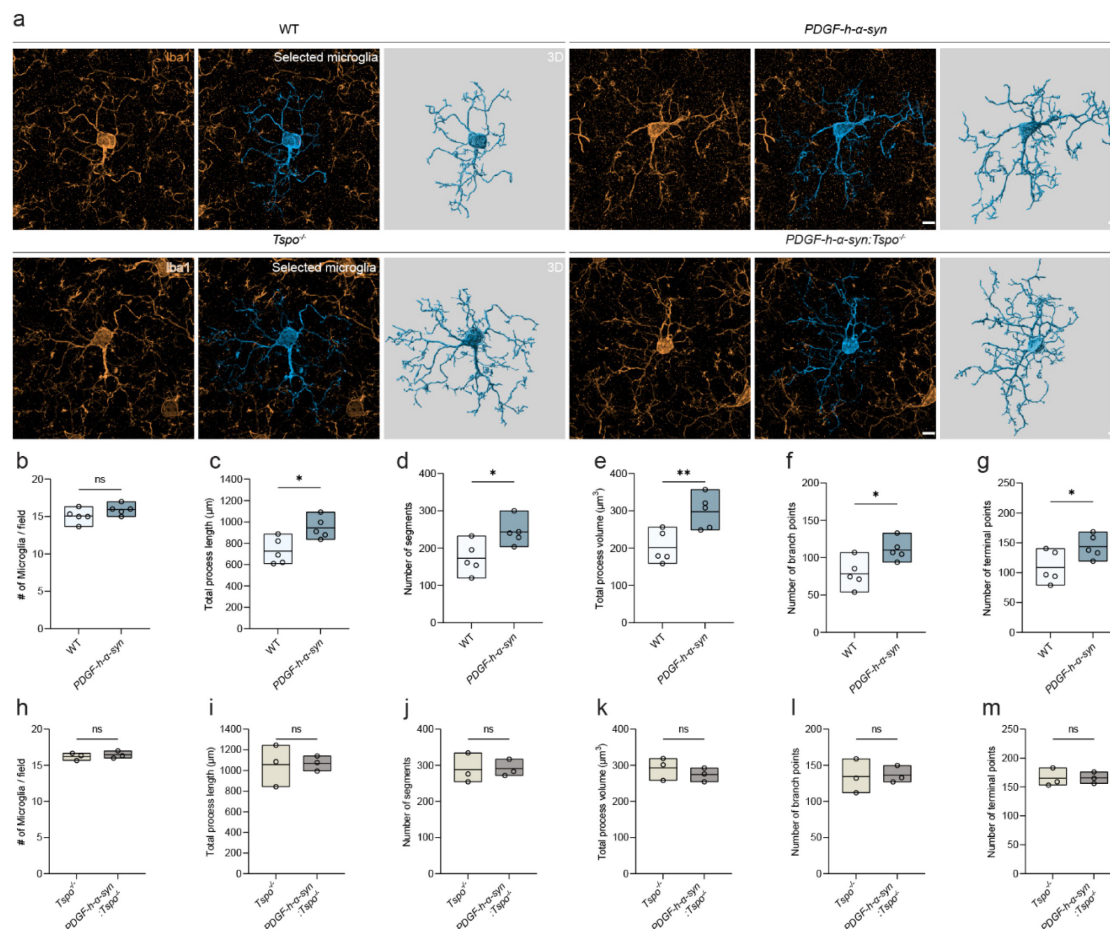


Figure 15 Altered microglial morphology in *PDGF-h-α-syn* mice.

a, Representative super-resolution confocal micrographs and 3D reconstruction of cortical Iba1⁺ microglia in 3.5-month-old WT, *PDGF-h-α-syn*, *Tspo*^{-/-}, and *PDGF-h-α-syn:Tsapo*^{-/-} mice. **b-m**, Imaris-based semi-automatic quantification of microglia morphometry. $n = 5$ animals (**b-g**); $n = 3$ animals (**h-m**). For floating bars, the line within the box represents the mean. Two-sided unpaired Student's *t* test (**b**: $t_{(8)} = 1.619$, $p = 0.1441$; **c**: $t_{(8)} = 3.035$, $p = 0.0162$; **d**: $t_{(8)} = 2.845$, $p = 0.0216$; **e**: $t_{(8)} = 3.404$, $p = 0.0093$; **f**: $t_{(8)} = 2.942$, $p = 0.0187$; **g**: $t_{(8)} = 2.327$, $p = 0.0484$; **h**: $t_{(4)} = 0.5340$, $p = 0.6216$; **i**: $t_{(4)} = 0.1022$, $p = 0.9235$; **j**: $t_{(4)} = 0.08728$, $p = 0.9346$; **k**: $t_{(4)} = 0.8661$, $p = 0.4353$; **l**: $t_{(4)} = 0.1400$, $p = 0.8954$; **m**: $t_{(4)} = 0.05555$, $p = 0.9584$). * $p < 0.05$, ** $p < 0.01$. n.s. - no significant difference. Scale bars: **a** = 5 μm .

As illustrated above, microglia in *PDGF-h-α-syn* mice exhibited a significant increase in volume and arborized processes, with elevated counts of branch and terminal points when compared to those in WT microglia (Fig. 15a, c-g). Despite these changes, there was no indication of microgliosis in the *PDGF-h-α-syn* mice (Fig. 15b&h). On the other hand, microglia in *Tspo*^{-/-} and *PDGF-h-α-syn:Tsapo*^{-/-} mice generally exhibited higher volume and more complex structures. However, no discernible morphological alterations were detected between these two groups (Fig. 15a, i-m), indicating that the

morphological changes observed in *PDGF-h- α -syn* mice were contingent on the presence of TSPO.

3.2.2 Elevated TSPO-dependent microglial synaptic engulfment

Having established the TSPO-dependent morphological alterations in microglia morphology following LBD, the next question is whether the phagocytic activity of microglia towards synaptic materials changes with their altered morphology.

To investigate this, I employed a multichannel immunostaining approach. In addition to microglia (Iba1) and TSPO, PSD95, an essential scaffolding protein for the construction and maintenance of postsynaptic density⁵⁹, was immunolabelled as a marker of dendritic spines. Moreover, the CD68 marker, which represents the microglial lysosome responsible for engulfing extracellular materials during phagocytosis²⁷⁶, was also subjected to labeling. In concert, the tally of PSD95⁺ puncta detected within the CD68⁺ lysosome denotes the microglial uptake of dendritic spines.

Whitney test (**b**: $U = 45$, $p < 0.0001$; **c**: $U = 43$, $p < 0.0001$); Two-sided unpaired Student's t test (**e**: $t_{(28)} = 0.2669$, $p = 0.7915$). * $p < 0.05$, ** $p < 0.01$. n.s. - no significant difference. Scale bars: **a** = 1 μm .

By employing the 3D reconstruction and analysis, I have ascertained that when normalized to cell volume, microglia in *PDGF-h- α -syn* mice exhibited a marked increase in the number of engulfed PSD95⁺ puncta, relative to their WT counterparts. This result suggests that the phagocytic activity of microglia was more pronounced in the *PDGF-h- α -syn* mice (Fig. 16a-c). Furthermore, I conducted quantification of TSPO volume in these microglia and investigated its correlation with the aforementioned engulfed PSD95⁺ puncta (Fig. 16d). My findings reveal a robust positive correlation between these two variables. This observation implies that the heightened level of TSPO in *PDGF-h- α -syn* mice positively impacts the phagocytosis of synaptic materials by microglia.

In contrast, in line with my observations of microglial morphology, it is evident that upon TSPO depletion, the LBD pathology in *PDGF-h- α -syn* mice failed to augment the microglial phagocytic activity towards synaptic materials (Fig. 16a&e). This finding serves to substantiate further that the alterations of microglial phagocytosis in *PDGF-h- α -syn* mice occurred in a TSPO-dependent manner.

3.2.3 Elevated microglial synaptic engulfment via DBI-TSPO signaling

In order to ascertain whether the TSPO-mediated increase in microglial synaptic engulfment in *PDGF-h- α -syn* mice was attributable to astrocytic DBI, I combined the multichannel immunostaining approach with the PLA of DBI-TSPO binding. Notably, in addition to an elevated engulfment of PSD⁺ puncta in microglia of *PDGF-h- α -syn* mice compared to their WT counterparts (Fig. 17a&b), these microglia exhibited a significantly greater volume of DBI-TSPO PLA signal (Fig. 17c). Moreover, I found a strong correlation between microglial synaptic engulfment and the DBI-TSPO PLA signal in microglia (Fig. 17d), suggesting that the augmented phagocytic activity of

microglia towards synaptic materials can be ascribed to the excessively activated DBI-TSPO signaling in *PDGF-h- α -syn* mice.

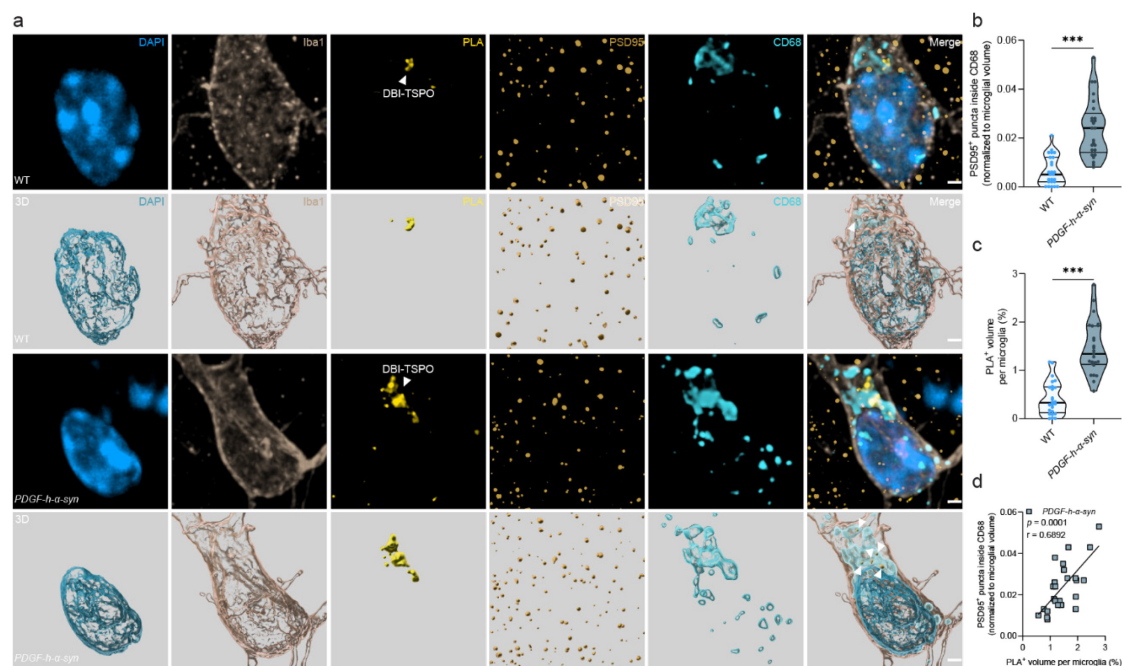


Figure 17 Astrocytic DBI confers microglial synaptic engulfment via TSPO.

a, Representative super-resolution confocal micrographs and 3D reconstruction of PLA (ligation of TSPO and DBI) volume, and CD68⁺ lysosomes with engulfed PSD95 puncta in microglia of *PDGF-h- α -syn* and WT mice. **b**, Normalized number of PSD95 in CD68⁺ microglial lysosomes. **c**, Quantification of PLA⁺ volume per microglia. **d**, Correlation between microglial PLA and engulfed PSD95 levels. Pearson's correlation $r = 0.6892$, significance (two-tailed) $p = 0.0001$. $n = 5$ animals, 25 microglia per group (**a-d**). For violin plots, median values and interquartile ranges are plotted. One-way ANOVA followed by Dunnett's multiple comparisons test (**b**: $F_{(4, 70)} = 30.43$, $p < 0.0001$; **c**: $F_{(4, 40)} = 14.35$, $p <$

3.2.4 DBI-induced alteration of TSPO-mediated phagocytosis of primary microglia

To further validate the foregoing results, primary-cultured microglia from the cerebral cortex of 3-4-month-old WT and *Tspo*^{-/-} mice were isolated, and their phagocytic activity toward synaptic materials was assessed *in vitro*. To emulate the *in vivo* environment and furnish primary microglia with naturally-released DBI, brain ECF was collected from both WT and *PDGF-h- α -syn* mice and utilized as DBI sources. Additionally, immunoblotting was performed to determine whether the brain ECF exclusively contained DBI that was naturally released from intact brain cells, wherein stathmin served as a marker for cytosolic protein. As illustrated in Fig. 18a, the absence of

stathmin in brain ECF indicated that the majority of brain cells were well-preserved during brain ECF collection.

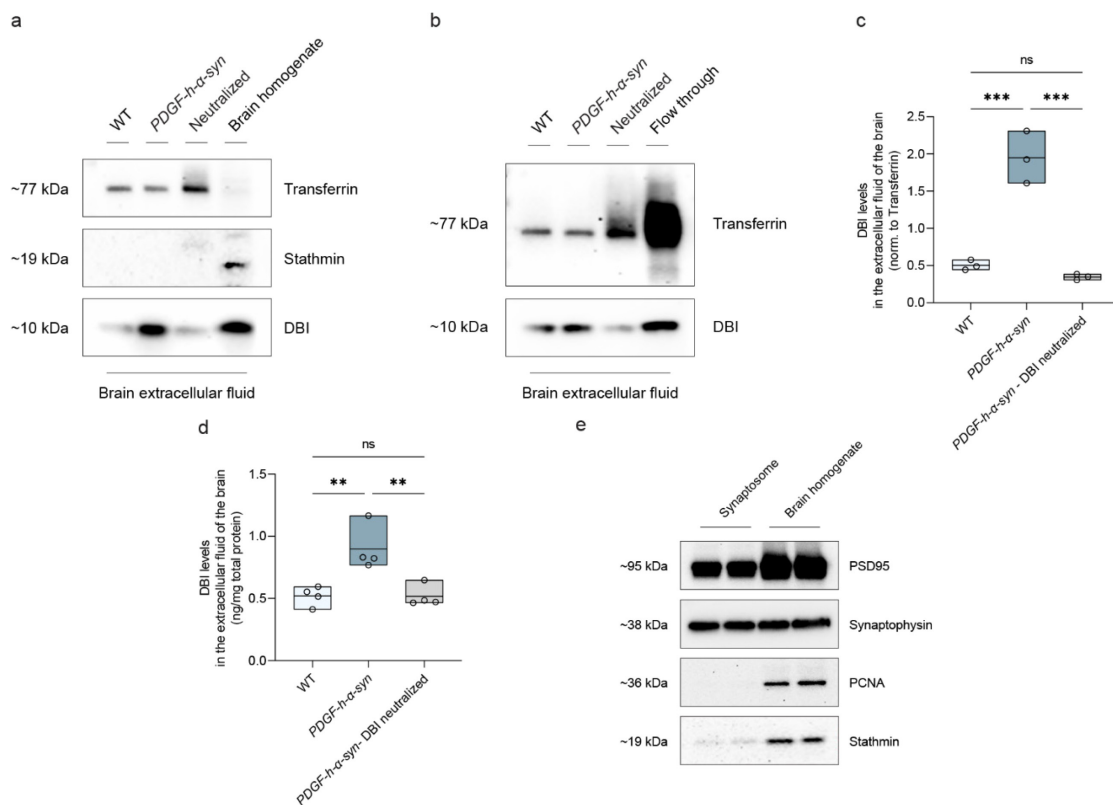


Figure 18 DBI neutralization in brain ECF and synaptosome purification.

a, Representative immunoblotting of DBI in brain extracellular fluid (ECF) of WT and *PDGF-h-α-syn* mice, *PDGF-h-α-syn* brain ECF with DBI neutralization and WT brain homogenate, coupled with immunoblotting of Stathmin (cytoplasmic protein, marker for brain cell lysate) and Transferrin (housekeeping protein for brain extracellular fluid). **b**, Representative immunoblotting of DBI and Transferrin in brain ECF of WT and *PDGF-h-α-syn* mice, *PDGF-h-α-syn* brain ECF with DBI neutralization and flow through of *PDGF-h-α-syn* brain ECF with DBI neutralization. **c**, Quantification of DBI in brain ECF of WT and *PDGF-h-α-syn* mice, *PDGF-h-α-syn* brain ECF with DBI neutralization, normalized to Transferrin. $n = 3$ animals per group, samples were immunoblotted in triplicate (**a-c**). **d**, Quantitation of DBI in brain ECF of WT and *PDGF-h-α-syn* mice, *PDGF-h-α-syn* brain ECF with DBI neutralization by ELISA. **e**, Characterization of extracted synaptosomes used in DBI-related microglial phagocytosis assay, the purity of synaptosomes was verified using pre- and postsynaptic protein (Synaptophysin, PSD95), cytosolic protein (Stathmin) and nuclear protein (PCNA). Please note that compared to brain homogenate, synaptosomes contain a high concentration of pre- and postsynaptic proteins, a trace amount of cytosolic protein, and no nuclear protein. $n = 4$ animals per group (**c, d**). For violin plots, median values and interquartile ranges are plotted. Two-sided unpaired Student's *t* test (**e**: $t_{(28)} = 0.2669$, $p = 0.7915$); Two-sided Mann-Whitney test (**b**: $U = 45$, $p < 0.0001$; **c**: $U = 43$, $p < 0.0001$). For floating bars, the line within the box represents the mean. One-way ANOVA followed by Bonferroni's multiple comparisons test (**c**: $F_{(2, 6)} = 54.26$, $p = 0.0001$; **d**: $F_{(2, 9)} = 12.32$, $p = 0.0027$). ** $p < 0.01$, *** $p < 0.001$. n.s. - no significant difference. Scale bars: **a** = 1 μm .

In tandem with WT and *PDGF-h- α -syn* brain ECF, I also introduced recombinant mouse DBI into primary-cultured microglia at a concentration of 0.1 $\mu\text{g}/\text{mL}$. The purpose of this incorporation was to assess the singular influence of DBI on microglial. As a point of comparison, particular samples of *PDGF-h- α -syn* brain ECF underwent immunodepletion (neutralization) of DBI to more sophisticatedly control the effects of DBI on microglial functions (Fig. 18b-d).

To evaluate the phagocytic activity of microglia towards synaptic materials *in vitro*, cortical tissue was extracted from 3-4-month-old WT mice to obtain synaptosomes²⁷² – specialized subcellular fractions comprised of resealed postsynaptic entities conjoined with the presynaptic component of synapses (Fig. 18e). In order to visualize and authenticate microglial synaptic engulfment, all synaptosomes were conjugated with pHrodo, as this pH-sensitive fluorophore emits red fluorescence upon uptake into microglial lysosomes, which is a low pH environment¹¹⁰.

Before co-incubation with pHrodo-conjugated synaptosomes, all primary-cultured microglia underwent a 24-h preexposure to various experimental conditions. These conditions included exposure to WT brain ECF, *PDGF-h- α -syn* brain ECF, 0.1 $\mu\text{g}/\text{mL}$ mouse recombinant DBI, and DBI-neutralized *PDGF-h- α -syn* brain ECF. Following this preexposure, primary-cultured microglia were co-incubated with pHrodo-conjugated synaptosomes for a period of 2 h (Fig. 19a).

In addition to the aforementioned groups, certain primary-cultured microglia underwent a 2-h preexposure to 10 μM cytochalasin D, which is an inhibitor of actin polymerization and known to act as a phagocytic inhibitor (Fig. 19a). This treatment served as a negative control for the experimental conditions, and as a result, only a negligible amount of engulfed synaptosomes were observed inside these microglia.

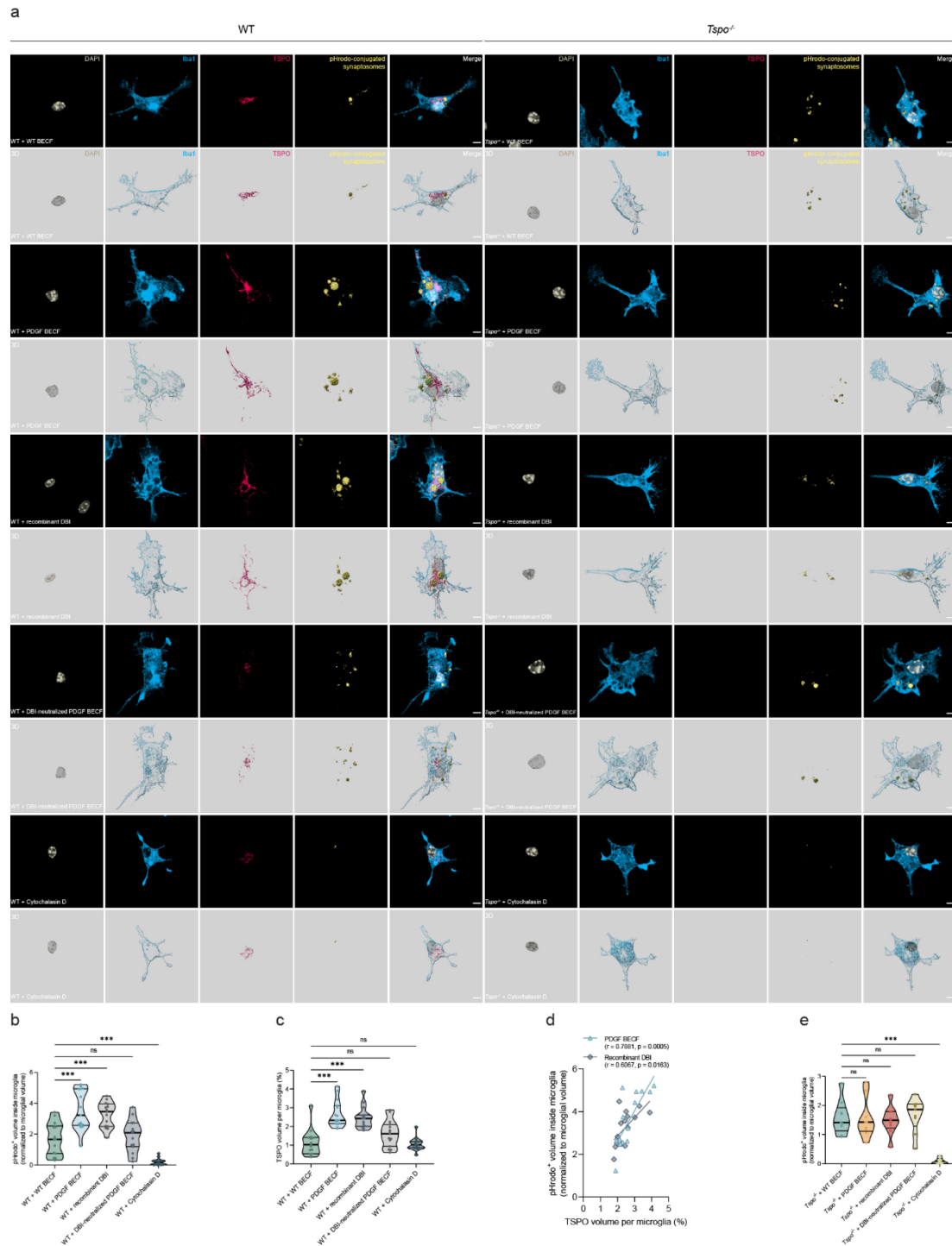


Figure 19 TSPO-dependent synaptosome uptake by microglia.

a, Representative super-resolution confocal micrographs and 3D reconstruction of *in vitro* microglial phagocytosis assay with microglia (Iba1 staining, blue), TSPO (red) and pHrodo conjugated synaptosomes (yellow). **b & c**, Quantification of WT microglial engulfed synaptosomes and expressed TSPO within 2-h incubation after the *in vitro* engulfment assay with brain ECF from WT, *PDGF-h-a-syn* mice, 0.1 μ g/mL mouse recombinant DBI and DBI-neutralized brain ECF from *PDGF-h-a-syn* mice treatment for 24 h; cytochalasin D was used as a negative control. **d**, Correlation between WT microglial TSPO and engulfed synaptosome levels. Pearson's correlation r (PDGF brain ECF) = 0.7881, significance (two-tailed) p = 0.0005; r (Recombinant DBI) = 0.6067, significance (two-tailed) p = 0.0163. **b & c**,

Quantification of *Tspo*^{-/-} microglial engulfed synaptosomes within 2-h incubation after the *in vitro* engulfment assay with brain ECF from WT, *PDGF-h-α-syn* mice, 0.1 μg/mL mouse recombinant DBI and DBI-neutralized brain ECF from *PDGF-h-α-syn* mice treatment for 24 h; cytochalasin D was used as a negative control. n = 15 microglia per WT group (**b-d**); n = 9 microglia per *Tspo*^{-/-} group (**e**). For violin plots, median values and interquartile ranges are plotted. One-way ANOVA followed by Dunnett's multiple comparisons test (**b**: $F_{(2, 24)} = 16.58, p < 0.0001$). ** $p < 0.01$, *** $p < 0.001$. Scale bars = 5 μm.

Through 3D reconstruction and analysis, my investigations have revealed that relative to microglia preexposed to WT brain ECF, microglia preexposed to *PDGF-h-α-syn* brain ECF and 0.1 μg/mL mouse recombinant DBI exhibited augmented engulfment of synaptosomes, as well as heightened expressions of TSPO (Fig. 19b&c). Consistent with prior research, I observed a positive correlation between TSPO expression and microglial synaptosome uptake (Fig. 19d). Furthermore, I found that neutralization of DBI mitigated the enhanced microglial synaptosome engulfment induced by the naïve *PDGF-h-α-syn* brain ECF (Fig. 19b&c), indicating the DBI-dependent nature of TSPO-mediated microglial synaptic engulfment.

Remarkably, my results demonstrated that only microglia obtained from WT mice, but not from *Tspo*^{-/-} mice, exhibited elevated uptake of synaptosomes after being preexposed to the *PDGF-h-α-syn* brain ECF and 0.1 μg/mL mouse recombinant DBI, both of which contain a relatively high concentration of DBI (Fig. 19a&e). This finding emphasizes the necessity of TSPO for the DBI-induced enhancement of microglial engulfment of synaptosomes.

Collectively, these lines of evidence suggest that the excessive release of DBI in the mouse model of LBD triggers morphological changes in microglia and leads to amplified microglial phagocytosis of synaptic materials via the overactivated DBI-TSPO signaling pathway.

3.3 DBI-TSPO suppression alleviates dendritic spine pathology in LBD

3.3.1 Dendritic spine impairment in LBD

An expanding corpus of evidence has established dendritic spines as the structural underpinnings of cognition and its modulations under diverse conditions^{45,46,83}. In line with these, prior investigations have described dendritic spine damage in the context of LBD-associated cognitive decline in both human and animal subjects^{42,44,84-88,277}.

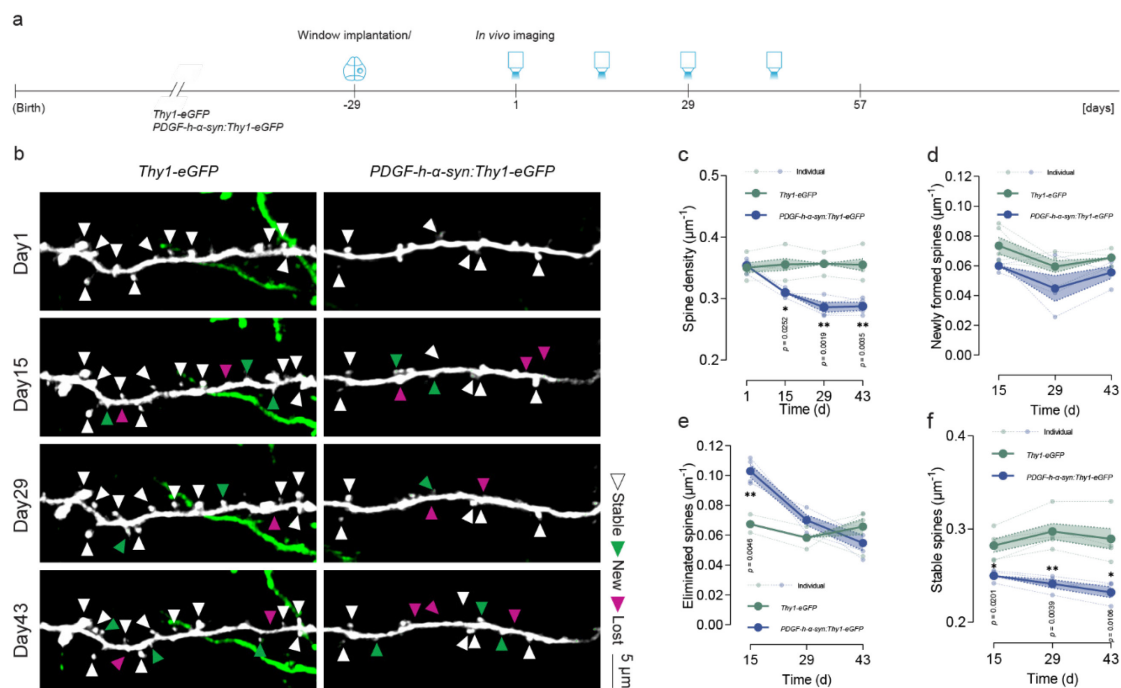


Figure 20 Structural plasticity of dendritic spines is impaired in *PDGF-h-α-syn* mice.

a, Experimental design. **b**, Representative *in vivo* two-photon micrographs of apical dendritic tufts. **c-f**, Dendritic spine density (**c**), densities of gained (**d**), lost (**e**), and stable (**f**) spines in *PDGF-h-α-syn* and WT mice. $n = 5$ animals, ~990 spines from 44 dendrites in *Thy1-eGFP* group; 4 animals, ~755 spines from 33 dendrites in *PDGF-h-α-syn:Thy1-eGFP* group (**b-f**). Dot plots represent mean \pm s.e.m. Repeated measures ANOVA with Geisser-Greenhouse correction followed by two-way repeated measures ANOVA with Geisser-Greenhouse correction followed by Bonferroni's multiple comparisons test (**c**: $F_{\text{interaction: genotype} \times \text{time}} (3, 21) = 49.80, p < 0.0001$; **d**: $F_{\text{interaction: genotype} \times \text{time}} (2, 14) = 0.1409, p = 0.8698$; **e**: $F_{\text{interaction: genotype} \times \text{time}} (2, 14) = 18.91, p = 0.0001$; **f**: $F_{\text{interaction: genotype} \times \text{time}} (2, 14) = 10.97, p = 0.0014$) * $p < 0.05$, ** $p < 0.01$. Scale bars: **b** = 5 μm .

To trace the longitudinal trajectory of dendritic spines and investigate their plasticity in *PDGF-h-α-syn* mice *in vivo*, I conducted crossbreeding between *PDGF-h-α-syn* mice and *Thy1-eGFP* mice. This crossbreeding permits visualization of dendritic spines

through the insertion of a transgene encoding eGFP in a subset of neurons⁷¹, which can be excited via laser stimulation at 488 nm (confocal) or 880 nm (two-photon).

In order to investigate the synaptic impairment occurring in cortical regions during the early stages of LBD, I installed a cranial window on the mouse cranium via replacement of a circular section of parietal bone with a coverslip of corresponding dimensions. This surgical intervention was performed when the mouse was approximately 2-month-old, and following a convalescence period of one month, the animal was then deemed suitable for longitudinal *in vivo* two-photon imaging.

From approximately 3 months of age, I monitored the fate of cortical dendritic spines in mice for over 50 days. While cortical dendritic spines exhibit sustained structural stability under healthy conditions, *PDGF-h- α -syn:Thy1-eGFP* mice displayed a markedly lower proportion of stable cortical dendritic spines compared to *Thy1-eGFP* mice (Fig. 20). This was accompanied by a significantly elevated rate of spine elimination and a progressive decrease in overall dendritic spine density.

3.3.2 *TSPO deficiency alleviates dendritic spine impairment in LBD*

Building upon the demonstration of dendritic spine impairment in *PDGF-h- α -syn:Thy1-eGFP* mice, and taking into account prior findings, I again employed longitudinal *in vivo* two-photon imaging to investigate the role of TSPO in the context of LBD with respect to dendritic spine impairment.

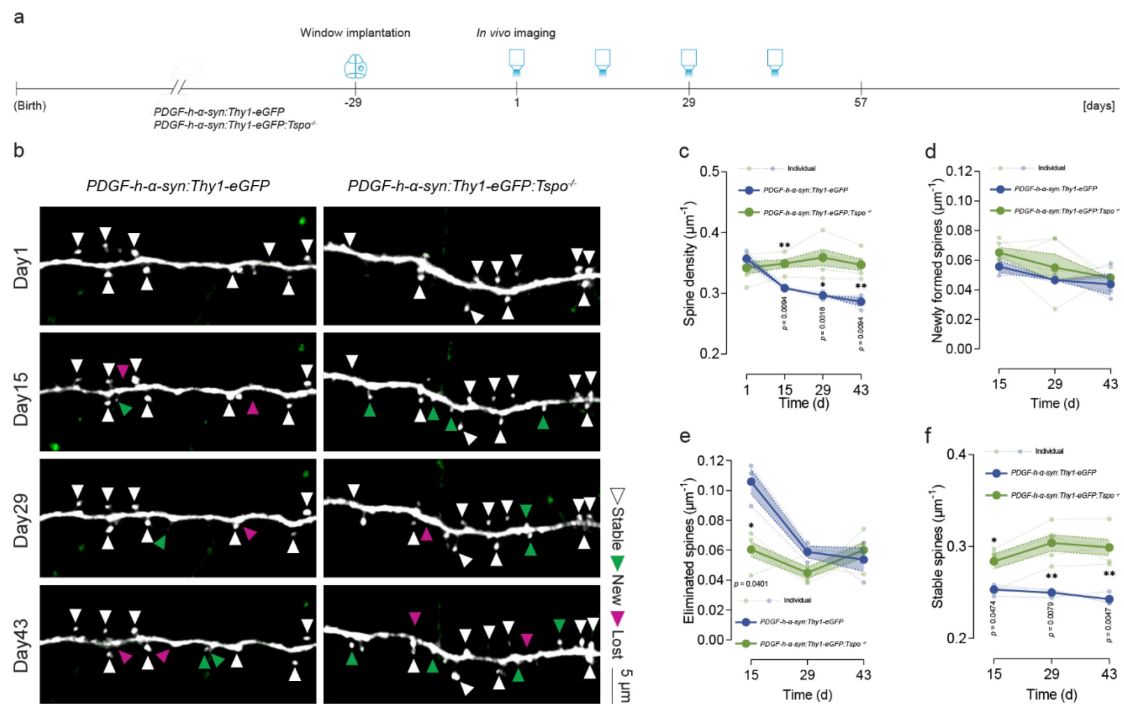


Figure 21 The impairment of dendritic spine structural plasticity is TSPO-dependent in *PDGF-h-α-syn* mice.

a, Experimental design. **b**, Representative *in vivo* two-photon micrographs of apical dendritic tufts. **c-f**, Dendritic spine density (**b**), densities of gained (**c**), lost (**d**), and stable (**e**) spines in *PDGF-h-α-syn:Tspo^{-/-}* and *PDGF-h-α-syn* mice. $n = 3$ animals, ~499 spines from 25 dendrites in *PDGF-h-α-syn:Thy1-eGFP* group; 5 animals, ~805 spines from 38 dendrites in *PDGF-h-α-syn:Thy1-eGFP:Tspo^{-/-}* group (**b-f**). Dot plots represent mean \pm s.e.m. Repeated measures ANOVA with Geisser-Greenhouse correction followed by two-way repeated measures ANOVA with Geisser-Greenhouse correction followed by Bonferroni's multiple comparisons test (**c**: $F_{\text{interaction: genotype} \times \text{time}}(3, 18) = 26.06$, $p < 0.0001$; **d**: $F_{\text{interaction: genotype} \times \text{time}}(2, 12) = 0.09305$, $p = 0.9118$; **e**: $F_{\text{interaction: genotype} \times \text{time}}(2, 12) = 8.326$, $p = 0.0054$; **f**: $F_{\text{interaction: genotype} \times \text{time}}(2, 12) = 4.300$, $p = 0.0391$). * $p < 0.05$, ** $p < 0.01$. Scale bars: **b** = 5 μm .

To this end, I crossbred *Thy1-eGFP* and *PDGF-h-α-syn:Tspo^{-/-}* strains to visualize cortical dendritic spines. By conducting long-term tracing of dendritic spines over the same time range as in the previous section, I discovered that compared to *PDGF-h-α-syn:Thy1-eGFP* mice, the impairment of dendritic spines was significantly reduced in the *PDGF-h-α-syn:Tspo^{-/-}:Thy1-eGFP* mice. Specifically, in comparison to *PDGF-h-α-syn:Thy1-eGFP* mice, the *PDGF-h-α-syn:Tspo^{-/-}:Thy1-eGFP* mice exhibited a much higher proportion of stable spines and a much lower elimination rate of total spines, resulting in a relatively sustained dendritic spine density that was similar to that observed in the *Thy1-eGFP* mice (Fig. 21).

3.3.3 Microglia depletion attenuates dendritic spine impairment in LBD

In order to elucidate the contribution of microglia to dendritic spine impairment in the LBD context, I conducted a pharmacological intervention to deplete microglia from the CNS of *PDGF-h- α -syn:Thy1-eGFP* mice using the compound PLX5622. This compound is a remarkably potent inhibitor of the colony-stimulating factor 1 receptor (CSF1R), which is an indispensable factor in the development and sustenance of tissue macrophages, including microglia that reside within the CNS²⁷⁸.

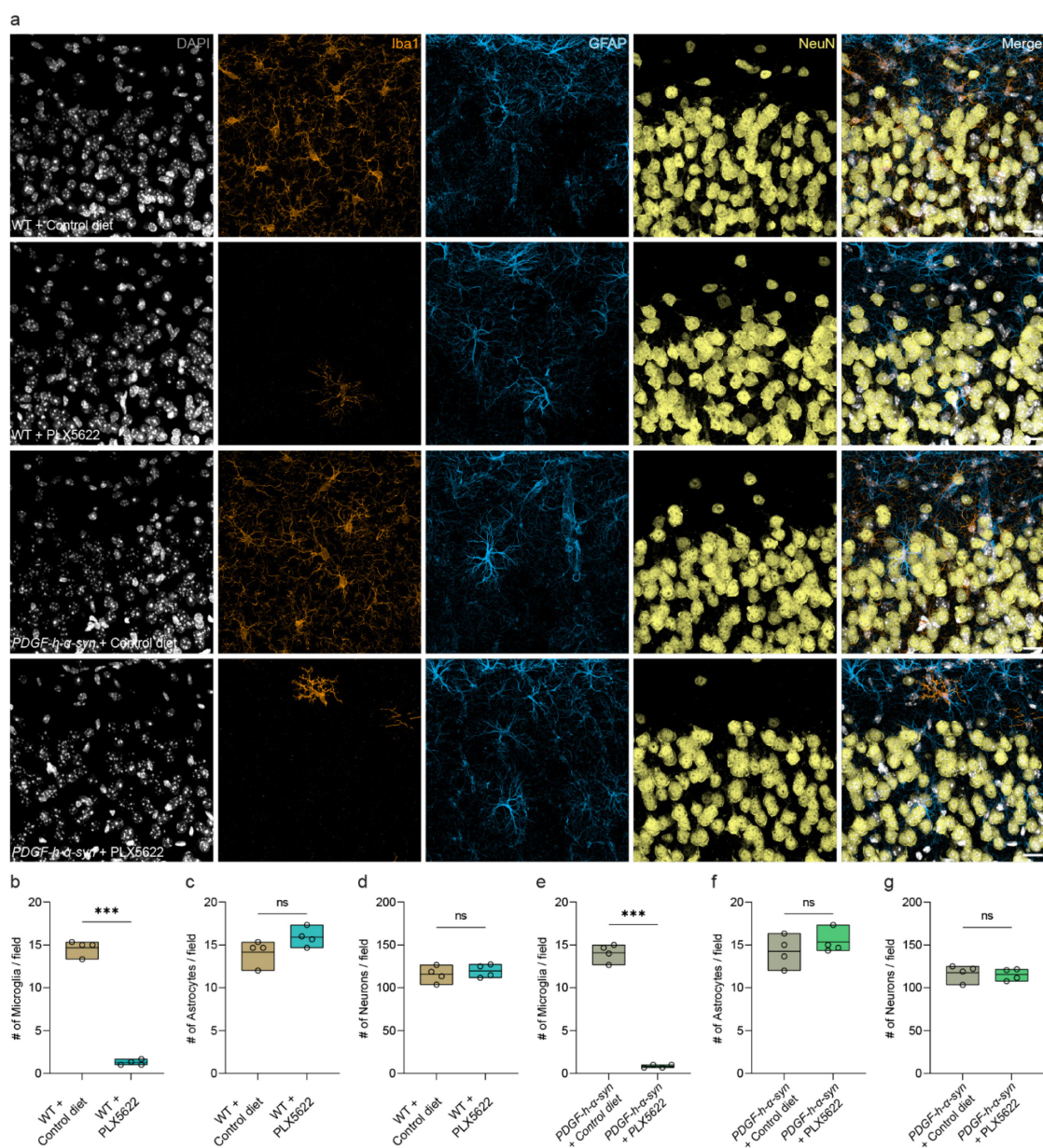


Figure 22 Long-term microglia elimination does not affect astrocytes or neurons in *PDGF-h- α -syn* and WT mice.

a, Representative confocal micrographs show that WT or *PDGF-h- α -syn* mice treated with the control diet or PLX5622 to fully eliminate microglia. **b & e**, Quantification of Iba1⁺ cells in the cortex, as shown, was performed via Imaris spot counts, revealing robust decreases in microglial numbers in WT (**b**) or *PDGF-h- α -syn* (**e**) mice treated with PLX5622. **c & f**, Quantification of GFAP⁺ cells encompassing the cortex of 3-4 months-old WT (**c**) or *PDGF-h- α -syn* (**f**) mice fed with six-week PLX5622 or control diet as shown were performed via Imaris spot counts, revealing no changes. **d & g**, Relative numbers of NeuN⁺ cells per field in the cortex of 3-4 months-old WT (**d**) or *PDGF-h- α -syn* (**g**) mice fed with six-week PLX5622 or control diet as shown were performed via Imaris spot counts, revealing no changes. n= 4 animals per group (**a-g**). For floating bars, the line within the box represents the mean. Two-sided unpaired Student's *t* test (**b**: $t_{(6)} = 28.02$, $p < 0.0001$; **c**: $t_{(6)} = 1.899$, $p = 0.1063$; **d**: $t_{(6)} = 0.6627$, $p = 0.5322$; **e**: $t_{(6)} = 25.25$, $p < 0.0001$; **f**: $t_{(6)} = 0.9423$, $p = 0.3824$; **g**: $t_{(6)} = 0.3367$, $p = 0.7478$). *** $p < 0.001$. n.s. - no significant difference. Scale bars = 10 μ m.

Prior to initiating longitudinal two-photon imaging of dendritic spines, I conducted an initial validation of the efficacy of microglia depletion through the administration of PLX5622. Consistent with previous reports²⁷⁹, the provision of standard chow containing PLX5622 at 1200 ppm ad libitum for a duration of two weeks resulted in a 90% to 95% reduction of cortical microglia in both WT and *PDGF-h- α -syn* mice. It is noteworthy that no significant impact was observed on other major cell types within the CNS, including astrocytes and neurons (Fig. 22).

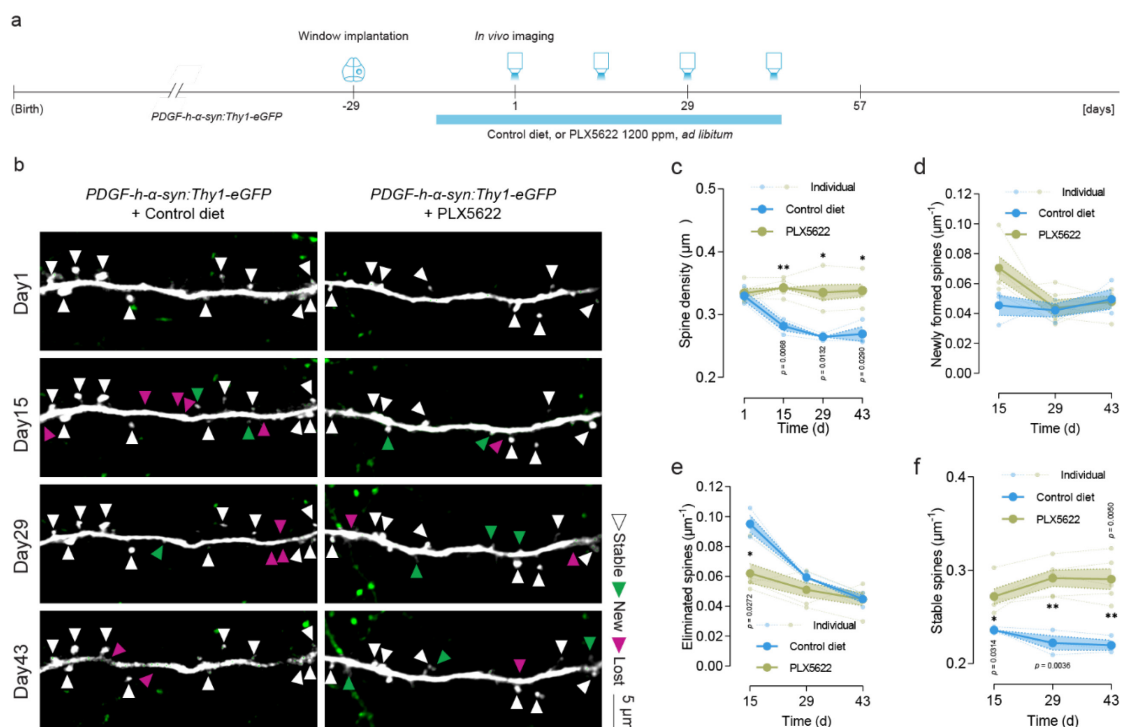


Figure 23 Microglial depletion ameliorates the impairment of dendritic spine structural plasticity in *PDGF-h- α -syn* mice.

a, Experimental design. **b**, Representative *in vivo* two-photon micrographs of apical dendritic tufts. **c-f**, Quantifications of relative spine density (**c**), fractions of gained (**d**), lost spines (**e**), and stable (**f**) in *PDGF-h- α -syn* animals with PLX5622 or control diet treatment. $n = 3$ animals, ~ 474 spines from 24 dendrites in control diet group; 5 animals, ~ 1088 spines from 48 dendrites PLX5622 group (**b-f**). Dot plots represent mean \pm s.e.m. Repeated measures ANOVA with Geisser- Greenhouse correction followed by two-way repeated measures ANOVA with Geisser-Greenhouse correction followed by Bonferroni's multiple comparisons test (**c**: $F_{\text{interaction: durg treatment} \times \text{time}}(3, 18) = 23.99, p < 0.0001$; **d**: $F_{\text{interaction: durg treatment} \times \text{time}}(2, 12) = 2.368, p = 0.1359$; **e**: $F_{\text{interaction: durg treatment} \times \text{time}}(2, 12) = 7.059, p = 0.0094$; **f**: $F_{\text{interaction: durg treatment} \times \text{time}}(2, 12) = 9.647, p = 0.0032$). * $p < 0.05$, ** $p < 0.01$. Scale bars: **b** = 5 μm .

Following the successful validation of PLX5622-induced microglia depletion, *PDGF-h- α -syn:Thy1-eGFP* mice were administered standard chow containing PLX5622 (1200 ppm) or a control compound ad libitum, starting from 2 weeks prior to the imaging and continuing throughout the imaging period. As anticipated, the depletion of microglia resulted in a higher proportion of stable dendritic spines in *PDGF-h- α -syn:Thy1-eGFP* mice fed with PLX5622 chow, in contrast to mice of the same strain but provided with control chow. This increase in stable spines was accompanied by a significant decrease in the dendritic spine elimination rate (Fig. 23). Furthermore, the overall dendritic spine density in PLX5622-fed *PDGF-h- α -syn:Thy1-eGFP* mice remained stable during the 50-day imaging period, which was similar to observations made in *Thy1-eGFP* and *PDGF-h- α -syn:Tspo^{-/-}:Thy1-eGFP* mice.

3.3.4 DBI knockdown mitigates dendritic spine impairment in LBD

Upon establishing the impact of TSPO and microglia depletion on dendritic spine impairment in the context of LBD, I proceeded to investigate the effect of downregulating DBI on the mice of the same LBD pathology.

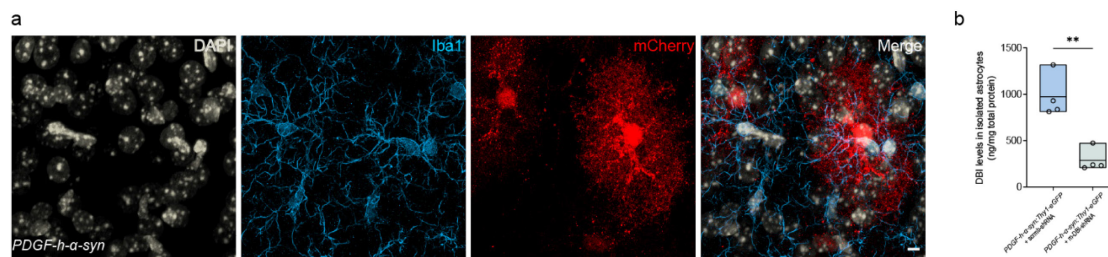


Figure 24 AAV vectors transduce CNS cells and achieve the DBI knockdown in *PDGF-h-α-syn* mice.

a, Representative confocal micrographs after AAV (pAAV-mCherry-U6-m-DBI-shRNA or control AAV vector containing pAAV-mCherry-U6-scrmb-shRNA) injection in *PDGF-h-α-syn* mice, mCherry⁺ signal indicates successful transduction. **b**, Quantitation of astrocytic DBI by ELISA in *PDGF-h-α-syn* mice after injection of AAV containing DBI shRNA or scrambled control RNA. $n = 4$ animals per group (**b**). Dot plots represent mean \pm s.e.m. Two-sided unpaired Student's t test (**b**: $t_{(6)} = 5.167$, $p = 0.0021$). $**p < 0.01$. Scale bars: **b** = 5 μm .

To achieve the aforementioned goal, I utilized AAV that harbor mouse small hairpin RNA (shRNA), which selectively target the messenger RNA (mRNA) responsible for DBI synthesis (m-DBI-shRNA). This approach was utilized to induce the knockdown of DBI mRNA and consequently decrease DBI protein expression. For control purposes, a scrambled shRNA sequence (scrmb-shRNA) was also employed. Both m-DBI-shRNA and scrmb-shRNA were engineered to express under the regulation of the U6 promoter, which facilitates efficient shRNA transduction in a majority of mammalian cells²⁸⁰. Additionally, AAV was designed to express the mCherry reporter, enabling AAV tracking both *in vivo* and *ex vivo*.

Initially, I validated the expression of AAVs containing shRNA through cortical stereotaxic injection in the *PDGF-h-α-syn* mice, as illustrated in Fig. 24a. Robust AAV expression was detectable in cortical brain cells one month after the injection without eliciting any discernible inflammatory responses, such as microgliosis.

Furthermore, in order to specifically evaluate the knockdown effect of the DBI gene in its primary CNS source – the astrocytes, I isolated cortical astrocytes from *PDGF-h-α-syn:Thy1-eGFP* mice one month following their cortical injection with AAV containing either m-DBI-shRNA or scrmb-shRNA. The concentration of DBI protein within these

astrocytes was subsequently quantified via ELISA. As depicted in Fig. 24b, the results revealed that cortical astrocytes derived from mice treated with m-DBI-shRNA exhibited a significant reduction in DBI protein concentration compared to those from mice receiving scrm-shRNA, thereby confirming the effectiveness of the AAV-mediated DBI gene silencing as initially intended.

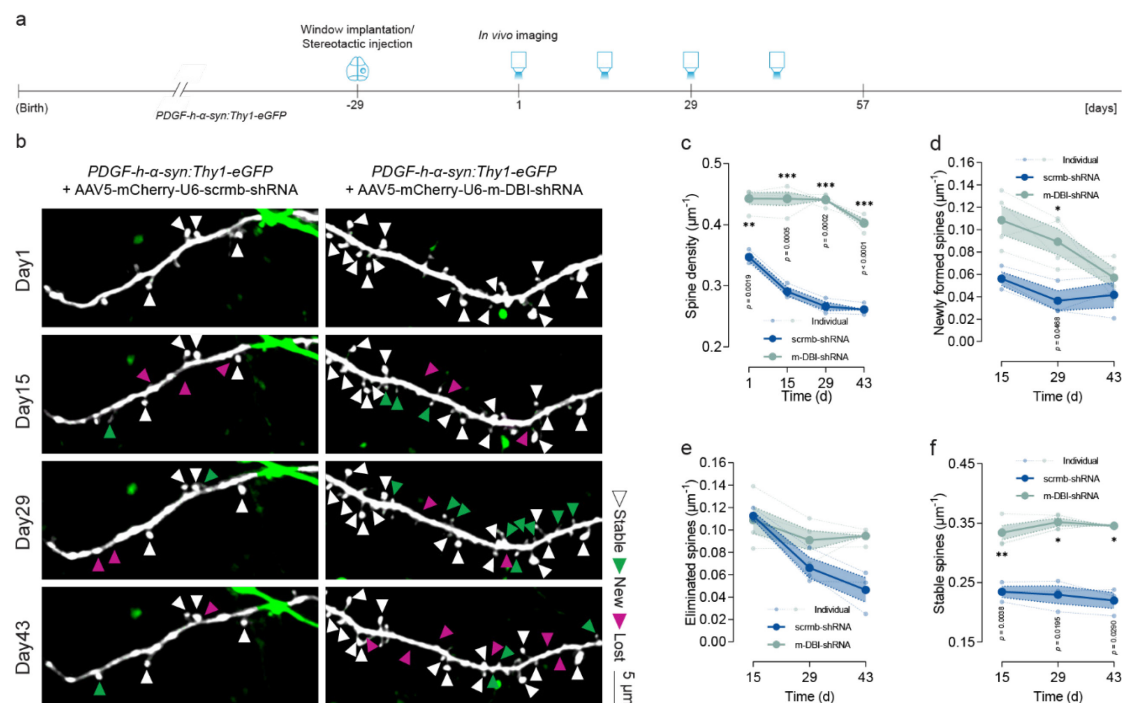


Figure 25 DBI knockdown ameliorates the impairment of dendritic spine structural plasticity in *PDGF-h-α-syn* mice.

a, Experimental design. **b**, Dendritic spine density (**r**), densities of gained (**s**), lost (**t**), and stable (**u**) spines in *PDGF-h-α-syn* animals injected with the AAV vector containing pAAV-mCherry-U6-m-DBI-shRNA or with control AAV vector containing pAAV-mCherry-U6-scram-shRNA. $n = 3$ animals, ~438 spines from 23 dendrites in the scrm-shRNA control group; 5 animals, ~806 spines from 30 dendrites in the m-DBI-shRNA group (**b-f**). Dot plots represent mean \pm s.e.m.. Repeated measures ANOVA with Geisser-Greenhouse correction followed by two-way repeated measures ANOVA with Geisser-Greenhouse correction followed by Bonferroni's multiple comparisons test (**r**: $F_{\text{interaction: gene knockdown} \times \text{time}} (3, 15) = 16.95, p < 0.0001$; **s**: $F_{\text{interaction: gene knockdown} \times \text{time}} (2, 10) = 2.423, p = 0.1387$; **t**: $F_{\text{interaction: gene knockdown} \times \text{time}} (2, 10) = 9.973, p = 0.0042$; **u**: $F_{\text{interaction: gene knockdown} \times \text{time}} (2, 10) = 2.093, p = 0.1741$). * $p < 0.05$, ** $p < 0.01$. Scale bars: **b** = 5 μm .

Upon successful validation of the method, to evaluate the impact of DBI knockdown on dendritic spine plasticity in the LBD mouse model, AAVs containing either m-DBI-

shRNA or scrmb-shRNA were stereotaxically administered into cortical regions of *PDGF-h- α -syn:Thy1-eGFP* mice immediately prior to cranial window implantation.

Subsequent to the one-month convalescence, the *in vivo* imaging was conducted in cortical areas in which the mCherry signal was prominently detectable. In comparison to the control group, of which the mice were transduced with scrmb-shRNA, mice injected with m-DBI-shRNA displayed a significant elevation in dendritic spine density, coupled with a substantially increased proportion of stable spines (Fig. 25).

To validate and more comprehensively understand the impact of DBI knockdown on dendritic spines, I employed *ex vivo* confocal microscopy and 3D-reconstruction-based analysis to further examine the modifications in density and morphology of dendritic spines in *PDGF-h- α -syn:Thy1-eGFP* mice and *Thy1-eGFP* mice, both subjected to stereotaxic injection of AAV containing m-DBI-shRNA or scrmb-shRNA.

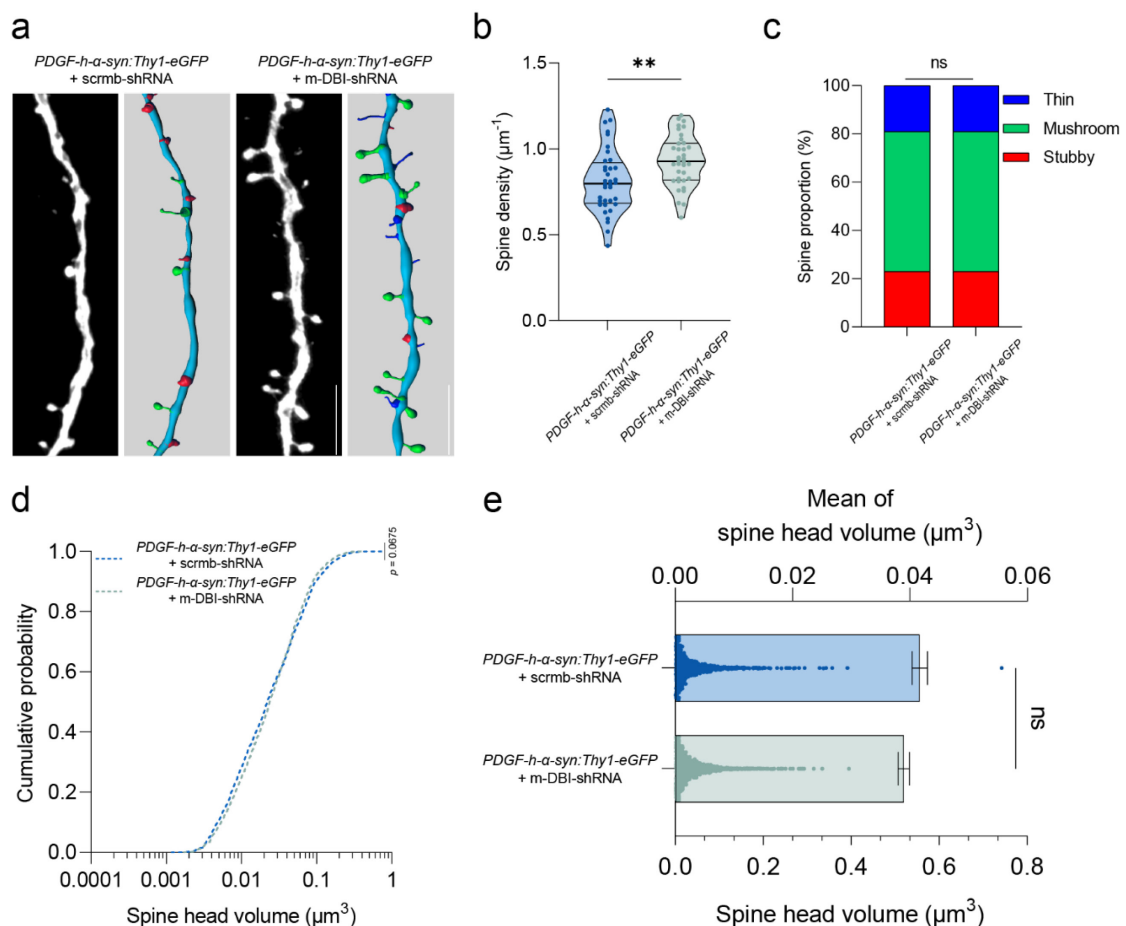


Figure 26 DBI knockdown alters the dendritic spine density and morphology in *PDGF-h- α -syn* mice.

a, Representative confocal micrographs and 3D reconstruction of apical dendritic tufts in the *PDGF-h- α -syn:Thy1-eGFP* animals injected with the AAV vector containing DBI shRNA or with scrambled control RNA. **b**, Quantifications of dendritic spine densities in *PDGF-h- α -syn:Thy1-eGFP* animals (median values and interquartile ranges are plotted). **c**, Quantifications of dendritic spine morphologies in *PDGF-h- α -syn:Thy1-eGFP* animals. **d**, Spine head volume cumulative probabilities *PDGF-h- α -syn:Thy1-eGFP* animals. **e**, Spine head volumes are altered in *PDGF-h- α -syn:Thy1-eGFP* animals (bars show mean and s.e.m., dots represent individual spine head volumes). n = 3 animals per group, scmb-shRNA: ~1592 spines from 36 dendrites, m-DBI-shRNA: ~2096 spines from 36 dendrites (**a**, **b**, **c**, **d**, **e**). Two-sided Mann-Whitney test (**e**: $U = 1638062$, $p = 0.3433$). χ^2 test (**c**: $\chi^2_{(2)} = 0.000$, $p > 0.9999$); Two-sided unpaired Student's t test (**b**: $t_{(70)} = 2.961$, $p = 0.0042$); Kolmogorov-Smirnov test (**d**: $D = 0.05615$, $p = 0.0018$). ** $p < 0.01$. n.s. - no significant difference. Scale bars: **a** = 5 μm .

Consistent with the *in vivo* outcomes, one month post-injection, there was an in observable escalation in cortical dendritic spine density within the transduction regions of m-DBI-shRNA-injected *PDGF-h- α -syn:Thy1-eGFP* mice, in comparison to those receiving scmb-shRNA (Fig. 26a-e). Furthermore, in *Thy1-eGFP* mice subjected to m-DBI-shRNA injection, the dendritic spines located within the transduction regions exhibited a higher density and larger spine head volume, when compared to their scmb-shRNA-injected counterparts (Fig. 27a-e). These findings suggest a plausible role of DBI in the regulation of dendritic spines also in physiological conditions.

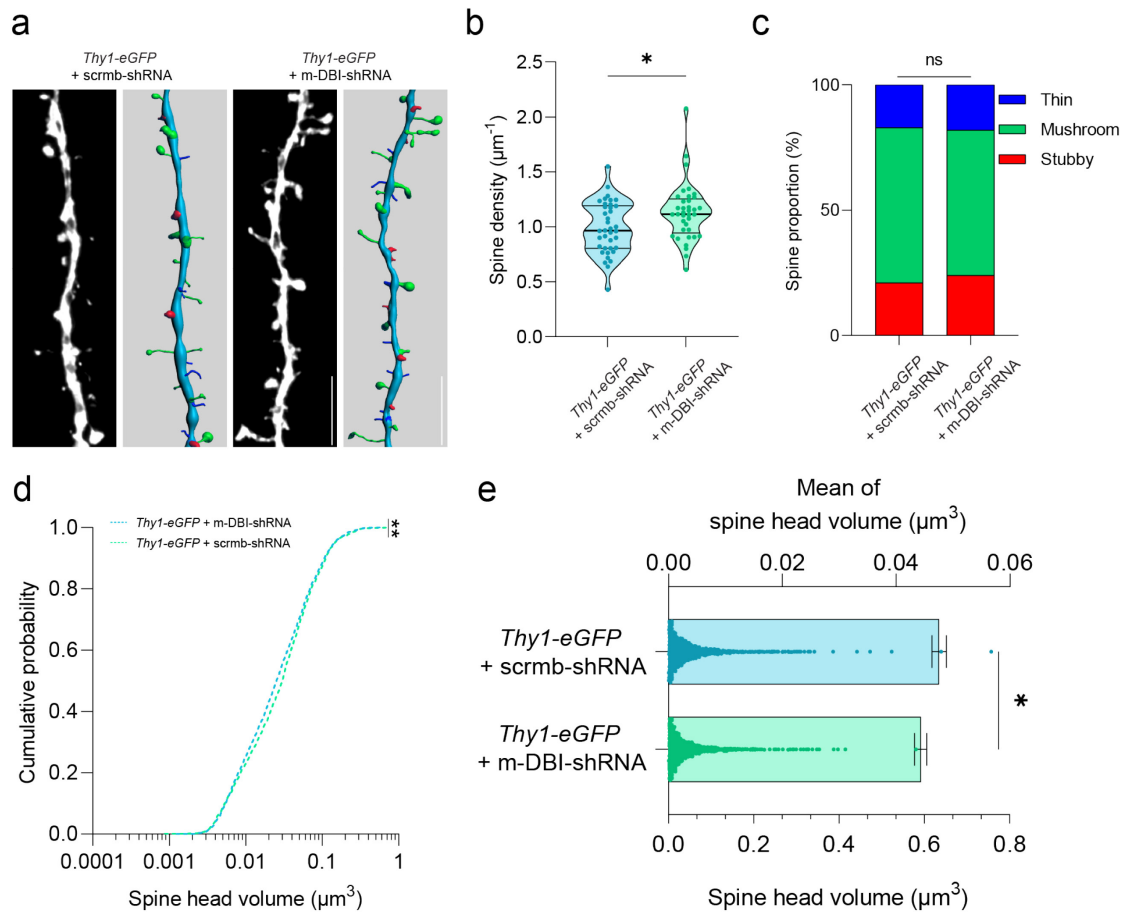


Figure 27 DBI knockdown alters the dendritic spine density and morphology in WT mice.

a, Representative confocal micrographs and 3D reconstruction of apical dendritic tufts in the *Thy1-eGFP* animals injected with the AAV vector containing DBI shRNA or with scrambled control RNA. **b**, Quantifications of dendritic spine densities in *Thy1-eGFP* animals (median values and interquartile ranges are plotted). **c**, Quantifications of dendritic spine morphologies in *Thy1-eGFP* animals. **d**, Spine head volumes are altered in *Thy1-eGFP* animals (bars show mean and s.e.m., dots represent individual spine head volumes). **e**, Spine head volume cumulative probabilities *Thy1-eGFP* animals. $n = 3$ animals per group, scrmb-shRNA: ~2084 spines from 38 dendrites, m-DBI-shRNA: ~2404 spines from 37 dendrites (**a**, **b**, **c**, **d**, **e**); Two-sided Mann-Whitney test (**b**: $U = 507$, $p = 0.0378$; **e**: $U = 2399096$, $p = 0.0145$). χ^2 test (**c**: $\chi^2_{(2)} = 0.3619$, $p = 0.8345$); Kolmogorov-Smirnov test (**d**: $D = 0.04327$, $p = 0.0675$). * $p < 0.05$, ** $p < 0.01$. n.s. - no significant difference. Scale bars: **a** = 5 μm .

To summarize, the findings demonstrate that intercellular DBI-TSPO signaling is vital in the modulation of dendritic spine structural plasticity in the LBD mouse model.

3.4 Altered DBI-TSPO signalling in the brains of patients with LBD

3.4.1 Astrocytic DBI elevates in human LBD patients

In light of the results obtained from the mouse models, I sought to translate my findings to a human context by examining the state of DBI-TSPO signaling in the brain tissue of human patients with LBD. To accomplish this, I employed FFPE brain sections of the medial frontal gyrus obtained from 6 LBD patients and 3 healthy controls, as indicated in Tab. 6.

I evaluated the astrocytic expression of DBI in the aforementioned tissue samples using immunostaining in combination with multichannel super-resolution confocal imaging and 3D reconstruction-based analysis. By quantifying DBI⁺ puncta both within and outside the astrocytes, I observed a significantly higher level of DBI expression in the astrocytes of LBD patients relative to healthy controls (Fig. 28a&b). However, the astrocyte-released DBI⁺ puncta displayed only a marginal increase in astrocyte-adjacent regions in LBD patients compared to healthy controls (Fig. 28c&d).

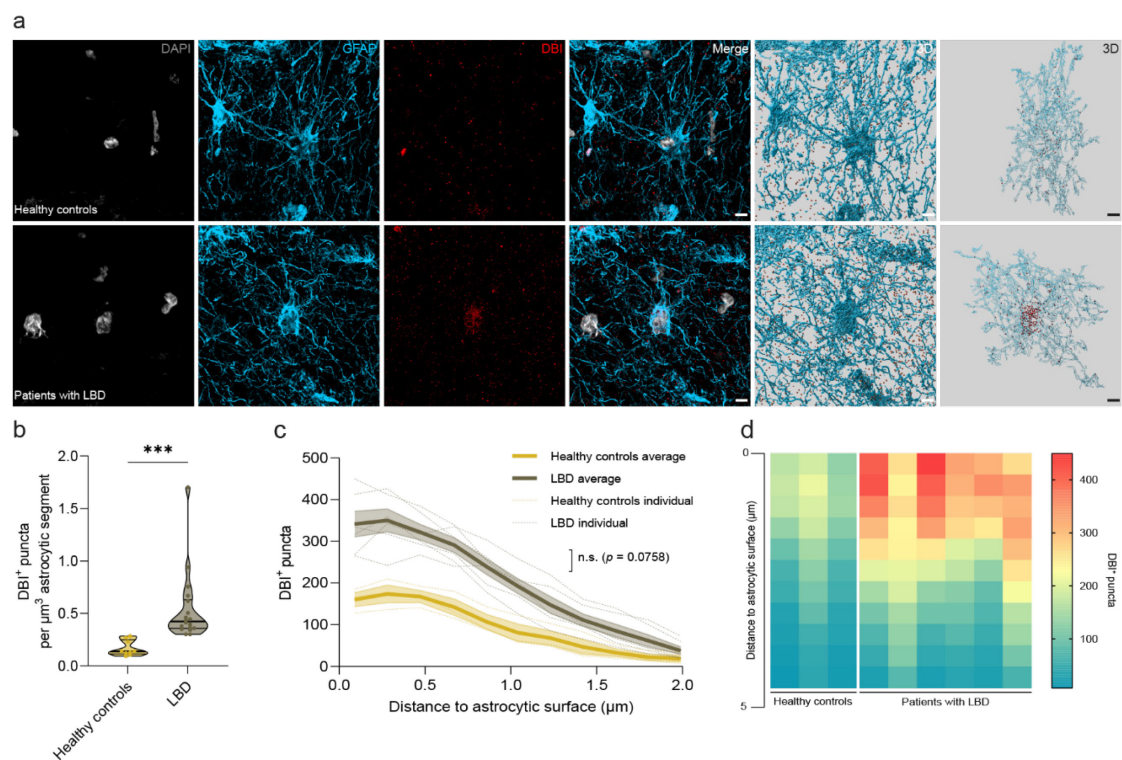


Figure 28 Astrocytes contain elevated levels of DBI to release in the postmortem brains of patients with LBD.

a, Representative confocal micrographs and 3D reconstruction of cortical GFAP⁺ astrocytes and DBI in the brain of patients with LBD and age-matched controls. **b**, Quantification of DBI⁺ puncta in the GFAP⁺ astrocytic segment. **c & d**, Distribution (**c**, in curve and **d**, in the heat map, each lane represents one human sample) of DBI⁺ puncta radiating from astrocytes, showing the release pattern of astrocytic DBI. $n = 3$ for control cases, $n = 6$ for DLB cases (**a-d**). For violin plots, median values and interquartile ranges are plotted. Two-sided Mann-Whitney test (**b**: $U = 0$, $p < 0.0001$). $***p < 0.001$. n.s. - no significant difference. Scale bars = 5 μm .

3.4.2 Microglial TSPO enhances in human LBD patients

Using analogous methods employed in the investigation of astrocytic DBI, I conducted a further inquiry into the microglia situated within the medial frontal gyrus of human brain tissue originating from both LBD patients and healthy controls.

Consistent with previous discoveries pertaining to *PDGF-h- α -syn* mice, the microglia obtained from LBD patients exhibited a significant upregulation of TSPO in contrast to microglia sourced from the healthy controls, signifying an elevated level of microglial activity in the brains of those afflicted with LBD (Fig. 29).

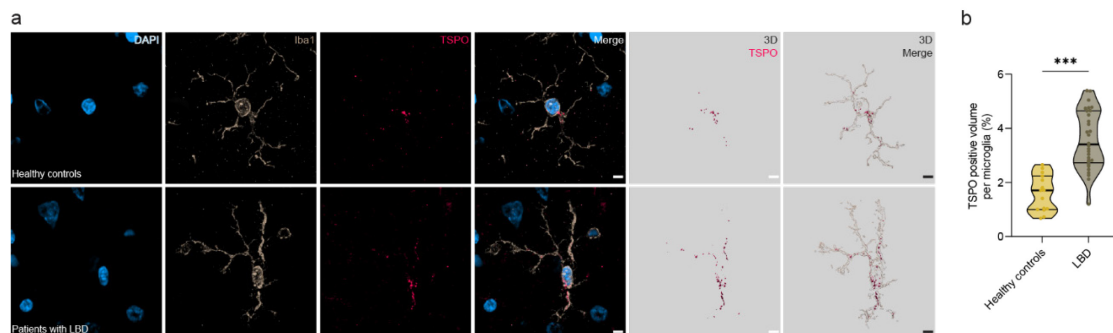


Figure 29 Microglia express higher levels of TSPO in the postmortem brains of patients with LBD.

a, Representative super-resolution confocal micrographs and 3D reconstruction of TSPO⁺ volume in cortical Iba1⁺ microglia from brains of humans with LBD and age-matched controls. **b**, Quantification of TSPO⁺ volume in the Iba1⁺ microglia. $n = 3$ for control cases, $n = 6$ for DLB cases (**a-b**). For violin plots, median values and interquartile ranges are plotted. Two-sided unpaired Student's *t* test (**b**: $t_{(43)} = 6.438$, $p < 0.0001$). $***p < 0.001$. Scale bars = 5 μm .

In light of these observations, it can be inferred that signaling through the astrocytic DBI-microglial TSPO pathway was also amplified in the brains of LBD patients. These

results serve to underscore the proposition that this particular signaling pathway likely plays a significant role in human LBD pathophysiology.

4. Discussion

In my dissertation, a potent intracellular communication mechanism between astrocytic DBI and microglial TSPO in both the mouse model and human subjects afflicted with LBD has been elucidated. This specific communication mechanism exerts a significant influence on the morphological attributes of microglia and their phagocytic activities towards synaptic materials, ultimately culminating in marked alterations in the structural plasticity of dendritic spines. Notwithstanding the inherent association between DBI and TSPO being substantial and the impact of the DBI-TSPO signaling pathway on dendritic spines being significant, there persist essential aspects warranting meticulous examination and a comprehensive discourse.

4.1 DBI exerts regulatory functions beyond TSPO

Within the CNS, TSPO does not exclusively serve as the binding site for DBI. As elucidated in antecedent sections, prior investigations have shown that through the interactions with GABA_ARs, DBI modulates neuronal activity and neurogenesis^{169,255}. Moreover, DBI governs an array of physiological processes extending beyond the confines of the CNS, encompassing the maintenance of energy expenditure¹⁷³, the fortification of the epidermal barrier¹⁷⁴, the facilitation of lipolysis, the regulation of feeding behavior, and body mass¹⁷⁵.

Given the broad spectrum of functions attributed to DBI across various systems, the present study utilized a local approach to mitigate DBI activity in the CNS by administering stereotaxic injections of AAV containing DBI shRNA to mouse cortical regions. This approach specifically targets the local site of DBI production and release, thus avoiding the undesirable effects that might arise from broad DBI ablation. As a result, I did not witness any abnormalities in daily behaviors or postmortem histology examinations (Fig. 24&25) of the animals that received shRNA. The same principle

should also be applied to future studies that aim to investigate therapeutic strategies for mitigating excessive microglial engulfment of synaptic materials by suppressing astrocytic DBI production and release in pathological conditions, such as neurodegenerative diseases. In this regard, it is crucial to restrict DBI manipulation in a system- and, ideally, also cell-type-specific manner, thus ensuring that the desired ameliorative effect on synapses can be achieved without inducing any side effects that may prove detrimental to the brain or the entire organism.

It is also imperative to acknowledge that the impact of DBI on dendritic spines may not be solely mediated by microglia and their TSPO. As mentioned before, DBI regulates neurogenesis by binding to $\gamma 2$ subunits of GABA_ARs as a negative allosteric modulator. Studies utilizing shRNA-mediated knockdown of DBI have demonstrated enhanced neurogenesis in postnatal mice¹⁶⁹. Notably, while neurogenesis predominantly occurs during the perinatal period, recent evidence has shown that altering GABA signaling can modulate dendritic branching and synaptic formation in the adult mouse brain²⁸¹. This suggests that, across different developmental stages, DBI may influence dendritic spines via the GABA signaling pathway, in addition to the DBI-TSPO signaling pathway delineated in the present study. Hence, a comprehensive investigation of the effects of DBI on the GABA signaling pathway and its impact on dendritic spines is warranted.

4.2 Non-microglial TSPO alters in CNS disorders

In contrast to the predominantly astrocytic origin of DBI in the CNS^{238,245}, the presence of TSPO has been identified in various CNS cell types, including microglia, neurons, endothelial cells, and astrocytes^{77,142}. In the present study, I investigated the expression pattern of TSPO in all major CNS cell types mentioned above in the mouse cortex. The results showed that, in *PDGF-h- α -syn* mice, only microglial TSPO exhibited a substantial increase relative to other cell types compared to their WT counterparts. Moreover, the PLA signal indicating the bindings between DBI and TSPO was also

primarily observed to elevate in microglia in the *PDGF-h- α -syn* mice. Therefore, the findings suggest that the response of TSPO to increased DBI in the *PDGF-h- α -syn* mice occurs predominantly in microglia, which is consistent with previous studies showing TSPO as a sensitive biomarker for CNS neurodegenerations¹⁴³ and microglia as the main responders^{121,123,144,282} to these disorders.

Nevertheless, this observation does not necessarily preclude the involvement of other types of CNS cells in the LBD pathophysiology via TSPO. Previous studies have demonstrated that in a rat model of PD, an increased level of TSPO was observed in dopaminergic neurons that were impacted by PD pathology²⁸³. Furthermore, overexpression of TSPO in SH-SY5Y cells, a human neuroblastoma cell line²⁸⁴, induced dysregulation of cellular reduction–oxidation (redox), mitochondria ubiquitylation, and autophagolysosomal response²⁸³. Similarly, research has suggested that neuronal TSPO could be upregulated via chemogenetic, physiological, or psychopharmacological stimulation of neuronal activity in adult mice¹⁴². These findings indicate that TSPO of other CNS cell types may also become responsive under pathological conditions.

Concomitant with its ubiquitous expression, TSPO possesses manifold roles that extend beyond its regulation of microglial phagocytosis. As mentioned in the preceding sections, TSPO participates in a plethora of biological processes, such as steroidogenesis^{168,285,286}, mitochondrial homeostasis^{140,287}, and apoptosis^{141,288}, in diverse cell types spanning various systems. Moreover, perturbations to TSPO that result from either pharmacological interventions^{77,141} or pathological states^{283,289} have been shown to engender deleterious consequences to the cells it inhabits.

Thus, it stands to reason that under CNS disorders such as LBD, DBI-induced TSPO activation, albeit at a lesser level, could still potentially take place in other types of CNS cells besides microglia, affecting a broad range of biological functions beyond

microglial phagocytosis. These alterations are also likely to have implications in LBD pathophysiology and, therefore, warrant further investigation in future studies.

4.3 DBI-TSPO signaling as a general pathway for synaptic regulation

In conjunction with the observed changes within the LBD context delineated in this study, significant alterations have been ascertained in both the DBI and TSPO, either concurrently or individually, across a diverse array of CNS disorders.

As mentioned before, subsequent to the initial *in vitro* experimental explication²⁹⁰ and ensuing *in vivo* observations in progressive dementia²⁹¹, aberrant expression of TSPO within the CNS has been identified in numerous CNS disorders and used as a biomarker for microglial activity. These disorders encompass a spectrum of neurodegenerative diseases, including AD^{143,292,293}, multiple system atrophy²⁹⁴, progressive supranuclear palsy²⁹⁵, corticobasal degeneration^{296,297}, frontotemporal dementia^{298,299}, and amyotrophic lateral sclerosis³⁰⁰. Moreover, neuropsychiatric conditions, such as bipolar disorder³⁰¹, major depressive disorder³⁰², and schizophrenia³⁰³, as well as neurodevelopmental disorders like autism spectrum disorder (ASD)³⁰⁴, have been associated with abnormal TSPO expression within the CNS. On top of this, it merits attention that TSPO expression in these diseases tends to diverge in distinct directions. While it generally escalates in response to neurodegeneration^{143,292-300}, a diminished level of TSPO has been consistently observed in specific neuropsychiatric disorders, such as ASD³⁰⁴.

Remarkably, in all heretofore mentioned CNS maladies, the cognitive dysfunction arising from synaptic dysregulation manifests as a principal syndrome. Additionally, the discernible dendritic spine density and their projected developmental trajectory⁴⁵ roughly exhibit a conspicuous inverse correlation with the TSPO expression^{143,292-300,304} in these afflictions. For instance, a reduction in dendritic spine density has been documented in numerous neurodegenerative diseases, wherein TSPO expression is

characteristically elevated¹⁰¹. In contrast, an anomalously augmented dendritic spine density was observed in individuals diagnosed with ASD, wherein TSPO levels were found to be diminished relative to healthy controls¹⁰¹. Considering the crucial function of microglia in the modulation of synaptic plasticity^{305,306}, along with the TSPO-mediated microglial phagocytosis of synaptic constituents explicated in the current investigation and the antecedent one⁷⁷, it appears highly feasible to hypothesize that TSPO-mediated microglial alterations likewise contribute to the synaptic dysregulation witnessed in these CNS disorders.

It is also worth noting that, as mentioned in the foregoing sections, TSPO is a ubiquitously expressed protein^{142,283} with a multitude of biological functions^{140,141,168,285-288}. As a result, any alteration in TSPO expression, in addition to microglia-related synaptic dysregulation, may denote aberrations in any of those processes in the TSPO-containing cells. Consequently, this aspect should be contemplated on each occasion when interpreting cell-type unspecific TSPO expression, such as PET.

In contrast to TSPO, a paucity of research exists regarding the perturbations of DBI in non-LBD CNS disorders. As mentioned in preceding sections, abnormal alterations of DBI have been shown in a multitude of CNS disorders, spanning neurodegenerative^{258,259}, neuroinflammatory²⁵⁸, psychiatric²⁵⁹⁻²⁶¹, and neurodevelopmental²⁶² disorders in cerebrospinal fluid and/or serum. In particular, it has been shown that A β peptide 25-35 increases DBI release from cultured astrocytes via the *N*-formyl peptide receptors²⁵³. Considering the drastically activated microglia around A β plaques in the AD context³⁰⁷, the elevated DBI strongly hints at the existence of the DBI-TSPO signaling pathway in the same areas. In line with this, in other CNS disorders mentioned above, the documented fluctuations of DBI also bear a generally positive correlation with TSPO^{258,259,262}. Besides these "pure" CNS disorders, perturbations in DBI regulation have been discerned in patients suffering from peripherally induced CNS disorders, such as hepatic encephalopathy³⁰⁸. This

finding is in accordance with prior investigations positing that DBI expression is fundamentally multisystemic, thereby insinuating that peripheral DBI might likewise contribute to the pathophysiology of CNS disorders.

Complementary to these antecedent studies, as illustrated in previous sections, I have observed an augmented dendritic spine density in *Thy1-eGFP* mice subjected to DBI knockdown via shRNA, utilizing both *in vivo* and *ex vivo* methods (Fig. 27). This observation elucidates the notion that the DBI-TSPO signaling pathway exerts a modulatory effect on synaptic plasticity, even within the confines of physiological circumstances.

In essence, the accumulated evidence implies that the DBI-TSPO signaling pathway likely constitutes one of the fundamental mechanisms governing synaptic regulation, encompassing both physiological and pathological contexts. It is exceedingly compelling to postulate that in an array of CNS disorders, such as AD, the dysregulated DBI-TSPO signaling pathway engenders anomalies in synaptic plasticity, culminating in cognitive impairment. Therefore, investigating the potential amelioration of synaptic abnormalities and cognitive deficits in these devastating diseases through the modulation of the DBI-TSPO signaling pathway represents an attractive avenue for future research.

4.4 The penta-partite synapse is an integral unit for synaptic studies

From an ontological standpoint, alterations in dendritic spine structural plasticity, instigated by astrocyte-microglia interactions, embody the essence of the penta-partite synapse³⁰⁹ – a relatively nascent paradigm garnering growing acknowledgment. This concept delineates a theoretical synapse that encompasses five constituents: the presynaptic and postsynaptic structures, perisynaptic astrocytes, extracellular matrix (ECM), and perisynaptic microglia. The foundational idea of this schema is that the preservation or the impairment of synaptic functionality is not exclusively contingent

upon neurons; rather, it necessitates intricate interplay between neurons and non-neuronal cells. In the context of this study, the non-neuronal cells encompass astrocytes and microglia.

The role of stimulated microglia in the dislocation of synapses in the context of CNS pathologies has been widely acknowledged and continuously scrutinized over an extended period^{305,306,310}. Contrarily, astrocytes were initially characterized as fulfilling a predominantly auxiliary capacity in relation to neurons through the modulation of synaptic formation, transmission, and plasticity^{94,177-182,216-227,229}. Consequently, astrocytes were incorporated into the concept of the tri-partite synapse alongside pre- and postsynaptic compartments³¹¹. As the investigations on astrocytes progress, in recent years, their capacity to directly phagocytose synaptic compartments^{110,312} has been gradually discerned and examined.

Concurrent with the astrocytic DBI-microglial TSPO signaling pathway presented in this investigation, as mentioned in preceding sections, research endeavors centered on intercellular crosstalk among heterogeneous glial cells and the subsequent implications for the CNS physiological and pathological processes are currently limited yet experiencing a notable intensification^{91,230,231,233,313}. The interaction between microglia and astrocyte has been gradually regarded as a primary mechanism that regulates synapses instead of a byproduct supplementing the functions of individual glial cell types.

Unlike the perception of "cellular" compartments that usually regards them as the primary drivers of biological functions, the ECM is often perceived merely as the "adhesive" of the nervous system, with its vital roles frequently underestimated. However, rather than a mere "adhesive," the ECM constitutes a highly intricate and dynamic molecular network³¹⁴, encompassing roughly 20% of brain volume³¹⁵, and is present in nearly every structure within the CNS³¹⁶. Apart from functioning as an extracellular scaffold to maintain tissue architecture³¹⁷, the ECM is intimately related to

regulating synaptic transductions and their structural plasticity by modulating the distribution of critical molecules³¹⁸, such as neurotransmitters³¹⁵, ions³¹⁹⁻³²¹, and membrane receptors^{322,323}. Previous research has indicated that the ECM can affect astrocytic functions^{324,325}, including secreted astrocytic extracellular vesicles. However, the impact of ECM on astrocytic DBI, as well as the underlying mechanisms, warrants further investigation in subsequent studies.

In addition to astrocytes, antecedent investigations have revealed that the ECM maintains a strong association with microglia in the brains of both mice and humans. Evidence has shown that in individuals afflicted with AD, as a part of the pathophysiology, activated microglia exhibit a propensity to engulf an excessive amount of perineuronal ECM^{326,327}. Concomitant with AD, microglia-associated aberrations in ECM have been consistently documented across an extensive array of CNS disorders, encompassing multiple sclerosis³²⁸, Huntington's disease³²⁹, and schizophrenia^{330,331}. Furthermore, a recent investigation has elucidated that, in adult brains, microglia exhibit phagocytic behavior and clear perisynaptic ECM in response to neuronal IL-33, consequently leading to an augmentation in dendritic spine formation and the precision of fear memory¹¹⁴.

These discoveries collectively underscore the intricate and intimate interplay among the ECM, astrocytes, and microglia under both physiological and pathological circumstances. In view of these observations, it stands to reason that the ECM may also contribute to the DBI-TSPO signaling pathway delineated herein. Moreover, from a more comprehensive perspective, as an integral component of the penta-partite synapse, it stands to reason that the ECM is implicated in synaptic pathologies in the context of diverse CNS disorders.

In summation, these revelations emphasize the significance of scrutinizing synaptic function or dysfunction through a holistic^{332,333} lens. The influence exerted by non-neuronal cells upon neurons transcends a simple bidirectional relationship and instead

manifests as a synergistic force derived from a complex and multifaceted interaction. Further explorations on astrocyte-microglia communication, or more intricate dialogues among the constituents of the penta-partite synapse in both healthy and pathological states, should be deemed as paramount subjects for forthcoming inquiries of synaptic functionality.

5. Conclusion

Based on the findings elucidated in the antecedent sections, several conclusions can be inferred.

Primarily, in both the mouse model of LBD and human patients afflicted with LBD, astrocytes show an augmented secretion of DBI, which in turn excessively binds to TSPO in microglia, thereby instigating an upregulation of TSPO activity.

Consequent to heightened TSPO activity, both the morphological and behavioral traits of microglia undergo significant alterations. Microglia manifest aberrant phagocytic activity, engulfing an excessive amount of synaptic materials, thereby precipitating a deleterious effect on dendritic spine structural plasticity and density.

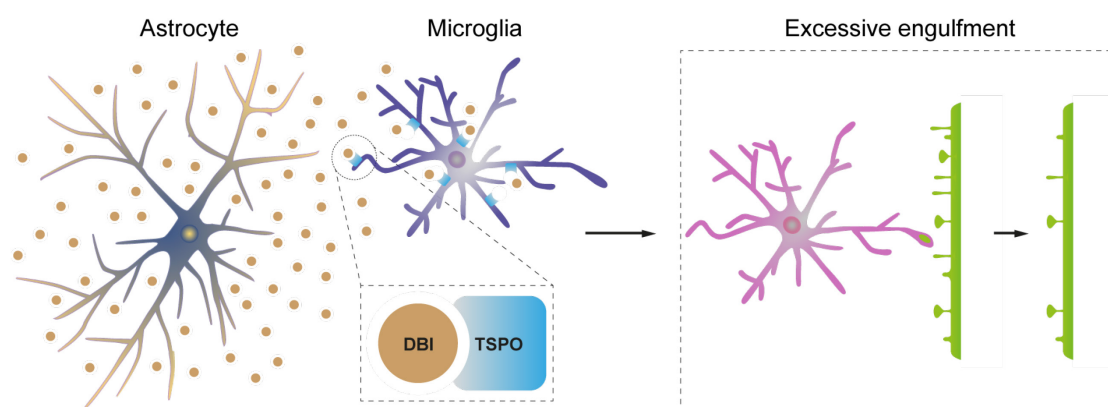


Figure 30 Schematic diagram.

In LBD, the increased level of astrocytic DBI binds to TSPO on microglia, leading to excessive microglial engulfment of synaptic materials and subsequent impaired structural plasticity of dendritic spines.

Furthermore, all these perturbations in microglial behavior and dendritic spine dynamics in LBD pathology are dependent on the exacerbated DBI-TSPO signaling pathway, as evidenced by the ameliorative effects observed upon selective suppression of either DBI or TSPO. Specifically, AAV-mediated knockdown of DBI or genetic knockout of TSPO resulted in mitigated microglial phagocytosis of synaptic materials and attenuated loss of dendritic spines in the LBD mouse model.

In summation, the current investigation underscores the pivotal role of the DBI-TSPO signaling pathway between astrocytes and microglia as a key driving force behind dendritic spine loss in LBD. Furthermore, the interruption of this pathway exerts a significant ameliorative effect on impaired dendritic spine plasticity, suggesting that the DBI-TSPO signaling pathway holds promise as a prospective therapeutic target for mitigating synaptic loss in LBD pathology.

List of Figures and Tables

Figure 1 Scheme of an asymmetric synapse.	7
Figure 2 Scheme of dendritic spines of different morphology and filopodium.....	9
Figure 3 Synaptic pruning by microglia.	13
Figure 4 Schematic diagram of excessive spine loss upon altered synaptic pruning.	15
Figure 5 Outline of one-photon and two-photon excitation.	29
Figure 6 Schematic diagram of the PLA reaction.....	40
Figure 7 Long-term <i>in vivo</i> two-photon imaging of dendritic spines.	50
Figure 8 3D reconstruction and analysis for distribution of astrocytic DBI.	51
Figure 9 3D reconstruction and analysis for microglial TSPO and their engulfment of synaptic materials.	52
Figure 10 Elevated astrocytic DBI production and release in <i>PDGF-h-α-syn</i> mice....	59
Figure 11 Elevated levels of DBI produced in astrocytes and released in the brains of <i>PDGF-h-α- syn</i> mice.	60
Figure 12 TSPO expression in different cell types of <i>PDGF-h-α-syn</i> and WT mice...	61
Figure 13 Elevated TSPO expression in microglia of <i>PDGF-h-α-syn</i> mice.....	62
Figure 14 Elevation of DBI-TSPO bindings in <i>PDGF-h-α-syn</i> mice.	63
Figure 15 Altered microglial morphology in <i>PDGF-h-α-syn</i> mice.	65
Figure 16 Increased DBI-TSPO bindings in microglia of <i>PDGF-h-α-syn</i> mice.....	67
Figure 17 Astrocytic DBI confers microglial synaptic engulfment via TSPO.	69
Figure 18 DBI neutralization in brain ECF and synaptosome purification.	70

Figure 19 TSPO-dependent synaptosome uptake by microglia.....	72
Figure 20 Structural plasticity of dendritic spines is impaired in <i>PDGF-h-α-syn</i> mice.	74
Figure 21 The impairment of dendritic spine structural plasticity is TSPO-dependent in <i>PDGF-h-α-syn</i> mice.	76
Figure 22 Long-term microglia elimination does not affect astrocytes or neurons in <i>PDGF-h-α-syn</i> and WT mice.	78
Figure 23 Microglial depletion ameliorates the impairment of dendritic spine structural plasticity in <i>PDGF-h-α-syn</i> mice.....	79
Figure 24 AAV vectors transduce CNS cells and achieve the DBI knockdown in <i>PDGF- h-α-syn</i> mice.....	80
Figure 25 DBI knockdown ameliorates the impairment of dendritic spine structural plasticity in <i>PDGF-h-α-syn</i> mice.....	81
Figure 26 DBI knockdown alters the dendritic spine density and morphology in <i>PDGF- h-α-syn</i> mice.....	83
Figure 27 DBI knockdown alters the dendritic spine density and morphology in WT mice.....	84
Figure 28 Astrocytes contain elevated levels of DBI to release in the postmortem brains of patients with LBD.	86
Figure 29 Microglia express higher levels of TSPO in the postmortem brains of patients with LBD.....	86
Figure 30 Schematic diagram.	97

Table 1 Representatives of synthetic TSPO ligands and their effects on microglia... 18	18
Table 2 Representatives of endogenous TSPO ligands and their functions.....20	20
Table 3 Commonly used fluorophores and two-photon excitation wavelengths.30	30
Table 4 Mouse strains used in this study.....32	32
Table 5 Primers for genotyping.....33	33
Table 6 Characterization of postmortem human tissue samples used in this study. .34	34
Table 7 Antibodies used in this study.....36	36
Table 8 AAVs used in this study.48	48
Table 9 Key resources used in this study.54	54
Table 10 Key software used in this study.....56	56

Bibliography

- 1 Lippa, C. *et al.* Dlb and Pdd Boundary Issues: Diagnosis, Treatment, Molecular Pathology, and Biomarkers. *Neurology* **68**, 812-819 (2007).
- 2 Walker, Z., Possin, K. L., Boeve, B. F. & Aarsland, D. Lewy Body Dementias. *The Lancet* **386**, 1683-1697 (2015).
- 3 Parkinson, J. An Essay on the Shaking Palsy. *The Journal of neuropsychiatry and clinical neurosciences* **14**, 223-236 (2002).
- 4 Goetz, C. G. Charcot the Clinician: The Tuesday Lessons. *New York: Raven* (1987).
- 5 Jefferson, M. James Parkinson, 1775-1824. *British Medical Journal* **2**, 601 (1973).
- 6 Sagar, J. Systema Morborum Symptomaticum Ecs. *Vienna Kraus, Class vii* **22**, 3 (1771).
- 7 Stern, G. Did Parkinsonism Occur before 1817? *Journal of neurology, neurosurgery, and psychiatry* **52**, 11 (1989).
- 8 Lewy, F. Pathologische Anatomie Handbuch Der Neurologie. (1912).
- 9 Holdorff, B. Fritz Heinrich Lewy (1885-1950). *Journal of neurology* **253**, 677 (2006).
- 10 Trétiakoff, C. Contribution a L'etude De L'anatomie Pathologique Du Locus Niger De Soemmering Avec Quelques Deduction Relatives a La Pathogenie Des Troubles Du Tonus Musculaire Et De La Maladie De Parkinson. *Theses de Paris* (1919).
- 11 Goedert, M., Spillantini, M. G., Del Tredici, K. & Braak, H. 100 Years of Lewy Pathology. *Nature Reviews Neurology* **9**, 13-24 (2013).
- 12 Greenfield, J. & Bosanquet, F. D. The Brain-Stem Lesions in Parkinsonism. *Journal of neurology, neurosurgery, and psychiatry* **16**, 213 (1953).
- 13 Bethlem, J. & Jager, W. D. H. The Incidence and Characteristics of Lewy Bodies in Idiopathic Paralysis Agitans (Parkinson's Disease). *Journal of neurology, neurosurgery, and psychiatry* **23**, 74 (1960).
- 14 Kosaka, K. Lewy Body Disease and Dementia with Lewy Bodies. *Proceedings of the Japan Academy, Series B* **90**, 301-306 (2014).
- 15 Kosaka, K. & Mehraein, P. Dementia-Parkinsonism Syndrome with Numerous Lewy Bodies and Senile Plaques in Cerebral Cortex. *Archiv für Psychiatrie und Nervenkrankheiten* **226**, 241-250 (1979).
- 16 Kosaka, K., Tsuchiya, K. & Yoshimura, M. Lewy Body Disease with and without Dementia: A Clinicopathological Study of 35 Cases. *Clinical neuropathology* **7**, 299-305 (1988).

- 17 Outeiro, T. F. *et al.* Dementia with Lewy Bodies: An Update and Outlook. *Molecular neurodegeneration* **14**, 1-18 (2019).
- 18 McKeith, I. G. *et al.* Diagnosis and Management of Dementia with Lewy Bodies: Third Report of the Dlb Consortium. *Neurology* **65**, 1863-1872 (2005).
- 19 Aarsland, D., Zaccai, J. & Brayne, C. A Systematic Review of Prevalence Studies of Dementia in Parkinson's Disease. *Movement disorders: official journal of the Movement Disorder Society* **20**, 1255-1263 (2005).
- 20 Williams-Gray, C. H. *et al.* The Campaign Study of Parkinson's Disease: 10-Year Outlook in an Incident Population-Based Cohort. *Journal of Neurology, Neurosurgery & Psychiatry* **84**, 1258-1264 (2013).
- 21 Emre, M. *et al.* Clinical Diagnostic Criteria for Dementia Associated with Parkinson's Disease. *Movement disorders: official journal of the Movement Disorder Society* **22**, 1689-1707 (2007).
- 22 Jones, S. V. & O'brien, J. The Prevalence and Incidence of Dementia with Lewy Bodies: A Systematic Review of Population and Clinical Studies. *Psychological medicine* **44**, 673-683 (2014).
- 23 McKeith, I. G. *et al.* Consensus Guidelines for the Clinical and Pathologic Diagnosis of Dementia with Lewy Bodies (Dlb): Report of the Consortium on Dlb International Workshop. *Neurology* **47**, 1113-1124 (1996).
- 24 Beyer, K. A-Synuclein Structure, Posttranslational Modification and Alternative Splicing as Aggregation Enhancers. *Acta neuropathologica* **112**, 237-251 (2006).
- 25 Withers, G. S., George, J. M., Banker, G. A. & Clayton, D. F. Delayed Localization of Synelfin (Synuclein, Nacp) to Presynaptic Terminals in Cultured Rat Hippocampal Neurons. *Developmental brain research* **99**, 87-94 (1997).
- 26 Zhang, L. *et al.* Semi-Quantitative Analysis of A-Synuclein in Subcellular Pools of Rat Brain Neurons: An Immunogold Electron Microscopic Study Using a C-Terminal Specific Monoclonal Antibody. *Brain research* **1244**, 40-52 (2008).
- 27 Lee, S.-J., Jeon, H. & Kandrор, K. V. Alpha-Synuclein Is Localized in a Subpopulation of Rat Brain Synaptic Vesicles. *Acta Neurobiol Exp (Wars)* **68**, 509-515 (2008).
- 28 Scott, D. A. *et al.* A Pathologic Cascade Leading to Synaptic Dysfunction in A-Synuclein-Induced Neurodegeneration. *Journal of Neuroscience* **30**, 8083-8095 (2010).
- 29 Burré, J. *et al.* A-Synuclein Promotes Snare-Complex Assembly *in vivo* and *in Vitro*. *Science* **329**, 1663-1667 (2010).
- 30 Hijaz, B. A. & Volpicelli-Daley, L. A. Initiation and Propagation of A-Synuclein Aggregation in the Nervous System. *Molecular neurodegeneration* **15**, 1-12 (2020).

- 31 Cremades, N. & Dobson, C. M. The Contribution of Biophysical and Structural Studies of Protein Self-Assembly to the Design of Therapeutic Strategies for Amyloid Diseases. *Neurobiology of Disease* **109**, 178-190 (2018).
- 32 Spillantini, M. G., Crowther, R. A., Jakes, R., Hasegawa, M. & Goedert, M. A-Synuclein in Filamentous Inclusions of Lewy Bodies from Parkinson's Disease and Dementia with Lewy Bodies. *Proceedings of the National Academy of Sciences* **95**, 6469-6473 (1998).
- 33 Polymeropoulos, M. H. *et al.* Mutation in the A-Synuclein Gene Identified in Families with Parkinson's Disease. *science* **276**, 2045-2047 (1997).
- 34 Krüger, R. *et al.* Alasopro Mutation in the Gene Encoding A-Synuclein in Parkinson's Disease. *Nature genetics* **18**, 106-108 (1998).
- 35 Zarranz, J. J. *et al.* The New Mutation, E46k, of A-Synuclein Causes Parkinson and Lewy Body Dementia. *Annals of Neurology: Official Journal of the American Neurological Association and the Child Neurology Society* **55**, 164-173 (2004).
- 36 Tanner, C. M. The Role of Environmental Toxins in the Etiology of Parkinson's Disease. *Trends in neurosciences* **12**, 49-54 (1989).
- 37 Klawans, H. L., Stein, R. W., Tanner, C. M. & Goetz, C. G. A Pure Parkinsonian Syndrome Following Acute Carbon Monoxide Intoxication. *Archives of neurology* **39**, 302-304 (1982).
- 38 Uitti, R. J. *et al.* Parkinsonism Induced by Solvent Abuse. *Annals of Neurology: Official Journal of the American Neurological Association and the Child Neurology Society* **35**, 616-619 (1994).
- 39 Gorell, J. M., Johnson, C., Rybicki, B., Peterson, E. & Richardson, R. The Risk of Parkinson's Disease with Exposure to Pesticides, Farming, Well Water, and Rural Living. *Neurology* **50**, 1346-1350 (1998).
- 40 Braak, H. *et al.* Staging of Brain Pathology Related to Sporadic Parkinson's Disease. *Neurobiol Aging* **24**, 197-211 (2003).
- 41 George, S., Rey, N. L., Reichenbach, N., Steiner, J. A. & Brundin, P. A-Synuclein: The Long Distance Runner. *Brain pathology* **23**, 350-357 (2013).
- 42 Blumenstock, S. *et al.* Seeding and Transgenic Overexpression of Alpha-Synuclein Triggers Dendritic Spine Pathology in the Neocortex. *EMBO molecular medicine* **9**, 716-731 (2017).
- 43 Luk, K. C. *et al.* Pathological A-Synuclein Transmission Initiates Parkinson-Like Neurodegeneration in Nontransgenic Mice. *Science* **338**, 949-953 (2012).
- 44 Zaja-Milatovic, S. *et al.* Selective Dendritic Degeneration of Medium Spiny Neurons in Dementia with Lewy Bodies. *Neurology* **66**, 1591-1593 (2006).
- 45 Forrest, M. P., Parnell, E. & Penzes, P. Dendritic Structural Plasticity and Neuropsychiatric Disease. *Nature Reviews Neuroscience* **19**, 215-234 (2018).

- 46 Herms, J. & Dorostkar, M. M. Dendritic Spine Pathology in Neurodegenerative Diseases. *Annual Review of Pathology: Mechanisms of Disease* **11**, 221-250 (2016).
- 47 Cajal, S. R. Y. *Recollections of My Life*. Vol. 8 (MIT press, 1989).
- 48 Yuste, R. & Bonhoeffer, T. Genesis of Dendritic Spines: Insights from Ultrastructural and Imaging Studies. *Nature Reviews Neuroscience* **5**, 24-34 (2004).
- 49 Johnston, D., Magee, J. C., Colbert, C. M. & Christie, B. R. Active Properties of Neuronal Dendrites. *Annual review of neuroscience* **19**, 165-186 (1996).
- 50 Kasai, H., Fukuda, M., Watanabe, S., Hayashi-Takagi, A. & Noguchi, J. Structural Dynamics of Dendritic Spines in Memory and Cognition. *Trends in neurosciences* **33**, 121-129 (2010).
- 51 Hering, H. & Sheng, M. Dendritic Spines: Structure, Dynamics and Regulation. *Nature Reviews Neuroscience* **2**, 880-888 (2001).
- 52 Chicurel, M. E. & Harris, K. M. Three-Dimensional Analysis of the Structure and Composition of Ca³ Branched Dendritic Spines and Their Synaptic Relationships with Mossy Fiber Boutons in the Rat Hippocampus. *Journal of comparative neurology* **325**, 169-182 (1992).
- 53 Feng, W. & Zhang, M. Organization and Dynamics of Pdz-Domain-Related Supramodules in the Postsynaptic Density. *Nature Reviews Neuroscience* **10**, 87-99 (2009).
- 54 Bardo, S., Cavazzini, M. G. & Emptage, N. The Role of the Endoplasmic Reticulum Ca²⁺ Store in the Plasticity of Central Neurons. *Trends in pharmacological sciences* **27**, 78-84 (2006).
- 55 Li, Z., Okamoto, K.-I., Hayashi, Y. & Sheng, M. The Importance of Dendritic Mitochondria in the Morphogenesis and Plasticity of Spines and Synapses. *Cell* **119**, 873-887 (2004).
- 56 Ostroff, L. E., Fiala, J. C., Allwardt, B. & Harris, K. M. Polyribosomes Redistribute from Dendritic Shafts into Spines with Enlarged Synapses During Ltp in Developing Rat Hippocampal Slices. *Neuron* **35**, 535-545 (2002).
- 57 Noguchi, J., Matsuzaki, M., Ellis-Davies, G. C. & Kasai, H. Spine-Neck Geometry Determines Nmda Receptor-Dependent Ca²⁺ Signaling in Dendrites. *Neuron* **46**, 609-622 (2005).
- 58 Bloodgood, B. L. & Sabatini, B. L. Neuronal Activity Regulates Diffusion across the Neck of Dendritic Spines. *Science* **310**, 866-869 (2005).
- 59 Gray, N. W., Weimer, R. M., Bureau, I. & Svoboda, K. Rapid Redistribution of Synaptic Psd-95 in the Neocortex *in vivo*. *PLoS biology* **4**, e370 (2006).
- 60 Calabrese, B., Wilson, M. S. & Halpain, S. Development and Regulation of Dendritic Spine Synapses. *Physiology* **21**, 38-47 (2006).

- 61 Zuo, Y., Lin, A., Chang, P. & Gan, W.-B. Development of Long-Term Dendritic Spine Stability in Diverse Regions of Cerebral Cortex. *Neuron* **46**, 181-189 (2005).
- 62 Holtmaat, A. J. *et al.* Transient and Persistent Dendritic Spines in the Neocortex *in vivo*. *Neuron* **45**, 279-291 (2005).
- 63 Matsuzaki, M. *et al.* Dendritic Spine Geometry Is Critical for Ampa Receptor Expression in Hippocampal Ca1 Pyramidal Neurons. *Nature neuroscience* **4**, 1086-1092 (2001).
- 64 Ashby, M. C., Maier, S. R., Nishimune, A. & Henley, J. M. Lateral Diffusion Drives Constitutive Exchange of Ampa Receptors at Dendritic Spines and Is Regulated by Spine Morphology. *Journal of Neuroscience* **26**, 7046-7055 (2006).
- 65 Spacek, J. & Harris, K. M. Three-Dimensional Organization of Smooth Endoplasmic Reticulum in Hippocampal Ca1 Dendrites and Dendritic Spines of the Immature and Mature Rat. *Journal of Neuroscience* **17**, 190-203 (1997).
- 66 Witcher, M. R., Kirov, S. A. & Harris, K. M. Plasticity of Perisynaptic Astroglia During Synaptogenesis in the Mature Rat Hippocampus. *Glia* **55**, 13-23 (2007).
- 67 Kasai, H., Matsuzaki, M., Noguchi, J., Yasumatsu, N. & Nakahara, H. Structure–Stability–Function Relationships of Dendritic Spines. *Trends in neurosciences* **26**, 360-368 (2003).
- 68 Ziv, N. E. & Smith, S. J. Evidence for a Role of Dendritic Filopodia in Synaptogenesis and Spine Formation. *Neuron* **17**, 91-102 (1996).
- 69 Dailey, M. E. & Smith, S. J. The Dynamics of Dendritic Structure in Developing Hippocampal Slices. *Journal of neuroscience* **16**, 2983-2994 (1996).
- 70 Denk, W., Strickler, J. H. & Webb, W. W. Two-Photon Laser Scanning Fluorescence Microscopy. *Science* **248**, 73-76 (1990).
- 71 Feng, G. *et al.* Imaging Neuronal Subsets in Transgenic Mice Expressing Multiple Spectral Variants of Gfp. *Neuron* **28**, 41-51 (2000).
- 72 Bonhoeffer, T. & Yuste, R. Spine Motility: Phenomenology, Mechanisms, and Function. *Neuron* **35**, 1019-1027 (2002).
- 73 Matsuzaki, M., Honkura, N., Ellis-Davies, G. C. & Kasai, H. Structural Basis of Long-Term Potentiation in Single Dendritic Spines. *Nature* **429**, 761-766 (2004).
- 74 Tolia, K. F. *et al.* The Rac1 Guanine Nucleotide Exchange Factor Tiam1 Mediates Ephb Receptor-Dependent Dendritic Spine Development. *Proceedings of the National Academy of Sciences* **104**, 7265-7270 (2007).
- 75 Holtmaat, A. & Svoboda, K. Experience-Dependent Structural Synaptic Plasticity in the Mammalian Brain. *Nature Reviews Neuroscience* **10**, 647-658 (2009).

- 76 Nithianantharajah, J. & Hannan, A. J. Enriched Environments, Experience-Dependent Plasticity and Disorders of the Nervous System. *Nature Reviews Neuroscience* **7**, 697-709 (2006).
- 77 Shi, Y. *et al.* Long-Term Diazepam Treatment Enhances Microglial Spine Engulfment and Impairs Cognitive Performance Via the Mitochondrial 18 Kda Translocator Protein (Tspo). *Nature Neuroscience* **25**, 317-329 (2022).
- 78 Zou, C. *et al.* Intraneuronal A β and Extracellular A β Independently Cause Dendritic Spine Pathology in Transgenic Mouse Models of Alzheimer's Disease. *Acta neuropathologica* **129**, 909-920 (2015).
- 79 Zou, C. *et al.* Neuroinflammation Impairs Adaptive Structural Plasticity of Dendritic Spines in a Preclinical Model of Alzheimer's Disease. *Acta neuropathologica* **131**, 235-246 (2016).
- 80 Millan, M. J. *et al.* Cognitive Dysfunction in Psychiatric Disorders: Characteristics, Causes and the Quest for Improved Therapy. *Nature reviews Drug discovery* **11**, 141-168 (2012).
- 81 Ethell, I. M. & Pasquale, E. B. Molecular Mechanisms of Dendritic Spine Development and Remodeling. *Progress in neurobiology* **75**, 161-205 (2005).
- 82 Lisman, J., Cooper, K., Sehgal, M. & Silva, A. J. Memory Formation Depends on Both Synapse-Specific Modifications of Synaptic Strength and Cell-Specific Increases in Excitability. *Nature neuroscience* **21**, 309-314 (2018).
- 83 Segal, M. Dendritic Spines and Long-Term Plasticity. *Nature Reviews Neuroscience* **6**, 277-284 (2005).
- 84 McNeill, T. H., Brown, S. A., Rafols, J. A. & Shoulson, I. Atrophy of Medium Spiny I Striatal Dendrites in Advanced Parkinson's Disease. *Brain Res* **455**, 148-152 (1988).
- 85 Day, M. *et al.* Selective Elimination of Glutamatergic Synapses on Striatopallidal Neurons in Parkinson Disease Models. *Nat Neurosci* **9**, 251-259 (2006).
- 86 Zaja-Milatovic, S. *et al.* Dendritic Degeneration in Neostriatal Medium Spiny Neurons in Parkinson Disease. *Neurology* **64**, 545-547 (2005).
- 87 Winner, B. *et al.* Role of Alpha-Synuclein in Adult Neurogenesis and Neuronal Maturation in the Dentate Gyrus. *J Neurosci* **32**, 16906-16916 (2012).
- 88 Neuner, J. *et al.* Pathological Alpha-Synuclein Impairs Adult-Born Granule Cell Development and Functional Integration in the Olfactory Bulb. *Nat Commun* **5**, 3915 (2014).
- 89 Burre, J., Sharma, M. & Sudhof, T. C. Definition of a Molecular Pathway Mediating Alpha-Synuclein Neurotoxicity. *J Neurosci* **35**, 5221-5232 (2015).
- 90 Kramer, M. L. & Schulz-Schaeffer, W. J. Presynaptic Alpha-Synuclein Aggregates, Not Lewy Bodies, Cause Neurodegeneration in Dementia with Lewy Bodies. *J Neurosci* **27**, 1405-1410 (2007).

- 91 Yun, S. P. *et al.* Block of A1 Astrocyte Conversion by Microglia Is Neuroprotective in Models of Parkinson's Disease. *Nature medicine* **24**, 931-938 (2018).
- 92 Doorn, K. J. *et al.* Microglial Phenotypes and Toll-Like Receptor 2 in the Substantia Nigra and Hippocampus of Incidental Lewy Body Disease Cases and Parkinson's Disease Patients. *Acta neuropathologica communications* **2**, 1-17 (2014).
- 93 Salter, M. W. & Stevens, B. Microglia Emerge as Central Players in Brain Disease. *Nat Med* **23**, 1018-1027 (2017).
- 94 Allen, N. J. & Eroglu, C. Cell Biology of Astrocyte-Synapse Interactions. *Neuron* **96**, 697-708 (2017).
- 95 Sierra, A., Paolicelli, R. C. & Kettenmann, H. Cien Años De Microglía: Milestones in a Century of Microglial Research. *Trends in neurosciences* **42**, 778-792 (2019).
- 96 Kreutzberg, G. W. Microglia: A Sensor for Pathological Events in the Cns. *Trends Neurosci* **19**, 312-318 (1996).
- 97 Schafer, D. P. *et al.* Microglia Sculpt Postnatal Neural Circuits in an Activity and Complement-Dependent Manner. *Neuron* **74**, 691-705 (2012).
- 98 Paolicelli, R. C. *et al.* Synaptic Pruning by Microglia Is Necessary for Normal Brain Development. *science* **333**, 1456-1458 (2011).
- 99 Von Bartheld, C. S., Bahney, J. & Herculano-Houzel, S. The Search for True Numbers of Neurons and Glial Cells in the Human Brain: A Review of 150 Years of Cell Counting. *Journal of Comparative Neurology* **524**, 3865-3895 (2016).
- 100 Ginhoux, F. *et al.* Fate Mapping Analysis Reveals That Adult Microglia Derive from Primitive Macrophages. *Science* **330**, 841-845 (2010).
- 101 Li, Q. & Barres, B. A. Microglia and Macrophages in Brain Homeostasis and Disease. *Nature Reviews Immunology* **18**, 225-242 (2018).
- 102 Ajami, B., Bennett, J. L., Krieger, C., Tetzlaff, W. & Rossi, F. M. Local Self-Renewal Can Sustain Cns Microglia Maintenance and Function Throughout Adult Life. *Nature neuroscience* **10**, 1538-1543 (2007).
- 103 Elmore, M. R. *et al.* Colony-Stimulating Factor 1 Receptor Signaling Is Necessary for Microglia Viability, Unmasking a Microglia Progenitor Cell in the Adult Brain. *Neuron* **82**, 380-397 (2014).
- 104 Cheadle, L. *et al.* Sensory Experience Engages Microglia to Shape Neural Connectivity through a Non-Phagocytic Mechanism. *Neuron* **108**, 451-468. e459 (2020).
- 105 Huttenlocher, P. R. Morphometric Study of Human Cerebral Cortex Development. *Neuropsychologia* **28**, 517-527 (1990).

- 106 Kurematsu, C. *et al.* Synaptic Pruning of Murine Adult-Born Neurons by Microglia Depends on Phosphatidylserine. *Journal of Experimental Medicine* **219**, e20202304 (2022).
- 107 Tau, G. Z. & Peterson, B. S. Normal Development of Brain Circuits. *Neuropsychopharmacology* **35**, 147-168 (2010).
- 108 Silbereis, J. C., Pochareddy, S., Zhu, Y., Li, M. & Sestan, N. The Cellular and Molecular Landscapes of the Developing Human Central Nervous System. *Neuron* **89**, 248-268 (2016).
- 109 Oh, W. C., Parajuli, L. K. & Zito, K. Heterosynaptic Structural Plasticity on Local Dendritic Segments of Hippocampal Ca1 Neurons. *Cell reports* **10**, 162-169 (2015).
- 110 Chung, W.-S. *et al.* Novel Allele-Dependent Role for Apoe in Controlling the Rate of Synapse Pruning by Astrocytes. *Proceedings of the National Academy of Sciences* **113**, 10186-10191 (2016).
- 111 Ueno, M. *et al.* Layer V Cortical Neurons Require Microglial Support for Survival During Postnatal Development. *Nature neuroscience* **16**, 543-551 (2013).
- 112 Tremblay, M.-È., Lowery, R. L. & Majewska, A. K. Microglial Interactions with Synapses Are Modulated by Visual Experience. *PLoS biology* **8**, e1000527 (2010).
- 113 Filipello, F. *et al.* The Microglial Innate Immune Receptor Trem2 Is Required for Synapse Elimination and Normal Brain Connectivity. *Immunity* **48**, 979-991. e978 (2018).
- 114 Nguyen, P. T. *et al.* Microglial Remodeling of the Extracellular Matrix Promotes Synapse Plasticity. *Cell* **182**, 388-403. e315 (2020).
- 115 Parellada, E. & Gassó, P. Glutamate and Microglia Activation as a Driver of Dendritic Apoptosis: A Core Pathophysiological Mechanism to Understand Schizophrenia. *Translational psychiatry* **11**, 271 (2021).
- 116 Stevens, B. *et al.* The Classical Complement Cascade Mediates Cns Synapse Elimination. *Cell* **131**, 1164-1178 (2007).
- 117 Reshef, R. *et al.* The Role of Microglia and Their Cx3cr1 Signaling in Adult Neurogenesis in the Olfactory Bulb. *Elife* **6**, e30809 (2017).
- 118 Butler, C. A. *et al.* Microglial Phagocytosis of Neurons in Neurodegeneration, and Its Regulation. *Journal of neurochemistry* **158**, 621-639 (2021).
- 119 Beynon, S. & Walker, F. Microglial Activation in the Injured and Healthy Brain: What Are We Really Talking About? Practical and Theoretical Issues Associated with the Measurement of Changes in Microglial Morphology. *Neuroscience* **225**, 162-171 (2012).
- 120 Plescher, M. *et al.* Plaque-Dependent Morphological and Electrophysiological Heterogeneity of Microglia in an Alzheimer's Disease Mouse Model. *Glia* **66**, 1464-1480 (2018).

- 121 Hickman, S., Izzy, S., Sen, P., Morsett, L. & El Khoury, J. Microglia in Neurodegeneration. *Nature neuroscience* **21**, 1359-1369 (2018).
- 122 Hanisch, U. K. Microglia as a Source and Target of Cytokines. *Glia* **40**, 140-155 (2002).
- 123 Keren-Shaul, H. *et al.* A Unique Microglia Type Associated with Restricting Development of Alzheimer's Disease. *Cell* **169**, 1276-1290. e1217 (2017).
- 124 Bohlen, C. J., Friedman, B. A., Dejanovic, B. & Sheng, M. Microglia in Brain Development, Homeostasis, and Neurodegeneration. *Annual Review of Genetics* **53**, 263-288 (2019).
- 125 Deczkowska, A. *et al.* Disease-Associated Microglia: A Universal Immune Sensor of Neurodegeneration. *Cell* **173**, 1073-1081 (2018).
- 126 Madry, C. *et al.* Microglial Ramification, Surveillance, and Interleukin-1 β Release Are Regulated by the Two-Pore Domain K⁺ Channel Thik-1. *Neuron* **97**, 299-312. e296 (2018).
- 127 Hong, S. *et al.* Complement and Microglia Mediate Early Synapse Loss in Alzheimer Mouse Models. *Science* **352**, 712-716 (2016).
- 128 Hopperton, K., Mohammad, D., Trépanier, M., Giuliano, V. & Bazinet, R. Markers of Microglia in Post-Mortem Brain Samples from Patients with Alzheimer's Disease: A Systematic Review. *Molecular psychiatry* **23**, 177-198 (2018).
- 129 Streit, W. J. & Xue, Q.-S. Microglia in Dementia with Lewy Bodies. *Brain, behavior, and immunity* **55**, 191-201 (2016).
- 130 Sellgren, C. M. *et al.* Increased Synapse Elimination by Microglia in Schizophrenia Patient-Derived Models of Synaptic Pruning. *Nature neuroscience* **22**, 374-385 (2019).
- 131 Slavik, R. *et al.* Synthesis, Radiolabeling and Evaluation of Novel 4-Oxo-Quinoline Derivatives as Pet Tracers for Imaging Cannabinoid Type 2 Receptor. *European journal of medicinal chemistry* **92**, 554-564 (2015).
- 132 Cortes, M. *et al.* in *JOURNAL OF LABELLED COMPOUNDS & RADIOPHARMACEUTICALS*. S312-S312 (WILEY-BLACKWELL 111 RIVER ST, HOBOKEN 07030-5774, NJ USA).
- 133 Beaino, W. *et al.* Purinergic Receptors P2y12r and P2x7r: Potential Targets for Pet Imaging of Microglia Phenotypes in Multiple Sclerosis. *Journal of Neuroinflammation* **14**, 1-16 (2017).
- 134 Beaino, W., Janssen, B., Vugts, D. J., de Vries, H. E. & Windhorst, A. D. Towards Pet Imaging of the Dynamic Phenotypes of Microglia. *Clinical & Experimental Immunology* **206**, 282-300 (2021).
- 135 Edison, P. *et al.* Microglia, Amyloid, and Glucose Metabolism in Parkinson's Disease with and without Dementia. *Neuropsychopharmacology* **38**, 938-949 (2013).

- 136 Paul, S. *et al.* Building a Database for Brain 18 Kda Translocator Protein Imaged Using [11c] Pbr28 in Healthy Subjects. *Journal of Cerebral Blood Flow & Metabolism* **39**, 1138-1147 (2019).
- 137 Lacapere, J.-J. & Papadopoulos, V. Peripheral-Type Benzodiazepine Receptor: Structure and Function of a Cholesterol-Binding Protein in Steroid and Bile Acid Biosynthesis. *Steroids* **68**, 569-585 (2003).
- 138 Papadopoulos, V. *et al.* Translocator Protein (18 Kda): New Nomenclature for the Peripheral-Type Benzodiazepine Receptor Based on Its Structure and Molecular Function. *Trends in pharmacological sciences* **27**, 402-409 (2006).
- 139 Gut, P., Zweckstetter, M. & Banati, R. B. Lost in Translocation: The Functions of the 18-Kd Translocator Protein. *Trends in Endocrinology & Metabolism* **26**, 349-356 (2015).
- 140 Šileikytė, J. *et al.* Regulation of the Mitochondrial Permeability Transition Pore by the Outer Membrane Does Not Involve the Peripheral Benzodiazepine Receptor (Translocator Protein of 18 Kda (Tspo)). *Journal of Biological Chemistry* **289**, 13769-13781 (2014).
- 141 Maaser, K., Sutter, A. P. & Scherübl, H. Mechanisms of Mitochondrial Apoptosis Induced by Peripheral Benzodiazepine Receptor Ligands in Human Colorectal Cancer Cells. *Biochemical and biophysical research communications* **332**, 646-652 (2005).
- 142 Notter, T. *et al.* Neuronal Activity Increases Translocator Protein (Tspo) Levels. *Molecular psychiatry* **26**, 2025-2037 (2021).
- 143 Liu, B. *et al.* *In vivo* Detection of Age-and Disease-Related Increases in Neuroinflammation by 18f-Ge180 Tspo Micropet Imaging in Wild-Type and Alzheimer's Transgenic Mice. *Journal of Neuroscience* **35**, 15716-15730 (2015).
- 144 Banati, R. *et al.* [11c](R)-Pk11195 Positron Emission Tomography Imaging of Activated Microglia *in vivo* in Rasmussen's Encephalitis. *Neurology* **53**, 2199-2199 (1999).
- 145 Fairley, L. H. *et al.* Mitochondrial Control of Microglial Phagocytosis by the Translocator Protein and Hexokinase 2 in Alzheimer's Disease. *Proceedings of the National Academy of Sciences* **120**, e2209177120 (2023).
- 146 Milenkovic, V. M. *et al.* Crispr-Cas9 Mediated Tspo Gene Knockout Alters Respiration and Cellular Metabolism in Human Primary Microglia Cells. *International journal of molecular sciences* **20**, 3359 (2019).
- 147 Belloli, S. *et al.* Evaluation of Three Quinoline-Carboxamide Derivatives as Potential Radioligands for the *in vivo* Pet Imaging of Neurodegeneration. *Neurochemistry international* **44**, 433-440 (2004).
- 148 Pike, V. *et al.* Radioligands for Pet Studies of Central Benzodiazepine Receptors and Pk (Peripheral Benzodiazepine) Binding Sites—Current Status. *Nuclear medicine and biology* **20**, 503-525 (1993).

- 149 Parker, M. A., Bazan, H. E., Marcheselli, V., Rodriguez de Turco, E. B. & Bazan, N. G. Platelet-Activating Factor Induces Permeability Transition and Cytochrome C Release in Isolated Brain Mitochondria. *Journal of neuroscience research* **69**, 39-50 (2002).
- 150 Veiga, S., Azcoitia, I. & Garcia-Segura, L. M. Ro5-4864, a Peripheral Benzodiazepine Receptor Ligand, Reduces Reactive Gliosis and Protects Hippocampal Hilar Neurons from Kainic Acid Excitotoxicity. *Journal of neuroscience research* **80**, 129-137 (2005).
- 151 Ryu, J. K., Choi, H. B. & McLarnon, J. G. Peripheral Benzodiazepine Receptor Ligand Pk11195 Reduces Microglial Activation and Neuronal Death in Quinolinic Acid-Injected Rat Striatum. *Neurobiology of disease* **20**, 550-561 (2005).
- 152 Kita, A. *et al.* Antianxiety and Antidepressant-Like Effects of Ac-5216, a Novel Mitochondrial Benzodiazepine Receptor Ligand. *British journal of pharmacology* **142**, 1059-1072 (2004).
- 153 Scholz, R. *et al.* Targeting Translocator Protein (18 Kda)(Tspo) Dampens Pro-Inflammatory Microglia Reactivity in the Retina and Protects from Degeneration. *Journal of neuroinflammation* **12**, 1-12 (2015).
- 154 Karlstetter, M. *et al.* Translocator Protein (18 Kda)(Tspo) Is Expressed in Reactive Retinal Microglia and Modulates Microglial Inflammation and Phagocytosis. *Journal of neuroinflammation* **11**, 1-13 (2014).
- 155 Riss, J., Cloyd, J., Gates, J. & Collins, S. Benzodiazepines in Epilepsy: Pharmacology and Pharmacokinetics. *Acta neurologica scandinavica* **118**, 69-86 (2008).
- 156 Patel, J. & Marangos, P. Differential Effects of Gaba on Peripheral and Central Type Benzodiazepine Binding Sites in Brain. *Neuroscience Letters* **30**, 157-160 (1982).
- 157 Poisbeau, P., Gazzo, G. & Calvel, L. Anxiolytics Targeting Gabaa Receptors: Insights on Etifoxine. *The World Journal of Biological Psychiatry* **19**, S36-S45 (2018).
- 158 Simon-O'Brien, E., Gauthier, D., Riban, V. & Verleye, M. Etifoxine Improves Sensorimotor Deficits and Reduces Glial Activation, Neuronal Degeneration, and Neuroinflammation in a Rat Model of Traumatic Brain Injury. *Journal of neuroinflammation* **13**, 1-15 (2016).
- 159 Lacapère, J.-J. *et al.* Structural and Functional Study of Reconstituted Peripheral Benzodiazepine Receptor. *Biochemical and biophysical research communications* **284**, 536-541 (2001).
- 160 Papadopoulos, V., Liu, J. & Culty, M. Is There a Mitochondrial Signaling Complex Facilitating Cholesterol Import? *Molecular and cellular endocrinology* **265**, 59-64 (2007).

- 161 Verma, A., Nye, J. S. & Snyder, S. H. Porphyrins Are Endogenous Ligands for the Mitochondrial (Peripheral-Type) Benzodiazepine Receptor. *Proceedings of the National Academy of Sciences* **84**, 2256-2260 (1987).
- 162 Guo, Y. *et al.* Structure and Activity of Tryptophan-Rich Tsps Proteins. *Science* **347**, 551-555 (2015).
- 163 Verma, A. & Snyder, S. H. Peripheral Type Benzodiazepine Receptors. *Annual Review of Pharmacology and Toxicology* **29**, 307-322 (1989).
- 164 Fan, J., Liu, J., Culty, M. & Papadopoulos, V. Acyl-Coenzyme a Binding Domain Containing 3 (Acbd3; Pap7; Gcp60): An Emerging Signaling Molecule. *Progress in lipid research* **49**, 218-234 (2010).
- 165 Liu, J., Rone, M. B. & Papadopoulos, V. Protein-Protein Interactions Mediate Mitochondrial Cholesterol Transport and Steroid Biosynthesis. *J Biol Chem* **281**, 38879-38893 (2006).
- 166 Guidotti, A. *et al.* Isolation, Characterization, and Purification to Homogeneity of an Endogenous Polypeptide with Agonistic Action on Benzodiazepine Receptors. *Proceedings of the National Academy of Sciences* **80**, 3531-3535 (1983).
- 167 Tonon, M.-C. *et al.* Endozepines and Their Receptors: Structure, Functions and Pathophysiological Significance. *Pharmacology & therapeutics* **208**, 107386 (2020).
- 168 Papadopoulos, V., Berkovich, A., Krueger, K., Costa, E. & Guidotti, A. Diazepam Binding Inhibitor and Its Processing Products Stimulate Mitochondrial Steroid Biosynthesis Via an Interaction with Mitochondrial Benzodiazepine Receptors. *Endocrinology* **129**, 1481-1488 (1991).
- 169 Everlien, I. *et al.* Diazepam Binding Inhibitor Governs Neurogenesis of Excitatory and Inhibitory Neurons During Embryonic Development Via Gaba Signaling. *Neuron* **110**, 3139-3153. e3136 (2022).
- 170 Faergeman, N. J. *et al.* Acyl-Coa-Binding Protein, Acb1p, Is Required for Normal Vacuole Function and Ceramide Synthesis in *Saccharomyces Cerevisiae*. *Biochemical Journal* **380**, 907-918 (2004).
- 171 van der Vusse, G. J. *Lipobiology*. Vol. 33 (Gulf Professional Publishing, 2004).
- 172 Mandrup, S., Faergeman, N. & Knudsen, J. Cellular Proteins and Their Fatty Acids in Health and Disease. (2003).
- 173 Neess, D. *et al.* Epidermal Acyl-Coa-Binding Protein Is Indispensable for Systemic Energy Homeostasis. *Molecular Metabolism* **44**, 101144 (2021).
- 174 Bloksgaard, M. *et al.* The Acyl-Coa Binding Protein Is Required for Normal Epidermal Barrier Function in Mice. *Journal of lipid research* **53**, 2162-2174 (2012).

- 175 Bravo-San Pedro, J. M. *et al.* Acyl-Coa-Binding Protein Is a Lipogenic Factor That Triggers Food Intake and Obesity. *Cell Metabolism* **30**, 754-767. e759 (2019).
- 176 Freeman, M. R. & Rowitch, D. H. Evolving Concepts of Gliogenesis: A Look Way Back and Ahead to the Next 25 Years. *Neuron* **80**, 613-623 (2013).
- 177 Christopherson, K. S. *et al.* Thrombospondins Are Astrocyte-Secreted Proteins That Promote Cns Synaptogenesis. *Cell* **120**, 421-433 (2005).
- 178 Hennekinne, L., Colasse, S., Triller, A. & Renner, M. Differential Control of Thrombospondin over Synaptic Glycine and Ampa Receptors in Spinal Cord Neurons. *Journal of Neuroscience* **33**, 11432-11439 (2013).
- 179 Allen, N. J. *et al.* Astrocyte Glypicans 4 and 6 Promote Formation of Excitatory Synapses Via Glua1 Ampa Receptors. *Nature* **486**, 410-414 (2012).
- 180 Feng, Z. & Ko, C.-P. Schwann Cells Promote Synaptogenesis at the Neuromuscular Junction Via Transforming Growth Factor-B1. *Journal of Neuroscience* **28**, 9599-9609 (2008).
- 181 Diniz, L. P. *et al.* Astrocyte-Induced Synaptogenesis Is Mediated by Transforming Growth Factor B Signaling through Modulation of D-Serine Levels in Cerebral Cortex Neurons. *Journal of Biological Chemistry* **287**, 41432-41445 (2012).
- 182 Bernardinelli, Y. *et al.* Activity-Dependent Structural Plasticity of Perisynaptic Astrocytic Domains Promotes Excitatory Synapse Stability. *Current Biology* **24**, 1679-1688 (2014).
- 183 Herculano-Houzel, S. The Glia/Neuron Ratio: How It Varies Uniformly across Brain Structures and Species and What That Means for Brain Physiology and Evolution. *Glia* **62**, 1377-1391 (2014).
- 184 Rowitch, D. H. & Kriegstein, A. R. Developmental Genetics of Vertebrate Glial-Cell Specification. *Nature* **468**, 214-222 (2010).
- 185 Matyash, V. & Kettenmann, H. Heterogeneity in Astrocyte Morphology and Physiology. *Brain research reviews* **63**, 2-10 (2010).
- 186 Oberheim, N. A., Wang, X., Goldman, S. & Nedergaard, M. Astrocytic Complexity Distinguishes the Human Brain. *Trends in neurosciences* **29**, 547-553 (2006).
- 187 Gomez-Arboledas, A. *et al.* Phagocytic Clearance of Presynaptic Dystrophies by Reactive Astrocytes in Alzheimer's Disease. *Glia* **66**, 637-653 (2018).
- 188 Chapman, D., Theodosis, D., Montagnese, C., Poulain, D. & Morris, J. Osmotic Stimulation Causes Structural Plasticity of Neurone-Glia Relationships of the Oxytocin but Not Vasopressin Secreting Neurones in the Hypothalamic Supraoptic Nucleus. *Neuroscience* **17**, 679-686 (1986).
- 189 Miyata, S., Itoh, T., Matsushima, O., Nakashima, T. & Kiyohara, T. Not Only Osmotic Stress but Also Repeated Restraint Stress Causes Structural Plasticity

- in the Supraoptic Nucleus of the Rat Hypothalamus. *Brain research bulletin* **33**, 669-675 (1994).
- 190 Hart, C. G. & Karimi-Abdolrezaee, S. Recent Insights on Astrocyte Mechanisms in Cns Homeostasis, Pathology, and Repair. *Journal of neuroscience research* **99**, 2427-2462 (2021).
- 191 Vasile, F., Dossi, E. & Rouach, N. Human Astrocytes: Structure and Functions in the Healthy Brain. *Brain Structure and Function* **222**, 2017-2029 (2017).
- 192 Bonvento, G. & Bolaños, J. P. Astrocyte-Neuron Metabolic Cooperation Shapes Brain Activity. *Cell metabolism* **33**, 1546-1564 (2021).
- 193 Abbott, N. J., Rönnbäck, L. & Hansson, E. Astrocyte–Endothelial Interactions at the Blood–Brain Barrier. *Nature reviews neuroscience* **7**, 41-53 (2006).
- 194 MacVicar, B. A. & Newman, E. A. Astrocyte Regulation of Blood Flow in the Brain. *Cold Spring Harbor perspectives in biology* **7**, a020388 (2015).
- 195 Weber, B. & Barros, L. F. The Astrocyte: Powerhouse and Recycling Center. *Cold Spring Harbor perspectives in biology* **7**, a020396 (2015).
- 196 Adermark, L. *et al.* Astrocytes Modulate Extracellular Neurotransmitter Levels and Excitatory Neurotransmission in Dorsolateral Striatum Via Dopamine D2 Receptor Signaling. *Neuropsychopharmacology* **47**, 1493-1502 (2022).
- 197 Walz, W. Role of Astrocytes in the Clearance of Excess Extracellular Potassium. *Neurochemistry international* **36**, 291-300 (2000).
- 198 Chung, W.-S., Allen, N. J. & Eroglu, C. Astrocytes Control Synapse Formation, Function, and Elimination. *Cold Spring Harbor perspectives in biology* **7**, a020370 (2015).
- 199 Kıray, H., Lindsay, S. L., Hosseinzadeh, S. & Barnett, S. C. The Multifaceted Role of Astrocytes in Regulating Myelination. *Experimental neurology* **283**, 541-549 (2016).
- 200 Dong, Y. & Benveniste, E. N. Immune Function of Astrocytes. *Glia* **36**, 180-190 (2001).
- 201 Colombo, E. & Farina, C. Astrocytes: Key Regulators of Neuroinflammation. *Trends in immunology* **37**, 608-620 (2016).
- 202 Cajal, S. R. *Histologie Du Systeme Me Nerveux De l'homme Et Des Verte Be S. Maloine (Paris)* **2**, 891-942 (1911).
- 203 Sofroniew, M. V. & Vinters, H. V. Astrocytes: Biology and Pathology. *Acta neuropathologica* **119**, 7-35 (2010).
- 204 Oberheim, N. A. *et al.* Uniquely Hominid Features of Adult Human Astrocytes. *Journal of Neuroscience* **29**, 3276-3287 (2009).
- 205 Batiuk, M. Y. *et al.* Identification of Region-Specific Astrocyte Subtypes at Single Cell Resolution. *Nature communications* **11**, 1220 (2020).

- 206 Werkman, I. L. *et al.* Transcriptional Heterogeneity between Primary Adult Grey and White Matter Astrocytes Underlie Differences in Modulation of in Vitro Myelination. *Journal of neuroinflammation* **17**, 1-18 (2020).
- 207 MacVicar, B. Voltage-Dependent Calcium Channels in Glial Cells. *Science* **226**, 1345-1347 (1984).
- 208 Emsley, J. G. & Macklis, J. D. Astroglial Heterogeneity Closely Reflects the Neuronal-Defined Anatomy of the Adult Murine Cns. *Neuron glia biology* **2**, 175-186 (2006).
- 209 Eroglu, C., Barres, B. A. & Stevens, B. Glia as Active Participants in the Development and Function of Synapses. *Structural and functional organization of the synapse*, 683-714 (2008).
- 210 Farhy-Tselnicker, I. & Allen, N. J. Astrocytes, Neurons, Synapses: A Tripartite View on Cortical Circuit Development. *Neural development* **13**, 1-12 (2018).
- 211 Haber, M. & Murai, K. K. Reshaping Neuron–Glial Communication at Hippocampal Synapses. *Neuron glia biology* **2**, 59-66 (2006).
- 212 DeFelipe, J., Alonso-Nanclares, L. & Arellano, J. I. Microstructure of the Neocortex: Comparative Aspects. *Journal of neurocytology* **31**, 299-316 (2002).
- 213 Verkhratsky, A., Matteoli, M., Parpura, V., Mothet, J. P. & Zorec, R. Astrocytes as Secretory Cells of the Central Nervous System: Idiosyncrasies of Vesicular Secretion. *The EMBO journal* **35**, 239-257 (2016).
- 214 Laviaille, M. *et al.* Structural Plasticity of Perisynaptic Astrocyte Processes Involves Ezrin and Metabotropic Glutamate Receptors. *Proceedings of the National Academy of Sciences* **108**, 12915-12919 (2011).
- 215 Pfrieger, F. W. & Barres, B. A. Synaptic Efficacy Enhanced by Glial Cells in Vitro. *Science* **277**, 1684-1687 (1997).
- 216 Ullian, E. M., Sapperstein, S. K., Christopherson, K. S. & Barres, B. A. Control of Synapse Number by Glia. *science* **291**, 657-661 (2001).
- 217 Cao, G. & Ko, C.-P. Schwann Cell-Derived Factors Modulate Synaptic Activities at Developing Neuromuscular Synapses. *Journal of Neuroscience* **27**, 6712-6722 (2007).
- 218 Reddy, L. V., Koirala, S., Sugiura, Y., Herrera, A. A. & Ko, C.-P. Glial Cells Maintain Synaptic Structure and Function and Promote Development of the Neuromuscular Junction *in vivo*. *Neuron* **40**, 563-580 (2003).
- 219 Cuevas, M. E. *et al.* The Presence of Glia Stimulates the Appearance of Glycinergic Synaptic Transmission in Spinal Cord Neurons. *Molecular and Cellular Neuroscience* **28**, 770-778 (2005).
- 220 Elmariah, S. B., Oh, E. J., Hughes, E. G. & Balice-Gordon, R. J. Astrocytes Regulate Inhibitory Synapse Formation Via Trk-Mediated Modulation of Postsynaptic Gabaa Receptors. *Journal of Neuroscience* **25**, 3638-3650 (2005).

- 221 Boué-Grabot, E. & Pankratov, Y. Modulation of Central Synapses by Astrocyte-Released Atp and Postsynaptic P2x Receptors. *Neural plasticity* **2017** (2017).
- 222 Koizumi, S., Fujishita, K., Tsuda, M., Shigemoto-Mogami, Y. & Inoue, K. Dynamic Inhibition of Excitatory Synaptic Transmission by Astrocyte-Derived Atp in Hippocampal Cultures. *Proceedings of the National Academy of Sciences* **100**, 11023-11028 (2003).
- 223 Ota, Y., Zanetti, A. T. & Hallock, R. M. The Role of Astrocytes in the Regulation of Synaptic Plasticity and Memory Formation. *Neural plasticity* **2013** (2013).
- 224 Santello, M. & Volterra, A. Synaptic Modulation by Astrocytes Via Ca²⁺-Dependent Glutamate Release. *Neuroscience* **158**, 253-259 (2009).
- 225 Bonansco, C. *et al.* Glutamate Released Spontaneously from Astrocytes Sets the Threshold for Synaptic Plasticity. *European Journal of Neuroscience* **33**, 1483-1492 (2011).
- 226 Yang, J. *et al.* Glutamate-Releasing Swell1 Channel in Astrocytes Modulates Synaptic Transmission and Promotes Brain Damage in Stroke. *Neuron* **102**, 813-827. e816 (2019).
- 227 Kucukdereli, H. *et al.* Control of Excitatory Cns Synaptogenesis by Astrocyte-Secreted Proteins Hevin and Sparc. *Proceedings of the National Academy of Sciences* **108**, E440-E449 (2011).
- 228 Singh, S. K. *et al.* Astrocytes Assemble Thalamocortical Synapses by Bridging Nrx1 α and Nl1 Via Hevin. *Cell* **164**, 183-196 (2016).
- 229 Stellwagen, D. & Malenka, R. C. Synaptic Scaling Mediated by Glial Tnf- α . *Nature* **440**, 1054-1059 (2006).
- 230 Vainchtein, I. D. *et al.* Astrocyte-Derived Interleukin-33 Promotes Microglial Synapse Engulfment and Neural Circuit Development. *Science* **359**, 1269-1273 (2018).
- 231 McAlpine, C. S. *et al.* Astrocytic Interleukin-3 Programs Microglia and Limits Alzheimer's Disease. *Nature* **595**, 701-706 (2021).
- 232 Lian, H. *et al.* Astrocyte-Microglia Cross Talk through Complement Activation Modulates Amyloid Pathology in Mouse Models of Alzheimer's Disease. *Journal of Neuroscience* **36**, 577-589 (2016).
- 233 Liddelow, S. A. *et al.* Neurotoxic Reactive Astrocytes Are Induced by Activated Microglia. *Nature* **541**, 481-487 (2017).
- 234 Shankar, G. M. & Walsh, D. M. Alzheimer's Disease: Synaptic Dysfunction and A β . *Molecular neurodegeneration* **4**, 1-13 (2009).
- 235 Lafon-Cazal, M. *et al.* Proteomic Analysis of Astrocytic Secretion in the Mouse: Comparison with the Cerebrospinal Fluid Proteome. *Journal of Biological Chemistry* **278**, 24438-24448 (2003).

- 236 Tonon, M., Désy, L., Nicolas, P., Vaudry, H. & Pelletier, G. Immunocytochemical Localization of the Endogenous Benzodiazepine Ligand Octadecaneuropeptide (Odn) in the Rat Brain. *Neuropeptides* **15**, 17-24 (1990).
- 237 Vidnyánszky, Z., Görcs, T. J. & Hámori, J. Diazepam Binding Inhibitor Fragment 33–50 (Octadecaneuropeptide) Immunoreactivity in the Cerebellar Cortex Is Restricted to Glial Cells. *Glia* **10**, 132-141 (1994).
- 238 Tong, Y., Toranzo, D. & Pelletier, G. Localization of Diazepam-Binding Inhibitor (Dbi) Mrna in the Rat Brain by High Resolution in Situ Hybridization. *Neuropeptides* **20**, 33-40 (1991).
- 239 Lamacz, M. *et al.* The Endogenous Benzodiazepine Receptor Ligand Odn Increases Cytosolic Calcium in Cultured Rat Astrocytes. *Molecular brain research* **37**, 290-296 (1996).
- 240 Duran, J. M., Anjard, C., Stefan, C., Loomis, W. F. & Malhotra, V. Unconventional Secretion of Acb1 Is Mediated by Autophagosomes. *Journal of cell biology* **188**, 527-536 (2010).
- 241 Lebrun, B. *et al.* Glial Endozepines and Energy Balance: Old Peptides with New Tricks. *Glia* **69**, 1079-1093 (2021).
- 242 Anjard, C. & Loomis, W. F. Peptide Signaling During Terminal Differentiation of Dictyostelium. *Proceedings of the National Academy of Sciences* **102**, 7607-7611 (2005).
- 243 Manjithaya, R., Anjard, C., Loomis, W. F. & Subramani, S. Unconventional Secretion of Pichia Pastoris Acb1 Is Dependent on Grasp Protein, Peroxisomal Functions, and Autophagosome Formation. *Journal of Cell Biology* **188**, 537-546 (2010).
- 244 Bouyakdan, K. *et al.* The Gliotransmitter Acbp Controls Feeding and Energy Homeostasis Via the Melanocortin System. *The Journal of clinical investigation* **129**, 2417-2430 (2019).
- 245 Loomis, W. F., Behrens, M. M., Williams, M. E. & Anjard, C. Pregnenolone Sulfate and Cortisol Induce Secretion of Acyl-Coa-Binding Protein and Its Conversion into Endozepines from Astrocytes. *Journal of Biological Chemistry* **285**, 21359-21365 (2010).
- 246 Brady, S., Siegel, G., Albers, R. W. & Price, D. L. *Basic Neurochemistry: Molecular, Cellular and Medical Aspects*. (Elsevier, 2005).
- 247 Hökfelt, T., Bartfai, T. & Bloom, F. Neuropeptides: Opportunities for Drug Discovery. *The Lancet Neurology* **2**, 463-472 (2003).
- 248 Udupa, P., Kumar, A., Parit, R. & Ghosh, D. K. Acyl-Coa Binding Protein Regulates Nutrient-Dependent Autophagy. *Metabolism*, 155338 (2022).
- 249 Martineau, M. *et al.* Storage and Uptake of D-Serine into Astrocytic Synaptic-Like Vesicles Specify Gliotransmission. *Journal of Neuroscience* **33**, 3413-3423 (2013).

- 250 Lanfray, D. *et al.* Gliotransmission and Brain Glucose Sensing: Critical Role of Endozepines. *Diabetes* **62**, 801-810 (2013).
- 251 Masmoudi, O. *et al.* Pituitary Adenylate Cyclase-Activating Polypeptide (Pacap) Stimulates Endozepine Release from Cultured Rat Astrocytes Via a Pka-Dependent Mechanism. *The FASEB journal* **17**, 17-27 (2003).
- 252 Masmoudi, O. *et al.* Somatostatin Down-Regulates the Expression and Release of Endozepines from Cultured Rat Astrocytes Via Distinct Receptor Subtypes. *Journal of neurochemistry* **94**, 561-571 (2005).
- 253 Tokay, T. *et al.* Beta-Amyloid Peptide Stimulates Endozepine Release in Cultured Rat Astrocytes through Activation of N-Formyl Peptide Receptors. *Glia* **56**, 1380-1389 (2008).
- 254 Charmpilas, N. *et al.* Acyl-Coa-Binding Protein (Acbp): A Phylogenetically Conserved Appetite Stimulator. *Cell Death & Disease* **11**, 7 (2020).
- 255 Christian, C. A. *et al.* Endogenous Positive Allosteric Modulation of Gabaa Receptors by Diazepam Binding Inhibitor. *Neuron* **78**, 1063-1074 (2013).
- 256 Knudsen, J. *et al.* Yeast Acyl-Coa-Binding Protein: Acyl-Coa-Binding Affinity and Effect on Intracellular Acyl-Coa Pool Size. *Biochemical Journal* **302**, 479-485 (1994).
- 257 Mogensen, I., Schulenberg, H., Hansen, H., Spener, F. & Knudsen, J. A Novel Acyl-Coa-Binding Protein from Bovine Liver. Effect on Fatty Acid Synthesis. *Biochemical Journal* **241**, 189 (1987).
- 258 Ferrero, P. *et al.* Diazepam Binding Inhibitor-Like Immunoreactivity (Dbi-Li) in Human Csf: Correlations with Neurological Disorders. *Journal of the neurological sciences* **87**, 327-349 (1988).
- 259 Conti, E. *et al.* Serum Dbi and Biomarkers of Neuroinflammation in Alzheimer's Disease and Delirium. *Neurological Sciences* **42**, 1003-1007 (2021).
- 260 Ferrarese, C. *et al.* Diazepam Binding Inhibitor (Dbi) Increases after Acute Stress in Rat. *Neuropharmacology* **30**, 1445-1452 (1991).
- 261 Katsura, M. *et al.* Psychological Stress, but Not Physical Stress, Causes Increase in Diazepam Binding Inhibitor (Dbi) Mrna Expression in Mouse Brains. *Molecular brain research* **104**, 103-109 (2002).
- 262 Pichitpunpong, C. *et al.* Phenotypic Subgrouping and Multi-Omics Analyses Reveal Reduced Diazepam-Binding Inhibitor (Dbi) Protein Levels in Autism Spectrum Disorder with Severe Language Impairment. *PLoS One* **14**, e0214198 (2019).
- 263 Kaiser, W. & Garrett, C. Two-Photon Excitation in Ca F 2: Eu 2+. *Physical review letters* **7**, 229 (1961).
- 264 Lichtman, J. W. & Conchello, J.-A. Fluorescence Microscopy. *Nature methods* **2**, 910-919 (2005).

- 265 Ash, C., Dubec, M., Donne, K. & Bashford, T. Effect of Wavelength and Beam Width on Penetration in Light-Tissue Interaction Using Computational Methods. *Lasers in medical science* **32**, 1909-1918 (2017).
- 266 Helmchen, F. & Denk, W. Deep Tissue Two-Photon Microscopy. *Nature methods* **2**, 932-940 (2005).
- 267 Spiess, E. *et al.* Two-Photon Excitation and Emission Spectra of the Green Fluorescent Protein Variants Ecfp, Egfp and Eyfp. *Journal of Microscopy* **217**, 200-204 (2005).
- 268 Wallace, M. Locus of the Gene 'Fidget' in the House Mouse. *Nature* **166**, 407-407 (1950).
- 269 Masliah, E. *et al.* Dopaminergic Loss and Inclusion Body Formation in A-Synuclein Mice: Implications for Neurodegenerative Disorders. *Science* **287**, 1265-1269 (2000).
- 270 Banati, R. B. *et al.* Positron Emission Tomography and Functional Characterization of a Complete Pbr/Tspo Knockout. *Nature communications* **5**, 1-12 (2014).
- 271 Fredriksson, S. *et al.* Protein Detection Using Proximity-Dependent DNA Ligation Assays. *Nature biotechnology* **20**, 473-477 (2002).
- 272 Weiler, I. Synaptosomes. (2009).
- 273 Fuhrmann, M., Mitteregger, G., Kretzschmar, H. & Herms, J. Dendritic Pathology in Prion Disease Starts at the Synaptic Spine. *Journal of Neuroscience* **27**, 6224-6233 (2007).
- 274 Amschl, D. *et al.* Time Course and Progression of Wild Type A-Synuclein Accumulation in a Transgenic Mouse Model. *BMC neuroscience* **14**, 1-14 (2013).
- 275 Guilarte, T. R., Rodichkin, A. N., McGlothan, J. L., De La Rocha, A. M. A. & Azzam, D. J. Imaging Neuroinflammation with Tspo: A New Perspective on the Cellular Sources and Subcellular Localization. *Pharmacology & therapeutics*, 108048 (2021).
- 276 Hendrickx, D. A., van Eden, C. G., Schuurman, K. G., Hamann, J. & Huitinga, I. Staining of Hla-Dr, Iba1 and Cd68 in Human Microglia Reveals Partially Overlapping Expression Depending on Cellular Morphology and Pathology. *Journal of neuroimmunology* **309**, 12-22 (2017).
- 277 Patt, S., Gertz, H. J., Gerhard, L. & Cervos-Navarro, J. Pathological Changes in Dendrites of Substantia Nigra Neurons in Parkinson's Disease: A Golgi Study. *Histol Histopathol* **6**, 373-380 (1991).
- 278 Chitu, V., Gokhan, Ş., Nandi, S., Mehler, M. F. & Stanley, E. R. Emerging Roles for Csf-1 Receptor and Its Ligands in the Nervous System. *Trends in neurosciences* **39**, 378-393 (2016).

- 279 Spangenberg, E. *et al.* Sustained Microglial Depletion with Csf1r Inhibitor Impairs Parenchymal Plaque Development in an Alzheimer's Disease Model. *Nature communications* **10**, 3758 (2019).
- 280 Miyagishi, M. & Taira, K. U6 Promoter-Driven Sirnas with Four Uridine 3' Overhangs Efficiently Suppress Targeted Gene Expression in Mammalian Cells. *Nature biotechnology* **20**, 497-500 (2002).
- 281 Ge, S. *et al.* Gaba Regulates Synaptic Integration of Newly Generated Neurons in the Adult Brain. *Nature* **439**, 589-593 (2006).
- 282 Focke, C. *et al.* Early and Longitudinal Microglial Activation but Not Amyloid Accumulation Predicts Cognitive Outcome in Ps2app Mice. *Journal of nuclear medicine* **60**, 548-554 (2019).
- 283 Frison, M. *et al.* The Translocator Protein (Tspo) Is Prodromal to Mitophagy Loss in Neurotoxicity. *Molecular Psychiatry* **26**, 2721-2739 (2021).
- 284 Ross, R. A., Spengler, B. A. & Biedler, J. L. Coordinate Morphological and Biochemical Interconversion of Human Neuroblastoma Cells. *Journal of the National Cancer Institute* **71**, 741-747 (1983).
- 285 Krueger, K. E. & Papadopoulos, V. Peripheral-Type Benzodiazepine Receptors Mediate Translocation of Cholesterol from Outer to Inner Mitochondrial Membranes in Adrenocortical Cells. *Journal of Biological Chemistry* **265**, 15015-15022 (1990).
- 286 Owen, D. R. *et al.* Tspo Mutations in Rats and a Human Polymorphism Impair the Rate of Steroid Synthesis. *Biochemical Journal* **474**, 3985-3999 (2017).
- 287 Chelli, B. *et al.* Peripheral-Type Benzodiazepine Receptor Ligands:: Mitochondrial Permeability Transition Induction in Rat Cardiac Tissue. *Biochemical pharmacology* **61**, 695-705 (2001).
- 288 Repalli, J. Translocator Protein (Tspo) Role in Aging and Alzheimer's Disease. *Current aging science* **7**, 168-175 (2014).
- 289 Magri, A. *et al.* Erk1/2-Dependent Tspo Overactivation Associates with the Loss of Mitophagy and Mitochondrial Respiration in Als. *Cell Death & Disease* **14**, 122 (2023).
- 290 Banati, R., Myers, R. & Kreutzberg, G. Pk ('Peripheral Benzodiazepine')-Binding Sites in the Cns Indicate Early and Discrete Brain Lesions: Microautoradiographic Detection of [3h] Pk 11195 Binding to Activated Microglia. *Journal of neurocytology* **26**, 77-82 (1997).
- 291 Cagnin, A. *et al.* In-Vivo Measurement of Activated Microglia in Dementia. *The Lancet* **358**, 461-467 (2001).
- 292 Kreisl, W. C. *et al.* In vivo Radioligand Binding to Translocator Protein Correlates with Severity of Alzheimer's Disease. *Brain* **136**, 2228-2238 (2013).

- 293 Suridjan, I. *et al.* In-Vivo Imaging of Grey and White Matter Neuroinflammation in Alzheimer's Disease: A Positron Emission Tomography Study with a Novel Radioligand, [18f]-Feppa. *Molecular psychiatry* **20**, 1579-1587 (2015).
- 294 Dodel, R. *et al.* Minocycline 1-Year Therapy in Multiple-System-Atrophy: Effect on Clinical Symptoms and [11c](R)-Pk11195 Pet (Mensa-Trial). *Movement Disorders* **25**, 97-107 (2010).
- 295 Kobylecki, C. *et al.* Diffusion-Weighted Imaging and Its Relationship to Microglial Activation in Parkinsonian Syndromes. *Parkinsonism & related disorders* **19**, 527-532 (2013).
- 296 Gerhard, A. *et al.* In vivo Imaging of Microglial Activation with [11c](R)-Pk11195 Pet in Corticobasal Degeneration. *Movement disorders: official journal of the Movement Disorder Society* **19**, 1221-1226 (2004).
- 297 Henkel, K. *et al.* Imaging of Activated Microglia with Pet and [11c] Pk 11195 in Corticobasal Degeneration. *Movement disorders* **19**, 817-821 (2004).
- 298 Cagnin, A., Rossor, M., Sampson, E. L., MacKinnon, T. & Banati, R. B. In vivo Detection of Microglial Activation in Frontotemporal Dementia. *Annals of Neurology: Official Journal of the American Neurological Association and the Child Neurology Society* **56**, 894-897 (2004).
- 299 Miyoshi, M. *et al.* In vivo Detection of Neuropathologic Changes in Presymptomatic Mapt Mutation Carriers: A Pet and Mri Study. *Parkinsonism & related disorders* **16**, 404-408 (2010).
- 300 Turner, M. *et al.* Evidence of Widespread Cerebral Microglial Activation in Amyotrophic Lateral Sclerosis: An [11c](R)-Pk11195 Positron Emission Tomography Study. *Neurobiology of disease* **15**, 601-609 (2004).
- 301 Haarman, B. C. B. *et al.* Neuroinflammation in Bipolar Disorder—a [11c](R)-Pk11195 Positron Emission Tomography Study. *Brain, behavior, and immunity* **40**, 219-225 (2014).
- 302 Setiawan, E. *et al.* Role of Translocator Protein Density, a Marker of Neuroinflammation, in the Brain During Major Depressive Episodes. *JAMA psychiatry* **72**, 268-275 (2015).
- 303 Van Berckel, B. N. *et al.* Microglia Activation in Recent-Onset Schizophrenia: A Quantitative (R)-[11c] Pk11195 Positron Emission Tomography Study. *Biological psychiatry* **64**, 820-822 (2008).
- 304 Zürcher, N. *et al.* [11c] Pbr28 Mr–Pet Imaging Reveals Lower Regional Brain Expression of Translocator Protein (Tspo) in Young Adult Males with Autism Spectrum Disorder. *Molecular Psychiatry* **26**, 1659-1669 (2021).
- 305 Li, Q. & Barres, B. A. Microglia and Macrophages in Brain Homeostasis and Disease. *Nat Rev Immunol* **18**, 225-242 (2018).
- 306 Salter, M. W. & Stevens, B. Microglia Emerge as Central Players in Brain Disease. *Nature medicine* **23**, 1018-1027 (2017).

- 307 Grubman, A. *et al.* Transcriptional Signature in Microglia Associated with A β Plaque Phagocytosis. *Nature communications* **12**, 3015 (2021).
- 308 Rothstein, J. D. *et al.* Cerebrospinal Fluid Content of Diazepam Binding Inhibitor in Chronic Hepatic Encephalopathy. *Annals of Neurology: Official Journal of the American Neurological Association and the Child Neurology Society* **26**, 57-62 (1989).
- 309 Aramideh, J. A., Vidal-Itriago, A., Morsch, M. & Graeber, M. B. Cytokine Signalling at the Microglial Penta-Partite Synapse. *International Journal of Molecular Sciences* **22**, 13186 (2021).
- 310 Blinzinger, K. & Kreutzberg, G. Displacement of Synaptic Terminals from Regenerating Motoneurons by Microglial Cells. *Zeitschrift für Zellforschung und mikroskopische Anatomie* **85**, 145-157 (1968).
- 311 Araque, A., Parpura, V., Sanzgiri, R. P. & Haydon, P. G. Tripartite Synapses: Glia, the Unacknowledged Partner. *Trends in neurosciences* **22**, 208-215 (1999).
- 312 Chung, W.-S. *et al.* Astrocytes Mediate Synapse Elimination through Megf10 and Mertk Pathways. *Nature* **504**, 394-400 (2013).
- 313 Clarke, L. E. *et al.* Normal Aging Induces A1-Like Astrocyte Reactivity. *Proceedings of the National Academy of Sciences* **115**, E1896-E1905 (2018).
- 314 Frantz, C., Stewart, K. M. & Weaver, V. M. The Extracellular Matrix at a Glance. *Journal of cell science* **123**, 4195-4200 (2010).
- 315 Nicholson, C. & Syková, E. Extracellular Space Structure Revealed by Diffusion Analysis. *Trends in neurosciences* **21**, 207-215 (1998).
- 316 Sellers, D. L., Maris, D. O. & Horner, P. J. Postinjury Niches Induce Temporal Shifts in Progenitor Fates to Direct Lesion Repair after Spinal Cord Injury. *Journal of Neuroscience* **29**, 6722-6733 (2009).
- 317 Badylak, S. F. in *Seminars in cell & developmental biology*. 377-383 (Elsevier).
- 318 Dityatev, A., Seidenbecher, C. I. & Schachner, M. Compartmentalization from the Outside: The Extracellular Matrix and Functional Microdomains in the Brain. *Trends in neurosciences* **33**, 503-512 (2010).
- 319 Hrabětová, S., Masri, D., Tao, L., Xiao, F. & Nicholson, C. Calcium Diffusion Enhanced after Cleavage of Negatively Charged Components of Brain Extracellular Matrix by Chondroitinase Abc. *The Journal of physiology* **587**, 4029-4049 (2009).
- 320 Morawski, M. *et al.* Ion Exchanger in the Brain: Quantitative Analysis of Perineuronally Fixed Anionic Binding Sites Suggests Diffusion Barriers with Ion Sorting Properties. *Scientific reports* **5**, 16471 (2015).
- 321 Bekku, Y. *et al.* Bral1: Its Role in Diffusion Barrier Formation and Conduction Velocity in the Cns. *Journal of Neuroscience* **30**, 3113-3123 (2010).

- 322 Frischknecht, R. *et al.* Brain Extracellular Matrix Affects Ampa Receptor Lateral Mobility and Short-Term Synaptic Plasticity. *Nature neuroscience* **12**, 897-904 (2009).
- 323 Groc, L. *et al.* Nmda Receptor Surface Trafficking and Synaptic Subunit Composition Are Developmentally Regulated by the Extracellular Matrix Protein Reelin. *Journal of Neuroscience* **27**, 10165-10175 (2007).
- 324 Nash, B. *et al.* Functional Duality of Astrocytes in Myelination. *Journal of Neuroscience* **31**, 13028-13038 (2011).
- 325 Harlow, D. E. & Macklin, W. B. Inhibitors of Myelination: Ecm Changes, Cspgs and Ptps. *Experimental neurology* **251**, 39-46 (2014).
- 326 Crapser, J. D. *et al.* Microglia Facilitate Loss of Perineuronal Nets in the Alzheimer's Disease Brain. *EBioMedicine* **58**, 102919 (2020).
- 327 Cattaud, V. *et al.* Early Disruption of Parvalbumin Expression and Perineuronal Nets in the Hippocampus of the Tg2576 Mouse Model of Alzheimer's Disease Can Be Rescued by Enriched Environment. *Neurobiology of aging* **72**, 147-158 (2018).
- 328 Gray, E., Thomas, T. L., Betmouni, S., Scolding, N. & Love, S. Elevated Matrix Metalloproteinase-9 and Degradation of Perineuronal Nets in Cerebrocortical Multiple Sclerosis Plaques. *Journal of Neuropathology & Experimental Neurology* **67**, 888-899 (2008).
- 329 Crapser, J. D. *et al.* Microglial Depletion Prevents Extracellular Matrix Changes and Striatal Volume Reduction in a Model of Huntington's Disease. *Brain* **143**, 266-288 (2020).
- 330 Pantazopoulos, H., Woo, T.-U. W., Lim, M. P., Lange, N. & Berretta, S. Extracellular Matrix-Glial Abnormalities in the Amygdala and Entorhinal Cortex of Subjects Diagnosed with Schizophrenia. *Archives of general psychiatry* **67**, 155-166 (2010).
- 331 Mauney, S. A. *et al.* Developmental Pattern of Perineuronal Nets in the Human Prefrontal Cortex and Their Deficit in Schizophrenia. *Biological psychiatry* **74**, 427-435 (2013).
- 332 Oshry, B. *Seeing Systems: Unlocking the Mysteries of Organizational Life.* (Berrett-Koehler Publishers, 2007).
- 333 Auyang, S. Y. *Foundations of Complex-System Theories: In Economics, Evolutionary Biology, and Statistical Physics.* (Cambridge University Press, 1998).

Abbreviations

°C	Degree Celsius
%	Percentage
2D	Two-dimensional
3D	Three-dimensional
A	Ampere
AAV	Adeno-associated virus
ACBD1	Acyl-coenzyme A binding domain-containing protein 1
ACBD3	Acyl-coenzyme A binding domain-containing protein 3
ACBP	Acyl-coenzyme A binding protein
AD	Alzheimer's disease
AMPA	α -amino-3-hydroxy-5-methyl-4-isoxazole propionic acid
ANF	Atipamezole, naloxone, and flumazenil
ANOVA	Analysis of variance
ASD	Autistic spectrum disorder
ATP	Adenosine triphosphate
A β	Amyloid-beta
BBB	Blood-brain barrier
BCA	Bicinchoninic acid
bp	Base pair
C1q	Complement component 1q
C3	Complement component 3
Ca ²⁺	Calcium ion
Cat#	Categorical number
CB2	Cannabinoid receptor type 2
CD68	Cluster of differentiation 68

CICR	Ca ²⁺ -induced Ca ²⁺ release
CNS	Central nervous system
COX-2	Cyclooxygenase-2
CR3	Complement receptor 3
CSF-1R	Colony-stimulating factor 1 receptor
CX3CR1	C-X3-C motif chemokine receptor 1
DAM	Disease-associated microglia
DBI	Diazepam binding inhibitor
DIV	Day <i>in vitro</i>
DLB	Dementia with Lewy bodies
DMSO	Dimethyl sulfoxide
DNA	Deoxyribonucleic acid
DTT	Dithiothreitol
<i>e.g.</i>	<i>Exempli gratia</i> ; for example
ECF	Extracellular fluid
eCFP	Enhance cyan fluorescent protein
ECL	Enhanced chemiluminescence
ECM	Extracellular matrix
eGFP	Enhanced green fluorescent protein
ELISA	Enzyme-linked immunosorbent assay
<i>et al.</i>	<i>Et alii</i> ; And others
eYFP	Enhanced yellow fluorescent protein
FBS	Fetal bovine serum
FFPE	Formalin-fixed paraffin-embedded
Fig.	Figure
GABA	γ-aminobutyric acid
GABA _A R	γ-aminobutyric acid type A receptor

GC	Genome copies
GDNF	Glial cell line-derived neurotrophic factor
GFAP	Glial fibrillary acidic protein
GM-CSF	Granulocyte-macrophage colony-stimulating factor
GRASP	Golgi reassembly stacking protein
h	Hour
HEPES	4-(2-Hydroxyethyl) piperazine-1-ethane sulfonic acid
HRP	Horseradish peroxidase
Iba1	Ionized calcium binding adaptor molecule 1
ICC	International consensus criteria
ID	Identifier
IL-1 β	Interleukin-1 β
IL-3	Interleukin-3
IL-33	Interleukin-33
IL-3R α	Interleukin-3 receptor α
IL-6	Interleukin-6
kDa	Kilodalton
kg	Kilogram
LBD	Lewy body dementia
LCACoA	Long-chain acyl-coenzyme A
M	Molar
mg	Milligram
MGI	Mouse genome informatics
MHC II	Major histocompatibility complex class II
min	Minute
mL	Milliliter
mm	Millimeter

mM	Millimolar
mm ³	Cubic millimeter
MMF	Midazolam, medetomidine, and fentanyl
N/A	Not applicable
ng	Nanogram
nm	Nanometer
nM	Nanomolar
NOS	Nitric oxide synthase
OD	Optical density
<i>p</i>	Probability value; p-value
PAP7	PBR-associated protein 7
PBR	Peripheral-type benzodiazepine receptor
PBS	Phosphate-buffered saline
PCR	Polymerase chain reaction
PCSK1	Proprotein convertase subtilisin/kexin type 1
PCSK2	Proprotein convertase subtilisin/kexin type 2
PD	Parkinson's disease
PDD	Parkinson's disease dementia
PDGF	Platelet-derived growth factor
PDGF-β	Platelet-derived growth factor b-chain
PET	Positron emission tomography
PFA	Paraformaldehyde
pH	Potential of hydrogen
PLA	Proximity ligation assay
PPIX	Protoporphyrin IX
ppm	Parts per million
PSD	Postsynaptic density

PSD 95	Postsynaptic density protein 95
PVDF	Polyvinylidene fluoride
REM	Rapid eye movement
RNA	Ribonucleic acid
RRID	Research resource identifier
S.E.M.	Standard error of the mean
SER	Smooth endoplasmic reticulum
SPARC	Secreted protein acidic and cysteine-rich
Tab.	Table
TBS	Tris-buffered saline
TGF- β 1	Transforming growth factor- β 1
Thy1	Thymocyte differentiation antigen 1
TMB	3,3',5,5'-Tetramethylbenzidine
TNF- α	Tumor necrosis factor- α
TREM2	Triggering receptor expressed on myeloid cells 2
TSPO	18 kDa Translocator protein
U	Unit
WT	Wild-type
YS	Yolk sac
μ g	Microgram
μ L	Microliter
μ m	Micrometer
μ M	Micromolar
μ m ³	Cubic micrometer

Acknowledgments

Embarking on my Ph.D. odyssey has been a profoundly enriching and rewarding adventure, encompassing numerous instances of exploration, adversity, and personal development. I am profoundly thankful for the backing I have been fortunate to receive from a multitude of individuals throughout this journey.

Initially, I wish to convey my sincerest gratitude to my mentor, Prof. Jochen Herms. Your counsel, guidance, and confidence in my capabilities have been pivotal in molding my research and overall academic path. Your enthusiasm for neuroscience and unwavering commitment to mentorship has motivated me to pursue excellence in my endeavors.

Furthermore, I extend my wholehearted appreciation to the veterinarians and animal caretakers who have played an indispensable role in my research. Your proficiency, attentiveness, and dedication to animal welfare have been crucial in safeguarding the well-being and health of the mouse models employed in my experiments. Your empathy and professionalism have significantly influenced the success of my research, and I am deeply grateful for your collaboration.

To my colleagues in the laboratory, I extend my gratitude for being a pillar of support and camaraderie amid the peaks and valleys of graduate studies. Your companionship, mutual experiences, and stimulating scientific conversations have enriched my time as a Ph.D. student and rendered it truly unforgettable.

I also wish to acknowledge my collaborators from the University of Sydney and Plexikon for supplying the essential animal models and chemical components for my project. My research would not have come to fruition without their assistance.

My heartfelt thanks go to my family and friends for their steadfast support, motivation, and comprehension throughout this odyssey. Your unwavering faith in me has fueled my determination, and I am grateful for your involvement in my life.

In summary, my Ph.D. expedition has presented an array of challenges and triumphs, and I am deeply indebted to everyone who has offered their encouragement and support along the way. Your collective input has been invaluable, and it is an honor to recognize your contributions in my dissertation.

List of Publications

Articles and manuscripts:

1. **Cui, M.**, Zu, J., Shi, Y., Herms, J. Spatial transcriptomics reveals a neuron-astrocyte-microglia vicious loop regulating synaptic plasticity in Alzheimer's disease. (In preparation)
2. **Cui, M.**, Zu, J., Shi, Y., Herms, J. Impact of astrocytic amyloid precursor protein on synaptic function. (In preparation)
3. **Cui, M.**, Zu, J., Brendel, M., Shi, Y., Herms, J. Long-term voluntary physical activity attenuates microglia-mediated synaptic impairment in transgenic mouse models of Alzheimer's disease. (In preparation)
4. **Cui, M.**, Shi, Y., Zu, J., Banati, R.B., Liu, G.J., Middleton, R.J., Herms, J. TSPO ligand XBD173 alters microglial synaptic engulfment via translocator protein (18 kDa). (In preparation)
5. Shi, Y., **Cui, M.**, Ochs, K., Brendel, M., Strübing, F.L., Briel, N., Eckenweber, F., Zou, C., Banati, R.B., Liu, G.J., Middleton, R.J., Rupprecht, R., Rudolph, U., Zeilhofer, H.U., Rammes, G., Dorostkar, M.M., Herms, J., 2022. Long-term diazepam treatment enhances microglial spine engulfment and impairs cognitive performance via the mitochondrial 18 kDa translocator protein (TSPO). *Nature Neuroscience*, 25(3), pp.317-329.
6. Shi, Y.*, **Cui, M.***, Zu, J., Ruf, V., Zou, C., Banati, R.B., Liu, G.J., Middleton, R.J., Rammes, G., Rupprecht, R., Herms, J. Astrocytic diazepam binding inhibitor confers microglial synaptic engulfment in synucleinopathy via translocator protein 18 kDa (TSPO). (*Contributed equally) (Submitted)

7. Li, S.* , Chen, X. * , **Cui, M.***, Tang, Y.* , Cui, N., Shi, Y., Herms, J, Zou, C. Glucose hypometabolism induces neuronal necroptosis in tauopathies. (*Contributed equally) (In preparation)

Book chapter:

1. Shi, Y., **Cui, M.**, Blume, T., Herms, J. Intravital imaging and analysis of the structural plasticity of dendritic spines in multiple brain regions. *Neurochemistry Methods*. Springer. (In press)

Conferences:

1. **Cui, M.**, Zu, J., Shi, Y., Herms, J. TSPO ligand XBD173 alters microglial synaptic engulfment via translocator protein (18 kDa). *2023 CINP world congress*. 2023 May; Montreal, Canada.
2. **Cui, M.**, Zu, J., Shi, Y., Herms, J. Translocator protein (18 kDa) deficiency attenuates excessive synaptic elimination by microglia in synucleinopathy. *Neuroscience 2022 (Society for Neuroscience)*. 2022 Nov.; San Diego, USA.
3. Herms, J., **Cui, M.**, Shi, Y. Benzodiazepine diazepam alters microglial synaptic engulfment via translocator protein (18 kDa). *Neuroscience 2022 (Society for Neuroscience)*. 2022 Nov.; San Diego, USA.
4. **Cui, M.**, Zu, J., Shi, Y., Herms, J. Translocator protein (18 kDa) deficiency attenuates excessive synaptic elimination by microglia in synucleinopathies. *20th Eibsee Meeting "Cellular Mechanisms of Neurodegeneration"*. 2022 Oct.; Munich, Germany.
5. Shi, Y., **Cui, M.**, Zu, J., Herms, J. Translocator protein (18 kDa) regulates microglial synaptic engulfment in synucleinopathy. *The International Conference on Molecular Neurodegeneration (ISMND 2022)*. 2022 Oct.; Athens, Greece.

6. **Cui, M.**, Shi, Y., Herms, J. Benzodiazepine diazepam induces dendritic spine loss via 18 kDa translocator protein. *FENS Forum 2022*. 2022 July; Paris, France.
7. **Cui, M.**, Zhu, K., Herms, J. Alterations of neuronal oscillation in early stages of Alzheimer's disease. *14th International Conference on Alzheimer's and Parkinson's Diseases (AD/PD 2019)*. 2019 Mar; Lisbon, Portugal.

Eidesstattliche Versicherung/Affidavit

Hiermit versichere ich an Eides statt, dass ich die vorliegende Dissertation Astrocytic Diazepam Binding Inhibitor Instructs Microglial Synaptic Engulfment in Lewy Body Dementia selbstständig angefertigt habe, mich außer der angegebenen keiner weiteren Hilfsmittel bedient und alle Erkenntnisse, die aus dem Schrifttum ganz oder annähernd übernommen sind, als solche kenntlich gemacht und nach ihrer Herkunft unter Bezeichnung der Fundstelle einzeln nachgewiesen habe.

I hereby confirm that the dissertation Astrocytic Diazepam Binding Inhibitor Instructs Microglial Synaptic Engulfment in Lewy Body Dementia is the result of my own work and that I have only used sources or materials listed and specified in the dissertation.

München, im 21 Nov. 2023

Mochen Cui

Confirmation of Congruency

I hereby declare that the electronic version of the submitted dissertation, entitled Astrocytic Diazepam Binding Inhibitor Instructs Microglial Synaptic Engulfment in Lewy Body Dementia is congruent with the printed version both in content and format.

München, im 21 Nov. 2023

Mochen Cui